Tunneling through Nanostructures - Interactions, Interference and Broadening

Pedersen, Jonas

2008

Citation for published version (APA):
Pedersen, J. (2008). *Tunneling through Nanostructures - Interactions, Interference and Broadening*. [Doctoral Thesis (compilation), Mathematical Physics]. Department of Physics, Lund University.

Total number of authors:
1

LUND UNIVERSITY

PO Box 117
221 00 Lund
+46 46-222 00 00

Tunneling through nanostructures - interactions, interference and broadening

Jonas Nyvold Pedersen

Division of Mathematical Physics
Faculty of Science

Lund University 2008

Printed in Sweden 2008 at Tryckeriet i E-huset, Lund.
ISBN-978-91-628-7643-2

Tunneling through nanostructures - interactions, interference and broadening

Jonas Nyvold Pedersen

Division of Mathematical Physics
Faculty of Science

Lund University, Sweden

Dissertation for the degree of
Doctor of Philosophy in Science

Thesis Advisor: Andreas Wacker

Faculty Opponent: Tobias Brandes, TU Berlin, Germany

Academic dissertation which, by due permission of the Faculty of Science at Lund University, will be publicly defended on Wednesday, December 17, 2008, at 10:15 in lecture hall B, Sölvegatan 14A, Lund, for the degree of Doctor of Philosophy in Science.

The thesis is based on the following publications:

I Andreas Fuhrer, Linus E. Fröberg, Jonas N. Pedersen, Magnus W. Larsson, Andreas Wacker, Mats-Erik Pistol and Lars Samuelson
Few electron double quantum dots
in InAs/InP nanowire heterostructures
Nano Letters **7**, 243 (2007).

II Jonas Nyvold Pedersen and Andreas Wacker
Tunneling through nanosystems:
Combining broadening with many-particle states
Phys. Rev. B **72**, 195330 (2005).

III Jonas Nyvold Pedersen, Benny Lassen,
Andreas Wacker and Matthias H. Hettler
Coherent Transport through an interacting double quantum dot:
Beyond sequential tunneling
Phys. Rev. B **75**, 235314 (2007).

IV Jonas Nyvold Pedersen, Dan Bohr, Andreas Wacker,
Tomas Novotný, Peter Schmitteckert, and Karsten Flensberg
Interplay between interference and Coulomb interaction
in the ferromagnetic Anderson model with applied magnetic field
Submitted to *Phys. Rev. B, arXiv:0810.5293v1.*

Also published during PhD studies but not contained in the thesis:

A Jonas N. Pedersen, Jesper Q. Thomassen and Karsten Flensberg
Noncollinear magnetoconductance of a quantum dot
Phys. Rev. B **72**, 045341 (2005).

B Tomas Novotný, Jonas Nyvold Pedersen, Tobias Ambjörnsson,
Mikael Sonne Hansen and Ralf Metzler
Bubble coalescence in breathing DNA:
Two vicious walkers in opposite potentials
EPL **77**, 48001 (2007).

Contents

Part A

Introduction, Background and Methods

1

Popular Science Summary

This thesis treats electron transport, or more precisely, the theoretical methods for calculating the electron transport through nanodevices. For macroscopic objects such as, e.g., a light bulb, Ohm's law relates the drop in electric potential, V, the resistance, R, and the current I, through the relation $V = RI$, see Fig. 1.1. Ohm's law also holds for large electronic components, but over the last fifty years it has constantly been possible to diminish the sizes of the electronic components and reach a regime where Ohm's law is no longer valid. In these devices, the smallest length scales can be down to 45 nanometers, i.e. $1/1.000.000.000$ m $= 10^{-9}$ meter $= 1$ nm.

An active field of basic research is to produce objects which are on the nanoscale and then connect them to wires for usage in electronic devices, so-called nano-electronics. This is a very difficult task and it may take several years before it can be exploited commercially. Examples of nano-objects are carbon nanotubes, single-molecules, and nanowires, where the latter is used as an example below. In these devices the current is not governed by the laws of classical electrodynamics, but rather the laws of quantum mechanics.

A nanowire is a thin rod of semiconducting materials with a length up to several microns ($1/1.000.000$ m $= 10^{-6}$ meter $= 1$ μm), but with a diameter of only $10-100$ nm. In comparison, the thickness of a human hair is about 50 μm. It is possible to form segments of different materials and, by a proper choice of materials, to grow two 'barriers' and thereby create a small 'box' confining the electrons, see Fig. 1.1. Such a box, down to a few nanometers long, is often referred to as a 'quantum dot'. It is also possible to create a series of coupled quantum dots, e.g. a double quantum dot by growing three separate barriers. The pieces of wire surrounding the quantum dots act as contacts, and by attaching wires to the these pieces an electric circuit can be formed and the current can be measured.

The laws of quantum mechanics give rise to two particular effects in the nanowire containing a quantum dot. First, the electrons in the quantum dot cannot have arbitrary energies but only some specific energies are possible, so-called energy levels. Secondly, there is a certain probability that the electrons

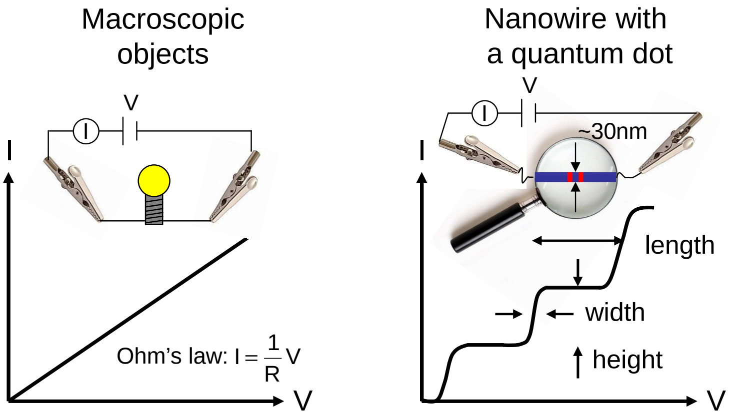

Figure 1.1: The current I versus the potential V for a macroscopic object and a nanowire with a quantum dot, respectively.

will cross the barriers and escape from the quantum dot, which is named the quantum tunneling effect. In addition, there is the classical effect that the electrons repel each other as they are charged particles, and therefore it costs extra energy to add an electron to the quantum dot.

Because of these effects, the current does not show a linear dependence on the potential but instead steps occur, see Fig. 1.1. It is even possible that the current suddenly decreases for increasing electric potential. The step-like behaviour can be exploited in electronic devices but can also be used to analyze the electronic properties of the quantum dot. The lengths of the steps reveal information about the energy levels in the quantum dot and the electric repulsion between them due to the Coulomb interaction, and the heights about the coupling to the surrounding segments and the Coulomb interaction. The widths of the steps depend on the temperature and how good the contacts are between the surrounding pieces of wire and the quantum dot.

In this thesis, current measurements on an electric circuit including a nanowire with two quantum dots are analyzed, setting the stage for a method for calculating the electron transport through simplified model systems representing the most important features of quantum dots or molecules. The method constitutes the main part of this thesis and allows for calculating IV-curves, taking into account the level energies, the Coulomb interaction, and the smearing of the steps.

2

Populärvetenskaplig sammanfattning

Denna avhandling behandlar elektrontransport, eller för att vara mer precis, de teoretiska metoder som används vid beräkning av elektrontransport genom nanostrukturer. För makroskopiska objekt, t.ex. en glödlampa, relaterar Ohms lag spänningsfallet V, resistansen R och strömmen I, genom sambandet $V = RI$, se Fig. 2.1. Ohms lag gäller även för stora elektroniska komponenter, men under de senaste femtio åren har utveckling gått mot mindre och mindre komponenter så att vi idag befinner oss i en regim där Ohms lag inte längre är tillämpbar. I dessa komponenter kan de minsta längdskalorna vara ner till 45 nanometer, d.v.s. 1/1.000.000.000 m = 10^{-9} meter = 1 nm.

Ett aktivt område inom grundforskningen är att producera objekt av nanoskala för sedan ansluta dem till elektroniska komponenter, s.k. nanoelektronik. Detta är en väldigt svår uppgift och det kan ta flera år innan den kan bli kommersiellt gångbar. Exempel på nanoobjekt är kolnanotuber, enskilda molekyler och nanotrådar, där de senare används som exempel nedan. I dessa komponenter lyder inte strömmen under de klassiska lagarna hos elektrodynamiken, utan snarare kvantmekanikens lagar.

En nanotråd är en tunn stav av halvledarmaterial med en längd upp mot flera mikrometer (1/1.000.000 m = 10^{-6} meter = 1 m), men med en diameter på endast 10-100 nm. Som en jämförelse är tjockleken på ett hårstrå runt 50 m. Det är möjligt att bygga segment av olika material och, genom lämpligt val av material, skapa två “barriärer” för att på så sätt bilda en liten låda där elektronerna innesluts, se Fig. 2.1. En sådan låda, som kan vara ner mot ett fåtal nanometer lång, kallas ofta för en “kvantprick”. Det är också möjligt att skapa en serie av kopplade kvantprickar, t.ex. en dubbel kvantprick genom att skapa tre separata barriärer. De delar av tråden som omger kvantpricken fungerar som kontakter, och genom att ansluta metalltrådar till dessa delar kan elektriska kretsar skapas för mätning av strömmen.

Kvantmekanikens lagar ger upphov till två speciella effekter för en nanotråd innehållande en kvantprick. För det första kan inte elektronerna i kvantpricken

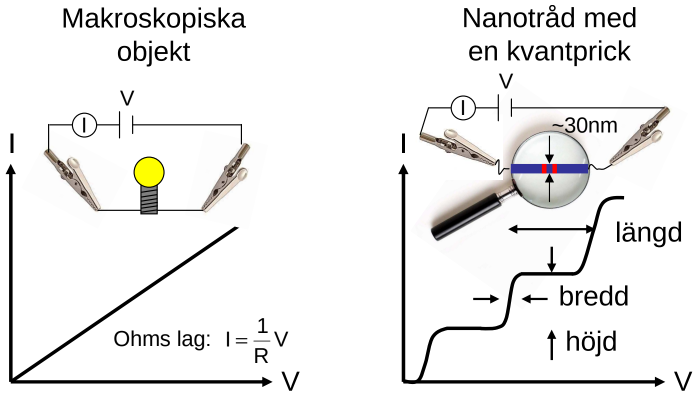

Figur 2.1: Strömmen I mot potentialen V för ett makroskopiskt objekt respektive en nanotråd med en kvantprick.

ha godtyckliga energier utan endast vissa energier är möjliga, s.k. energinivåer. För det andra är det en viss sannolikhet att elektroner kommer korsa barriärerna och fly från kvantpricken, något som kallas kvanttunnling. Dessutom finns en klassisk effekt att elektronerna repellerar varandra eftersom de är laddade partiklar, och det kostar därför extra energi att lägga till en elektron till kvantpricken.

P.g.a. dessa effekter visar inte strömmen ett linjärt beroende av spänningen utan istället förekommer steg, se Fig. 2.1. Det är även möjligt att strömmen plötsligt minskar för ökande spänning. Detta steglika uppförande kan utnyttjas i elektroniska komponenter men kan även användas för att analysera de elektroniska egenskaperna hos kvantpricken. Längden på stegen ger information om energinivåerna i kvantpricken och den elektriska repulsionen mellan elektronerna p.g.a. Coulomb växelverkan, medan höjden på stegen ger information om kopplingen till de omgivande segmenten och Coulomb växelverkan. Bredden på stegen beror på temperaturen och hur bra kopplingen är mellan de omgivande bitarna och kvantpricken.

I denna avhandling analyseras strömmätningarna av en elektrisk krets innehållande en nanotråd med två kvantprickar. För att studera detta experiment utvecklas en metod för beräkning av elektrontransport genom förenklade modellsystem vilka representerar de viktigaste egenskaperna hos kvantprickar och molekyler. Denna metod utgör huvuddelen av denna avhandling och möjliggör beräkning av IV-kurvor där hänsyn tagits till energinivåerna, Coulomb växelverkan och utsmetningen av stegen.

I gratefully acknowledge Olov Karlström for translating the Popular Science Summary.

3

Introduction to transport through nanostructures

For macroscopic electric devices like, e.g., a light bulb, the laws of classical physics can be applied. The relation between the potential, the resistance and the current is given by Ohm's law. When the sizes of the electric objects diminish this no longer holds true, and a different framework for describing the transport of electrons is needed.

Starting from macroscopic objects and diminishing the sizes, the scale of microelectronics is reached, i.e., where the sizes of the smallest components are on the micrometer scale. These components are typically made of silicon wafers using lithographical techniques, but in many situations the physical laws for macroscopic objects can still be applied.

A decrease of the size in one of the dimensions can be realized in layered semiconductor structures, where materials with different band gaps are deposited on top of each other using molecular beam-epitaxy. The thickness of each layer is well-controlled and can be down to a few atomic layers [1, 2, 3]. Due to the different band gaps, electrons are confined to certain layers, thereby creating two-dimensional electron gases. These structures have been used to make, e.g., resonant tunneling diodes, superlattices, and even more advanced structures such as quantum cascade lasers. The theoretical description of the electronic and optical properties requires a full quantum mechanical description, see, e.g., Ref. [4].

Confining the electrons in two dimensions leads to the formation of quantum wires, which are effectively one-dimensional objects. These can be realized, e.g., in cleaved-edge overgrown structures in GaAs [5], in InP nanowires created by laser-assisted catalytical growth [6], or by chemical-beam epitaxial growth of GaAs nanowires [7].

Finally, confining the electrons in all three spatial directions creates zero-dimensional objects, so-called quantum dots. They are also frequently referred to as "artificial atoms" or "man-made atoms". For sizes on the nanometer scale, these objects show a significant level quantization with clearly separated levels. As the smallest length scales typically range from a few nanometers up to hundreds of nanometers, these objects are often named nanostructures.

Various types of nanostructures exist. Frequently studied objects are quantum dots created in a two-dimensional electron gas, where the latter is formed at the interfaces between semiconducting materials with different band gaps as mentioned above. Using lithographically defined metallic topgates, areas in the electron gas beneath the gates are depleted and quantum dots are formed. By tuning the gates, the tunnel couplings to source and drain contacts can be controlled, and the chemical potentials of the dots can be shifted (see e.g. [8] and references therein). Also in two-dimensional electron gases, quantum dots can be "cut-out" using electron-beam lithography and etching. The shapes of the dots can be controlled, and using sidegates the dots can be emptied down to the last electron [9]. Quantum dots can also spontaneously form when a thin layer of a semiconducting material is deposited on top of another semiconducting material with a different lattice constant using molecular beam-epitaxy. These self-assembled dots occur due to the lattice mismatch. Carving out the surrounding material, stacks with a single or a few quantum dots can be created [10]. All the previous examples have in common that the quantum dots are formed in a large surrounding environment using top-down techniques such as lithography.

Alternatively, nanostructures are created by making electric contact to objects which are native nano-objects, i.e., a bottom-up approach. Examples of these nanostructures are carbon nanotubes [11], C_{60} bucky-ball molecules [12], OPV-molecules [13], or semiconducting nanowires with barriers forming quantum dots. At Lund University intense research takes place within the field of semiconducting nanowires [7, 14, 15].

Nanowires are rods of semiconducting materials with a diameter down to tens of nanometers for III-IV materials [7, 14], such as, e.g., InAs-InP, and even less for Si-nanowires [16]. For both types the lengths can be several microns. The III-IV wires from Lund University are, e.g., grown from gold aerosols deposited on a wafer. Using chemical-beam epitaxy, the wires grow catalytically only underneath the gold particles which stay at the top of the wires. By changing the gas in the growth chamber during growth, another type of material is deposited under the gold particle and a heterostructure is formed. Matching materials with different band gaps creates barriers in the structure, which form quantum dots as for example in an InAs wire with InP barriers. By changing the size of the catalyst particles, size control of the diameters of the wires can be achieved [7]. Figure 3.1 shows two InAs wires with triple InP barriers, and in Chap. 4 transport spectroscopy data of a nanowire double dot structure is analyzed.

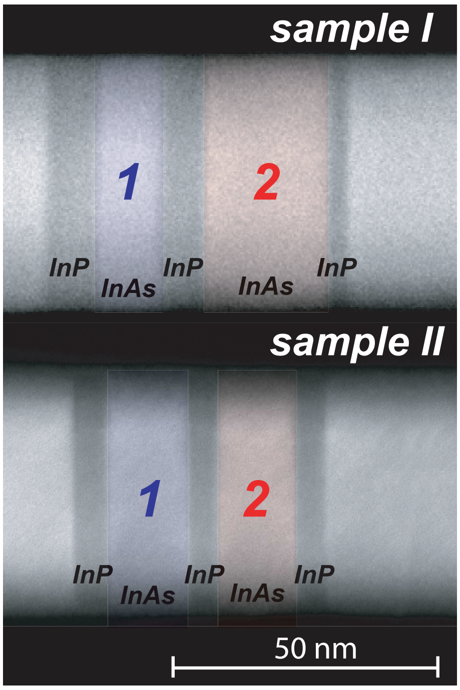

Figure 3.1: Two different InAs-nanowires with InP barriers. The transport characteristics of a device similar to sample I is further discussed in Chap. 4. From Paper I.

Nanostructures are interesting as they are potential candidates for new opto-electronic devices such as single-electron transistors or quantum dot lasers but are also exciting from a fundamental point of view, as they offer the possibility to study basic quantum mechanics. Due to the spatial confinement, the level spectrum displays discrete energies with spacings up to several meV, and the energy-cost for adding an electron can be several meV due to a pronounced Coulomb repulsion. These features of a single nanostructure can be investigated using, e.g., transport spectroscopy. Figure 3.2 shows so-called stability diagrams, i.e. plots of the differential conductance versus bias and gate voltage, for a single- and a double quantum dot structure defined in nanowires. In both cases, the wire is placed on an insulating substrate with a conducting layer beneath acting as a backgate. By changing the potential of the backgate, the energy levels in the quantum dots are shifted and clear Coulomb diamonds are observed. Within each diamond the occupation numbers in the dots are constant, and the sides of the diamonds mark the onset of sequential tunneling

Quantity	Energy scale
Temperature	1 K $\sim$ 0.1 meV
Level spacing	$\sim$ meV
Magnetic field	1 T $\sim$ 0.1 meV
Couplings ($\hbar\times$transition rate)	$\sim>$ 0.1 meV
Charging energies	$\sim$ meV

Table 3.1: Energy scales in transport through nanostructures.

as further discussed in Chap. 4.[1] Analyzing the shapes and the sizes of the diamonds reveals information about the level structure and the charging energies [17]. Figure. 3.3 shows the IV-characteristic for an InAs-InP heterostructure nanowire with a double quantum dot similar to sample I in Fig. 3.1. When the levels in the two dots pass each other due to the shifts in the electrostatic environments, peaks in the current appear giving rise to pronounced negative differential conductance. The inset shows how source and drain contacts are attached to the wire.

From a theorist's perspective, nanostructures offer new challenges. When the sizes decrease there is no longer a continuum of states available for the electrons but rather quantized levels which can be broadened due to coupling to leads. In addition, as the electrons are squeezed together Coulomb interactions can play an important role. The latter implies that the electrons cannot be described as individual particles, which complicates the theoretical description significantly. Furthermore, as electrons can pass through different levels interference may occur. Such effects should be included in a theoretical formalism, but as discussed in more detail in Chap. 5, the available methods for describing quantum transport have a limited range of validity, which depends on the energy scales in the problem. In Table 3.1 some characteristic energy scales occurring in transport through nanostructures are shown, and note that they can all be of the same order of magnitude. This motivates why a method which can handle several different effects and energy scales is needed.

In the rest of this thesis various aspects of quantum transport through nanostructures are considered. In Chap. 4 a detailed analysis of data obtained from measurements on an InAs-InP nanowire is presented. The analysis is based on a capacitance model, but as all parameters cannot be established from the data, an electrostatic model of the nanowire is set up. In Chap. 5 an overview of different methods for calculating transport through nanostructures

---

[1] Further examples of Coulomb diamonds for single dots are found in Fig. 4 in Paper II and in Chap. 8.

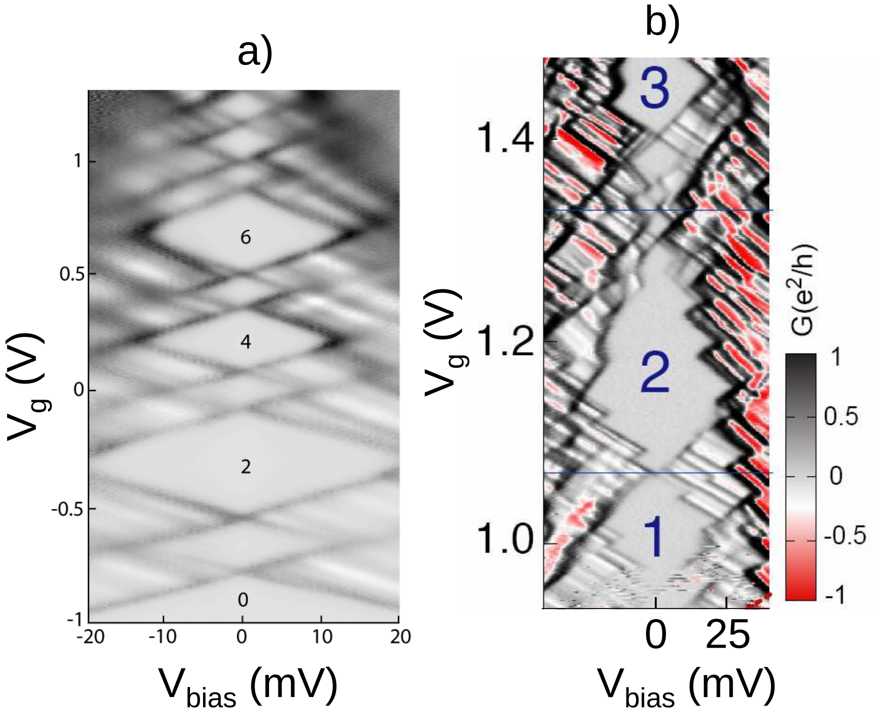

Figure 3.2: a) Measurement of the differential conductance, $G = dI/dV$, versus bias and gate voltage for a single quantum dot in an InAs wire with a double InP barrier. The diameter of the wire is approximately 50 nm and the dot is 18 nm long. Clear Coulomb diamonds are observed, where the numbers indicate the filling of the dot. *The data are kindly provided by L.E. Fröberg.* b) The measured differential conductance, $G = dI/dV$, versus bias and gate voltage for a double quantum dot in a device similar to sample I in Fig. 3.1. Coulomb diamonds are observed, and the numbers indicate the filling of dot 1. The additional structure along the edges is partly due to the filling of dot 2. From Paper I.

is presented, where the focus is on density-matrix based methods. A newly developed method is presented, which forms the core of this thesis. In the subsequent chapters the method is applied to various model systems and the results are compared with other theoretical approaches. In Chap. 6 transport through a double quantum dot is investigated, where the focus is on various quantum mechanical sources for negative differential conductance. The topic of Chap. 7 is the delicate interplay between interference and interactions in a model with a single level coupled to ferromagnetic leads and in addition having an applied

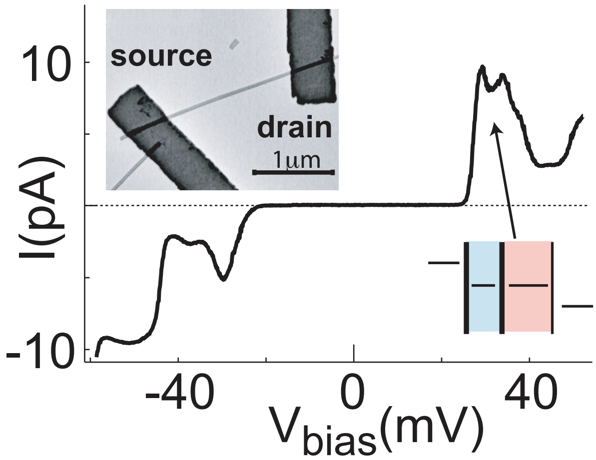

Figure 3.3: IV-characteristic for a double quantum dot displaying clear peaks when two levels are at resonance within the bias window (see the lower right inset). When the levels slide by each other due to electrostatic effects, negative differential conductance occurs. The upper left inset shows a SEM image of sample I with two Ni/Au source and drain contacts attached. The double dot structure is placed somewhere between the contacts. From Paper I.

magnetic field non-collinear with the magnetizations of the leads. Finally, in the regime where sequential tunneling processes are suppressed, current may still flow due to higher-order processes, so-called cotunneling processes. For finite bias, these processes may lead to the occupation of excited states. This is discussed in Chap. 8. In Chap. 9 a short summary and outlook is given.

4

Transport spectroscopy of an InAs-InP double quantum dot

In this chapter transport spectroscopy data of a particular nanostructure, an InAs nanowire with three InP barriers forming a double quantum dot, is investigated. The aim is to deduce the quantum mechanical single-particle level spacings and the Coulomb charging energies. These quantities are not directly accessible from the experiment, but can be found from an electrostatic model of the nanowire.

The basic idea is that due to Coulomb interactions, the energy levels in each dot are affected by the charging of the same as well as the neighbouring dot. Furthermore, changing the chemical potentials of the leads or the nearby backgate alters the electrostatic environments of the dots and, consequently, the position of the levels. Together with the quantum mechanical level spacings, these effects are captured in a model for the energy levels which can be cast on the form

$$E_1(N_1, N_2, V, V_g) = \Delta_1^{\mathrm{QM}}(N_1) + \frac{1}{2}E_{C1}(2N_1 - 1) + E_{Cm}N_2 - e\alpha_g^1 V_g + e\alpha_V^1 \frac{V}{2}, \tag{4.1}$$

and

$$E_2(N_1, N_2, V, V_g) = \Delta_2^{\mathrm{QM}}(N_2) + \frac{1}{2}E_{C2}(2N_2 - 1) + E_{Cm}N_1 - e\alpha_g^2 V_g - e\alpha_V^2 \frac{V}{2}. \tag{4.2}$$

Here $N_{1(2)}$ denote the occupation of dot 1(2), V_g is the potential of the backgate, $V_g = V_{\mathrm{BG}}$, and $e = |e|$ is the elementary charge. The bias voltage $V = V_{\mathrm{bias}}$ is applied symmetrically, $V_R = -V_L/2 = V/2$, and, finally, the chemical potential of the left lead is $\mu_L = -eV_L = eV/2$ and for the right lead $\mu_R = -eV/2$.

In Eqs. (4.1)-(4.2), the first term in each expression is the addition energy due to the quantum mechanical level spacing. The rest, denoted $\mu_{1,2}(N_1, N_2, V, V_g)$, is due to the mutual capacitive coupling between the dots, the leads and the backgate. The charging energies due to the electrostatic interactions within each dot are $E_{C1(2)}$, while E_{Cm} is the intradot charging energy. The quantities $\alpha_g^{1,2}$ show the response of the level position in each dot due to a change in the potential of the common backgate, while $\alpha_V^{1,2}$ indicates the response due to a change in the chemical potentials of the leads. The entities related to the shifts in bias or gate voltage are denoted lever arms.

Except for the quantum mechanical level spacings, the other seven quantities of interests, i.e. the three charging energies and the four lever arms, are related in terms of the seven capacitances shown in Fig. 4.1, namely C_{g1}, C_{g2}, C_{L1}, C_{L2}, C_{R1}, C_{R2}, and C_m, where the notation is changed relative to Paper I from S(ource) and D(rain) to L(eft) and R(ight), respectively.

In the experimental setup, a nanowire with dots embedded similar to sample I in Fig. 3.1 is placed on a substrate and contacts are attached as shown in Fig. 3.3. The substrate consists of a dielectric oxide layer with a doped Si-layer beneath acting as a backgate. The applied capacitance model is almost identical to the one presented in Ref. [17] by W.G. v.d Wiel *et al.*, but they consider a double quantum dot formed in a two-dimensional electron gas defined by metallic gates. In these systems each of the dots is contacted by a separate gate, not a common backgate as for the nanowire double quantum dot. Furthermore, they assume that the dots are only capacitatively coupled to the nearest lead, but in the model presented here also the next-to-nearest lead-dot capacitances are included as further discussed below. Details of the capacitance model are found in App. A, and in App. B it is shown how the features in the data can be related to the capacitances.

In this chapter it is demonstrated how to extract the capacitances from measurements of the differential conductance versus bias and gate voltage. First a general overview of the interpretation of the different lines appearing in the data is given in Sec. 4.1. However, due to the common backgate the data can only provide five relations between the seven capacitances, and, consequently, two further conditions have to be found. This is done in Sec. 4.2, where the capacitances are calculated directly from the wire geometry using a finite-element solver. In Sec. 4.3 the experimental data and the results of the finite-elements calculations are combined, and values for the charging energies and the lever arms are estimated. Finally, a conclusion and a discussion is found in Sec. 4.4.

4.1 Analyzing the experimental data

The experimental data for the differential conductance versus bias and gate voltage is shown in Fig. 4.2a. If considering a *fixed vanishing bias voltage*, $V_{\text{bias}} = V = 0$ the following is observed: By increasing the gate voltage, no

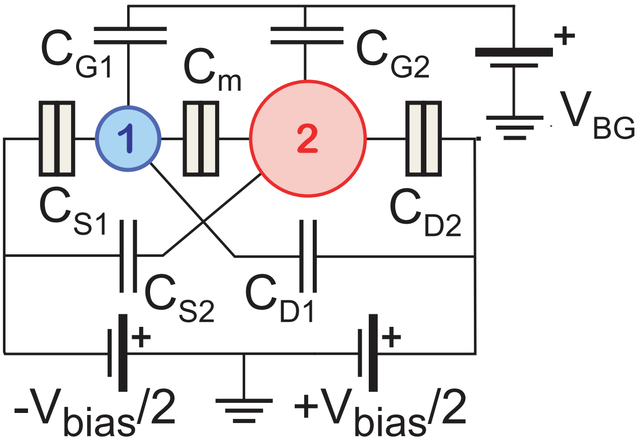

Figure 4.1: The capacitance model for a double quantum dot system with a common back gate. From Paper I.

structure is present below the gate voltage $V_{bg} = V_g = 0.9$ V.[1] At this value a change in the differential conductance, $G = dI/dV$ occurs, which is assigned to the addition of the first electron in dot 1. Subsequent filling of this dot occurs for increasing gate voltage. Below only $V_g < 0.9$ V and positive bias voltages are considered.

Before giving an interpretation of the measured data, it is discussed what can *a priori* be expected when performing a measurement of the differential conductance versus bias and gate voltage at low temperatures.

Previous experiments on similar single dots in InAs-InP nanowires have shown that only the lowest longitudinal quantum state is occupied for an electron number up to more than 15 if the length of the dot is smaller than ~ 20 nm [18]. As the lengths of the two dots in the double dot structure are 11.5 nm and 22.5 nm, respectively, it is assumed that for low electron numbers only the lowest longitudinal quantum state is occupied. So the single-particle level quantization seen in the data will presumably stem from the radial confinement.

As the considered DQD structure is asymmetric with dot 1 being roughly half the size of dot 2, see Fig. 3.1 sample I, the capacitive coupling between dot 1 and the gate is expected to be smaller than the one of dot 2 and the gate [15], $C_{g1} < C_{g2}$, i.e. a more positive gate voltage is needed in order to add the first electron to dot 1 than to add the first electron to dot 2.

Below the electron transfer through the structure is described as tunneling processes between eigenstates localized in each dot.[2] At positive bias voltage,

---

[1] Note that the gate voltage is given in Volts, while the bias voltage is in mV.

[2] In this picture the coherences between the states are neglected. The role of coherence is

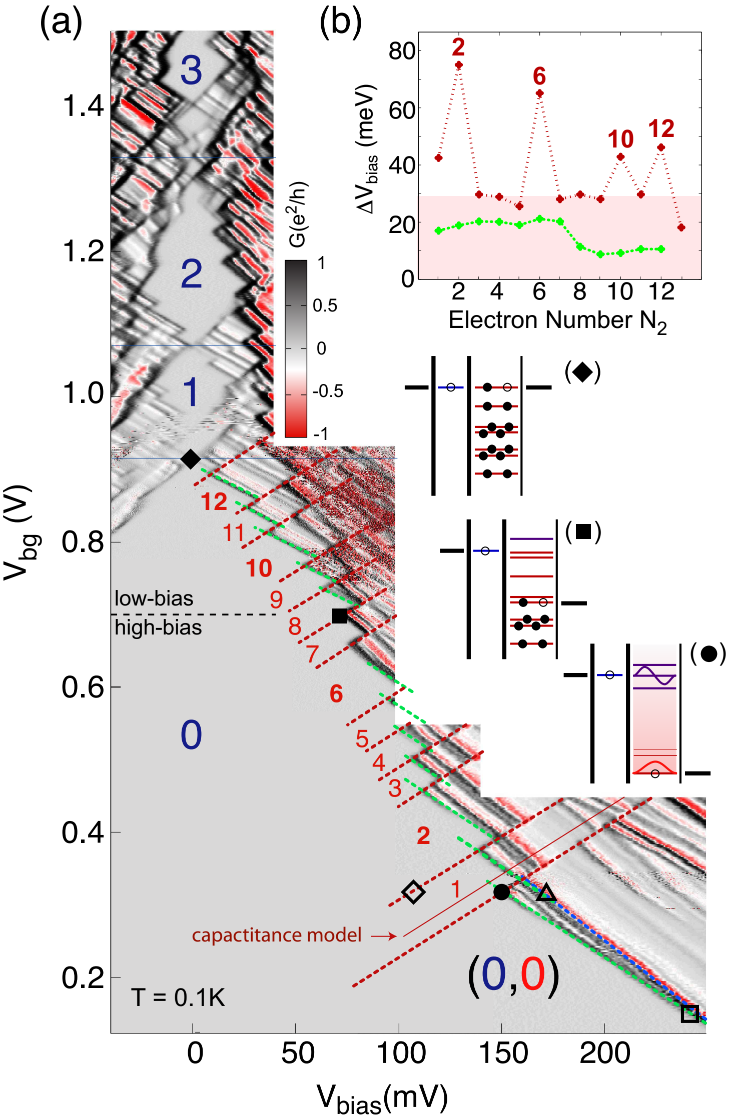

Figure 4.2: a) Measurements of the differential conductance, dI/dV, versus the source and bias voltage. The filling of dot 1(2) is indicated by the blue(red) numbers. b) The distances in bias voltage between the red and the green lines for a filling of dot 2, N_2, from 1 to 12. The sketches below b) show the level positions and the fillings of the dots for the points in the data specified in a). From Paper I.

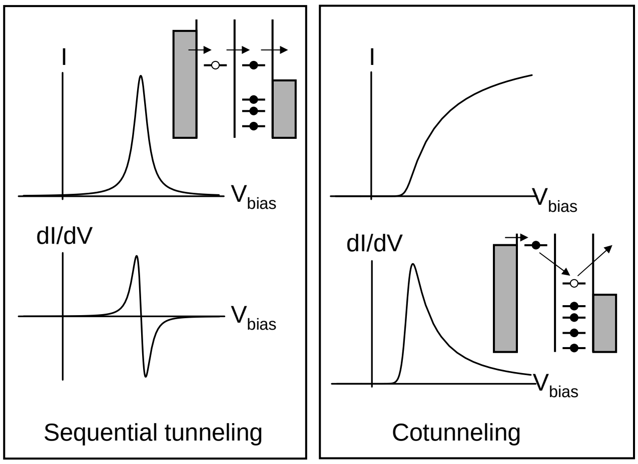

Figure 4.3: The pictures show how sequential tunneling and cotunneling give rise to two different types of lines in the measured data, see Fig. 4.2. For sequential tunneling, the levels in the two dots slide by each other due to the different capacitative couplings to leads, resulting in a peak in the current, I, and a wave-form in the differential conductance, dI/dV. At the onset of cotunneling, the current increases monotonously and a peak-structure appears in the differential conductance.

electrons tunnel into dot 1 from the left lead, subsequently tunnel into dot 2, and finally out into the right contact. However, these processes can occur in different ways, see also Fig. 4.3:

If a level in the left dot aligns with a level in the right dot within the bias window, a sequential tunneling process is possible. When the bias voltage and/or the gate voltage is varied, the levels will slide by each other due to the different lever arms and a resonance feature occurs, giving a sharp peak in the IV-curve and a wave form in the differential conductance dI/dV. In the experimental dI/dV-data in Fig. 4.2a, these processes give rise to a bundle of white-black-white-red-white lines with negative slopes, see e.g. the dashed blue line drawn between $\triangle - \square$. These lines will be denoted resonance lines and the slopes $\alpha_{\mathrm{resonance}}$.

Another feature occurs when tunneling is possible by overcoming a single energy mismatch, i.e. via a single cotunneling process through a virtual state; either between the states in the leads and the dot, or between the states in the different dots (see Fig. 4.4). The onset of these processes happens when the left(right) chemical potential aligns with the chemical potential of dot 1(2), and

---

discussed in Chap. 6.

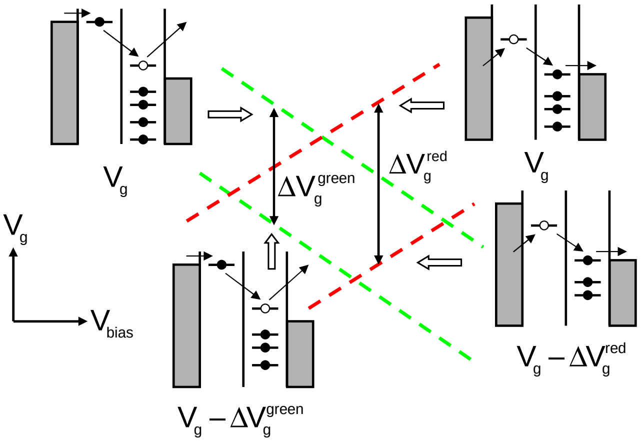

Figure 4.4: Schematic pictures of the appearance of the cotunneling lines, where electron transport is possible by overcoming only a single energy mismatch, i.e. via a cotunneling process through a virtual state.

gives rise to step in the IV-curve and a corresponding peak in the differential conductance, see Fig. 4.3. In the experimental data, a set of grey-black-grey lines occur as, e.g., seen between $\Box - \bullet$ in Fig. 4.2a. These lines will be denoted cotunneling lines as a virtual transition is involved.

In the data the dashed green lines, which have been drawn on top of the experimental data, are interpreted as cotunneling lines with an onset due to the alignment of the left chemical potential with the chemical potential of dot 1, $\mu_L = \mu_1$, see Fig. 4.2a and Fig. 4.4. The slopes of these lines are denoted α_{green}.

Similarly, the interpretation of the dashed red lines drawn on the data is that along these lines, the chemical potential of the right dot is aligned with the right chemical potential, $\mu_R = \mu_2$. These lines are also due to the onset of cotunneling processes, and the slopes are denoted α_{red}. At the crossing between the red and the green dashed lines, the chemical potentials of the left/right leads are aligned with the chemical potentials of the left/right contacts.

Together the red and the green dashed lines form a border, where the kinks of the border correspond to the filling of dot 2 by an extra electron. Below $V_g = 0.32$ V and $V = 150$ meV in Fig. 4.2a, the onset of the last dashed green line occurs, and it is assumed that below this gate voltage the double quantum dot structure is emptied.[3] Above this gate voltage several kinks in the data

---

[3] Even for a further increase of the bias voltage, no more kinks are observed.

are observed, indicating a filling of dot 2 up to at least 12 electrons (indicated by the red numbers on the figure).

When plotting the distance between the cotunneling lines versus the numbers of electrons in dot 2, N_2, shown in Fig. 4.2b, two features are observed:[4]

The distances between the green cotunneling lines are almost constant for the filling $N_2 < 7$, then it drops to a lower value and stays roughly constant for $N_2 \geq 8$. The change occurs at the point marked with '■' in Fig. 4.2a, and below a distinction between the *high/low-bias regime* with $N_2 < 7$ and $N_2 \geq 8$, respectively, is made. The change is explained as for a filling of $N_2 = 8$ electrons start to tunnel through an excited state in dot 2, see the lowest sketch in Fig 4.2c. As the shapes of the excited states are different than the shapes of the lower lying states, this might lead to the observed change in charging energy.

More striking is the large variation in the distances between the red lines, where large oscillations are imposed on an almost constant background value, independent of the filling of dot 2, as shown in Fig. 4.2b. The constant background is assigned to electrostatic effects as described by the capacitance model in App. A, while the large oscillations are due to the quantum mechanical level spacings, $\Delta_2^{QM}(N_2)$, induced by the radial confinement. The sequence shows magic numbers 2,6, 10 and 12, which is in accordance with both a hard-wall circular and a hexagonal confinement.[5] Similar shell structure is seen in etched vertical quantum dot structures [9] and also in single dot nanowire heterostructures [15].

Also the slopes of the cotunneling and resonance lines are different in the low- and high-bias regimes, but being (almost) constant within each regime. The results are shown in Table 4.1. Together with Eqs. (B.1)-(B.5) it gives five different relations between the capacitances. How to find an approximate expression for the last relations, C_{L2}/C_{L1} and C_{R1}/C_{R2}, is discussed in the next section.

---

[4] In Fig. 4.2 the distance between the lines is shown in bias voltage and not gate voltage as discussed here. As the lines are parallel, the two ways of measuring the distances are of course equivalent.

[5] Here 'magic numbers' $2, 6, 10, 12, \ldots$ means that the quantum mechanical single-particle levels are grouped into bunches/shells of two almost generate levels, then a larger spacing, then four almost degenerate levels, then a larger spacing, then four almost degenerate levels, and so forth. The notation of shell structure is frequently used in nuclear structure theory, see e.g. Ref. [19].

Quantity	High-bias regime	Low-bias regime
$\Delta V_g^{\mathrm{red}}$	50.3 meV	50.3 meV
$\Delta V_g^{\mathrm{green}}$	32.4 meV	22 meV
α_{red}	1.8	1.8
α_{green}	-1.9	-1.4
$\alpha_{\mathrm{resonance}}$	-2.3	-1.45

Table 4.1: Experimental values for the slopes of the blue resonance lines, the dashed red and green border lines, and the distances between the border lines for both the high- and low-bias regime.

4.2 Calculating capacitances using a finite-element solver

In order to deduce a reasonable estimate for the ratio, C_{L2}/C_{L1} and C_{R1}/C_{R2}, an electrostatic model is made and the capacitances are calculated.

In Paper I the geometry of the wire was determined from an high-angle annular dark-field scanning transmission electron microscope picture, see Fig. 1a in Paper I. In the experimental setup, the heterostructure nanowire is placed on a sandwich structure consisting of doped Si-layer acting as the backgate, with a 100 nm thick oxide-layer on top acting as a gate dielectric. In a complete model the backgate should be included in order to extract the capacitive couplings between the gate and the dots. However, this involves a full three-dimensional calculation, which is avoided for computational reasons. Instead the system is modelled as a free standing wire, which allows us to exploit the radial symmetry of the problem, reducing the task to a two-dimensional problem.[6]

To set up the electrostatic model the following assumptions are made: The nanowire is modelled as a perfect cylinder with a diameter of 40 nm, and the source(left) and the drain(right) leads are assumed to be perfect conductors and much longer than double dot structure (200 nm each). For the range of voltages considered, only a few electrons are present in each quantum dot ($N_{1,2} < 15$). It is therefore assumed that the excess charge does not completely fill the interior of the dots, and based on a $\mathbf{k} \cdot \mathbf{p}$-calculation the electrons are assumed to be confined in ellipsoids centered in the middle of the respective dots [20]. For dot 1 the size (length×width) is set to 6 nm×18 nm, and for dot 2 it is 10 nm×14 nm. Details are given in Fig. 4.5a. The scales agree approximately with sample I in Fig. 3.1. Here one has to take into account that a 5% size variation occurs due to the different wire diameters, and the device shown in Fig. 3.1 is not the actual device on which the measurements

---

[6] A few calculations where done for the full 3D problem, which showed that the capacitances C_{L1}, C_{L2}, C_{R1}, C_{R2} and C_m did not change significantly as compared to the 2D model.

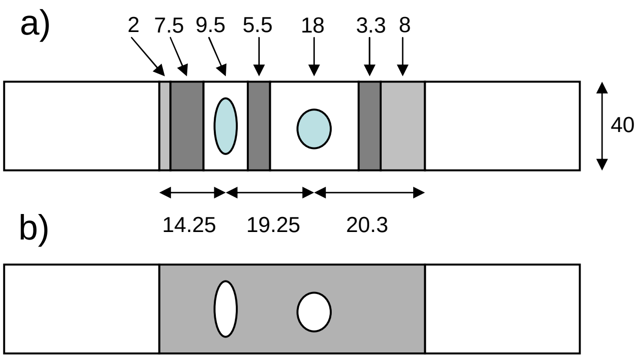

Figure 4.5: a) A sketch of the geometry of the nanowire (all lengths are in nm). The dark gray areas show the InP barrier material, while the white and light gray areas are InAs, with the latter being the depletion layers added at each end of the double quantum dot structure (see the main text). The ellipsoids are the assumed charge distributions in each dot, with the sizes being (length×width) 6 nm×18 nm for dot 1 and 10 nm×14 nm for dot 2. b) In the finite-element solver this geometry was used for calculating the capacitances, where the white areas are the perfect conductors, and in the gray area the relative dielectric constant is $\epsilon_r = 13$.

were performed. Due to the finite bias, an extra 8 nm depletion layer is added to the barrier at the drain contact and a 2 nm depletion layer at the source contact, see Fig. 4.5a.

Both ellipsoids are modelled as perfect conductors. As the relative dielectric constants of the InAs dot material ($\epsilon_r^{\mathrm{InAs}} = 14.55$) is rather close to the dielectric constant of the InP barrier material ($\epsilon_r^{\mathrm{InP}} = 12.37$), the same dielectric constant, $\epsilon_r = 13$, is used throughout the double quantum dot structure including the depletion layers, see Fig. 4.5b. Also the potential at infinity have to be specified, and therefore the whole nanowire is embedded in a cylindrical box much larger than the size of the nanowire (denoted the 'vacuum box').

In total there are five different conductors: The two leads, the two dots and the vacuum box.

The charge Q_i and the potential V_i of the i-th conductor are related to the other charges and potentials as $Q_i = \sum_{j=0} C_{ij}(V_i - V_j)$. The element C_{ij} in the capacitance matrix can be calculated by grounding all conductors except the jth conductor, which is set to unit potential ($V_j = 1$), and then calculate the total charge on the conductor i. As all charge on a perfect conductor is placed at the exterior, this equals the total surface charge ρ_s.[7]

The charges on the conductors are obtained by solving the Laplace equation

$$-\nabla\epsilon_0\epsilon_r(\mathbf{r})\nabla\phi(\mathbf{r}) = \rho(\mathbf{r}), \tag{4.3}$$

with $\phi(r)$ being the electrostatic potential, which relates to the electric field $\mathbf{E}(\mathbf{r})$ as

$$-\nabla\phi(r) = \mathbf{E}(\mathbf{r}). \tag{4.4}$$

As the electric field inside a perfect conductor vanishes, the potential inside the conductor is constant, i.e. it equals the potential at the boundary. In the calculation all boundaries involving conductors are set to a fixed potential, which is either ground or unit potential. The only other boundary conditions needed to be specified are at the outer surfaces between the barriers and the vacuum, and these are

$$\mathbf{n}\cdot(\mathbf{D}_{\mathrm{vac}} - \mathbf{D}_{\mathrm{barr}}) = 0, \tag{4.5}$$

where $\mathbf{D}(\mathbf{r})$ is the electric displacement field related to the electric field as $\mathbf{D}(\mathbf{r}) = \epsilon_0\epsilon_r(\mathbf{r})\mathbf{E}(\mathbf{r})$, and $\mathbf{D}_{\mathrm{vac/barr}}$ being the displacement field in the outside vacuum and in the barrier, respectively. $\mathbf{n}$ is a unit vector normal to the surface.

After solving the Laplace equation, the charge on each conductor can be calculated through the boundary condition

$$\mathbf{n}\cdot(\mathbf{D}_{\mathrm{vac/barr}} - \mathbf{D}_{\mathrm{cond}}) = \rho_s, \tag{4.6}$$

As the field inside the conductor, $\mathbf{D}_{\mathrm{cond}}$, is zero, it holds that

$$\mathbf{n}\cdot\mathbf{D}_{\mathrm{vac/barr}} = \rho_s. \tag{4.7}$$

So integrating the normal component of the displacement field over the surface of the conductor gives the total charge on the conductor.

The model is solved using the finite-element solver software *COMSOL Multiphysics* ©, and the results for the capacitances are presented in Table 4.2. For the relation between the lead and the dot capacitances the results are $C_{L2}/C_{L1} \approx 0.15$ and $C_{R1}/C_{R2} \approx 0.20$, showing that the next-to-nearest dot is not completely screened by the nearest dot. This will be taken as input when calculating the capacitances from the experimental data.[8]

---

[7] A check of the numerical solution is that $C_{ij} = C_{ji}$ and that the sum of the elements in each row of the capacitance matrix fulfills $\sum_j C_{ij} = 0$. The latter can be obtained by raising the potentials on all conductors by the same amount, which will not change the charges on the conductors.

[8] If one instead models the charge of the dots as completely filling the dots, the value of the lead-nearest-dot capacitance is very close to the value for a simple plate capacitor model, $C = A/[\epsilon_0\epsilon_r d]$ (d being the thickness of the barrier, and A the cross section of the wire), and the next-to-nearest dot is almost completely screened.

Capacitance	Value [aF]
C_{L1}	7.2
C_{L2}	1.1
C_{R1}	1.0
C_{R2}	4.9
C_m	3.5

Table 4.2: The calculated capacitances for the structure shown in Fig. 4.5 b.

4.3 Combining the experimental data and the capacitance model

As explained above, the data cannot provide all the information required to calculate the charging energies and lever arms. Based on the preceding section, the result of solving the Eqs. (B.1)-(B.5) using the ratios C_{L2}/C_{L1} and C_{R1}/C_{R2} in the range 0.1-0.3 is shown in Table 4.3 for the high-bias regime.[9] The results for the low-bias regime are not shown here, but can be found in Paper I.

Considering the variation of the capacitances, charging energies and lever arms with respect to C_{L2}/C_{L1} and C_{R1}/C_{R2}, the following trends are observed: In the high-bias regime, i.e. with $N_2 \leq 7$, the charging energies of dot 1 and dot 2 are almost identical and close to 13 meV and do not change much with the variation of the next-to-nearest lead coupling. This value is 2-3 times larger than the charging energy reported for similar single dots in InAs-InP nanowires [15], where they also find only a small variation of the charging energies versus the lengths of the dots, similar to our findings. The inter-dot charging energy is $\sim$ 0.4 times smaller than the intradot charging energies. If the next-to-nearest lead couplings are ignored, setting $C_{L2} = C_{R1} = 0$, the values for the charging energies are very different, showing an almost vanishing charging energy of dot 1 in contrast with the findings in Ref. [15] for single-dots. It is therefore concluded that for double dots in heterostructure nanowires, the next-to-nearest lead-dot capacitances are important.

The gate couplings satisfy $C_{g2} \gg C_{g1}$. A few calculations were done for the full three-dimensional structure including the backgate for a similar wire geometry, which indicated that for both dots the gate coupling should be $\sim$

---

[9] In Paper I the values stated for the two regime are taken for $C_{L2}/C_{L1} = C_{R1}/C_{R2} = 0.2$ and the margins stems from the maximum and minimum values in $C_{L2}/C_{L1} = C_{R1}/C_{R2} = 0.1 - 0.3$.

C_{L2}/C_{L1}	0.1	0.3	0.1	0.3	0.2	0.01	0.15
C_{R1}/C_{R2}	0.1	0.1	0.3	0.3	0.2	0.01	0.2
C_{g1} [aF]	0.558	0.488	1.116	1.027	0.817	0.085	0.839
C_{g2} -	3.06	3.036	2.703	2.689	2.861	3.19	2.866
C_{L1} -	12.78	6.829	7.790	5.289	6.940	351.5	7.811
C_{L2} -	1.28	2.049	0.779	1.587	1.388	3.51	1.718
C_{R1} -	0.518	0.497	1.296	1.252	0.917	0.057	0.9259
C_{R2} -	5.174	4.974	4.320	4.1732	4.585	5.73	4.629
C_m -	3.999	3.450	7.743	7.067	5.702	0.627	5.870
E_{C1} [meV]	9.6	15.4	11.4	14.0	13.2	0.685	12.25
E_{C2} -	12.7	12.9	13.1	13.2	13.1	12.3	13.02
E_{Cm} -	2.84	3.94	5.66	6.4	5.2	0.22	4.95
α_{g1}	0.088	0.122	0.175	0.197	0.160	0.007	0.153
α_{g2}	0.252	0.256	0.261	0.263	0.259	0.245	0.259
α_{V1}	0.666	0.538	0.336	0.250	0.393	0.974	0.420
α_{V2}	0.091	0.079	0.061	0.053	0.066	0.119	0.068

Table 4.3: High-bias regime: the capacitances, charging energies and lever arms for the ratios C_{L2}/C_{L1} and C_{R1}/C_{R2} between 0.1-0.3. Also the values for $C_{L2}/C_{L1} = C_{R1}/C_{R2} = 0.01$ (almost vanishing lead-next-to-nearest-dot capacitance) and $C_{L2}/C_{L1} = 0.15$ and $C_{R1}/C_{R2} = 0.20$ are shown.

0.5 aF, inline with the value of C_{g1}.[10] At the moment no clear explanation of the unexpected large value of C_{g2} exists.

4.4 Discussion and conclusion

An electrostatic model extending the work of Ref. [17] by including the next-to-nearest-lead-dot capacitances was presented, but it only contained a common backgate for both dots. As the *dI/dV*-data provided an insufficient number of parameters to determine all capacitances, the capacitances were calculated using a finite-element solver. The ratios for the lead-next-to-nearest-dot/lead-dot capacitances were taken as an input when estimating the charging energies and lever arms. Clear shell structure was seen, compatible with a hexagonal or a circular cross-section of the wire.

There are, however, some limitations of the applied method. From the experimental data, it is difficult to determine the position of the various lines

---

[10] For single dots in InAs-InP nanowires they report in [15] that the gate capacitance varies linearly with dot length between 1aF to 10aF for dots between 10 nm to 100 nm.

unambiguously, as the lines are rather broad. Especially, the resonance lines are problematic. Moreover, for the model calculation the laws of macroscopic electrodynamics were applied to objects which, concerning the barriers, are only several atom layers thick, and impurities and doping have not been taken into account. Consequently, the values found for the charging energies should be taken as order of magnitude estimates, rather than exact quantities. Nevertheless, the values found for the intra-dot charging energies, $E_{C1,C2}$, are comparable to values obtained for similar single dots in heterostructure nanowires [15].

In summary, it is concluded that next-to-nearest lead-dot capacitances are important for a quantitative description of multiple dot structures embedded in nanowires. However, these cannot be determined from transport experiments with no gate control of the individual dots but only having a common backgate.

A way of overcoming the problem of estimating the lead-next-to-nearest-dot capacitances would be to obtain individual gate control over the dots, which might be possible by placing the nanowire on a grid of gates. This was realized for a homogeneous wire, thereby creating electrostatically defined dots in the wire [21]. However, placing the heterostructure wire on the grid and obtaining the individual gate control seems to be an experimental challenge, as the exact location of the double quantum dot structure is difficult to determine.

5

Density matrix quantum transport

The main content of this chapter is a theoretical method for calculating transport through nanostructures presented in Sec. 5.3, which was published in Paper II and subsequently applied in Paper III-IV. In this chapter the method is put into context by discussing other approaches to quantum transport.

Below quantum transport through an open system, consisting of two (or more) leads connected to a central region is considered. The central region can be, e.g., a single or more quantum dots, a molecule, a carbon nanotube or a nanowire. In the rest of this thesis, the central region will be denoted the "quantum dot".

The system is described by a generic tunneling Hamiltonian, consisting of three parts,

$$H = H_D + H_{\text{leads}} + H_T, \tag{5.1}$$

describing the dot, the leads and the tunneling between the leads and the dot, respectively. The Hamiltonians will be further specified in Sec. 5.3.
Often the leads are modelled as non-interacting, while complicated many-body interactions might be present on the dot. The size of the dot is assumed to be so small that discrete quantum mechanical levels dominate the spectrum.

As an example of a generic model for this kind of setup, consider the Anderson model consisting of a single spinful level with an on-site Coulomb repulsion, U, and coupled to two reservoirs. Much theoretical work, numerical as well as analytical, has been devoted to this model and variations hereof, e.g., with the inclusion of more levels, vibrations, etc. When choosing the method for solving the transport problem, the energy scales to consider are the temperature of the leads times the Boltzmann factor, k_BT, the coupling strength[1], Γ, and finally

---

[1] The coupling strength depends on the specific system, but for a single level without spin the energy-dependent coupling strength is defined as $\Gamma(E) = 2\pi \sum_k |t_k|^2 \delta(E - E_k)$, with t_k being the tunneling amplitude between the dot state and a state k in one of the leads with energy E_k. Examples are given in Chap. 6-8.

the on-site Coulomb interactions, U.

In the regime of strong tunneling coupling, where the temperature is much smaller than the tunneling coupling, $k_BT/\Gamma \ll 1$, and the Coulomb repulsion is comparable to the coupling strength, $U \sim \Gamma$, the Anderson model displays the much studied Kondo effect, see, e.g., [22]. Among other features, the Kondo effect gives in the linear response regime at zero temperature perfect transmission through the dot, i.e. the conductance is $G = 2e^2/h$, even when the level is away from resonance. This is due to the formation of a correlated many-body state between the lead and the dot electrons. The investigation of the temperature dependence, magnetic field dependence, etc., requires non-perturbative methods, such as scaling or various renormalization group schemes [23, 24, 25, 26, 27]. However, several of these methods are restricted to zero temperature and/or the linear response regime, and often they are numerically expensive.

In the opposite regime, $k_BT/\Gamma \gg 1$, but still with a large Coulomb repulsion $U \gtrsim \max\{\Gamma, k_BT\}$, a much applied tool is the (generalized) master equation approach, also denoted the density matrix approach [28, 29, 30, 31, 32, 33], which will be discussed in Sec. 5.2. The method is applicable at finite bias, but often the effects of the leads are only included to lowest order in the tunneling coupling. Thereby all broadening of the levels is due to temperature, neglecting the level broadening due to the couplings to reservoirs. Higher-order effects such as interference or pair-tunneling are also not included.

Finally, when the Coulomb repulsion is not too large compared to the coupling strength, a transmission formalism is frequently applied, e.g., the nonequilibrium Green function formalism [34, 35]. This allows for including the broadening of the levels due to the coupling to leads and the description of higher-order effects, but the inclusion of interactions beyond the mean-field level is complicated [35].

In Paper II a method aiming at bridging the gap between the master equations and the transmission formalism is introduced. The method is based on the density matrix formalism, and by working in a basis of many-particle states of the dot Hamiltonian, correlations on the dot are taken fully into account. The method goes beyond the lowest-order expansion in the lead-dot coupling (the sequential tunneling approximation) by including coherent processes up to second order in the tunneling amplitude.

In the rest of this chapter, the use of the density matrix approach is briefly motivated in Sec. 5.1, and in Sec. 5.2 three approaches for deriving the generalized master equations are outlined. In Sec. 5.3 the formalism introduced in Paper II is presented, and in Sec. 5.4 the applied approximation scheme is more thoroughly discussed. Finally, a comparison with other methods is found in Sec. 5.5, and Sec. 5.6 contains the conclusions.

5.1 The density matrix approach

The density matrix approach is often used when considering transport through nanostructures. The central object is the density operator

$$\rho(t) = \sum_i W_i |i(t)\rangle\langle i(t)| \tag{5.2}$$

with $\{|\, i(t)\rangle\}$ being a complete basis set for the total system Hamiltonian, H, and $W_i \in [0,1]$ being the (classical) probability to find the system in state $|\, i\rangle$ at some initial time t_0. Due to the time evolution of the states, the time evolution of the density operator is governed by the von Neumann equation[2]

$$i\hbar \frac{\mathrm{d}}{\mathrm{d}t}\rho = -[\rho, H]. \tag{5.3}$$

The motivation for studying the density operator is that the expectation value of any operator, A, is given as

$$\langle A\rangle = \mathrm{Tr}\,[\rho A]\,, \tag{5.4}$$

where the trace is over a complete basis set. If the system can be divided into (at least) two subsystems, as in our case the leads and the dot, it is often assumed that at some initial time the densities can be factorized into a lead and a dot part, $\rho(t_0) = \rho^0_{\mathrm{leads}} \otimes \rho^0_{\mathrm{dot}}$. The tunneling Hamiltonian, H_T, couples the two subsystems, and mixing will occur. In the density matrix approach, the goal is to apply an approximation scheme, which allows for calculating an expression for the reduced dot density operator

$$\rho_{\mathrm{dot}}(t) = \mathrm{Tr}_{\mathrm{leads}}\,[\rho(t)]\,, \tag{5.5}$$

where the trace is over a complete set of lead states. This is achieved by finding a kinetic equation for the reduced dot density operator (or equivalently, the elements of the reduced dot density matrix), where the effects of the coupling to the reservoirs have been incorporated.

5.2 Generalized Master Equations

Below three different approaches for deriving the kinetic equations for the reduced dot density matrix are outlined. In some physical problems it is justified

---

[2] The Hamilton is assumed time-independent.

to consider only the diagonal elements, although correlations between different states might be present. Below this approach will be denoted the (Pauli) Master Equation (ME) approach. However, in other situations the inclusion of the off-diagonal elements of the reduced dot density matrix is crucial, and the set of equations including the off-diagonal elements will be called the Generalized Master Equation (GME) approach.[3]

A much used approach is the so-called Wangness-Bloch-Redfield method (WBR) [28, 36]. Using the von Neumann equation for the density operator one can derive an expression for the density operator [37]

$$\begin{aligned}\rho_{\mathrm{dot}}(t) &= -i\left[H_{\mathrm{dot}}, \rho_{\mathrm{dot}}(t)\right] \\ &- \int_0^\infty \mathrm{d}\tau \mathrm{Tr}\Big[H_T, \Big[e^{-i(H_{\mathrm{dot}}+H_{\mathrm{leads}})\tau} H_T e^{-i(H_{\mathrm{dot}}+H_{\mathrm{leads}})\tau}, \rho_{\mathrm{dot}}(t) \otimes \rho^0_{\mathrm{leads}}\Big]\Big],\end{aligned} \tag{5.6}$$

with ρ^0_{leads} being the density matrix for the isolated, non-interacting leads. In the derivation the "large-reservoir" assumption, i.e. the leads are unaffected by the tunneling between the leads and the dot, has been applied to second order in the tunneling amplitude, restricting Eq. (5.6) to the sequential tunneling limit. Also a Markov approximation has been used, and both approximations will be discussed in Sec. 5.3.[4] By tracing over a complete set of lead states and many-particle states of the dot, a matrix equation for the elements of the reduced dot density matrix is obtained, see, e.g., Ref. [37].

Another route to derive a set of generalized master equations was directed by Gurvitz and Prager [29, 30]. Starting from the many-body Schrödinger wave function, they were able to derive a closed set of equations for the elements of the N-resolved reduced density matrix including the off-diagonal elements, by keeping track of the number N of electrons entering one of the leads. As the GME is N-resolved it gives access not only to the steady-state current, but also to higher-order cumulants such as, e.g., the shot-noise [38]. The method has been applied to tunneling through single, double and multi-dot arrays, also including inelastic processes [29, 30], to nano-electromechanical systems [39, 40], as well as to systems with a quantum dot electrostatically coupled to a quantum point contact, where the latter acts as a charge detector [41].

The method works in a single-particle basis, but is restricted to the high-bias limit. I.e. the energies of all states, E_a, are far away from the chemical potentials of the leads, μ_α, i.e. $\max(k_B T, \Gamma) \ll |E_a - \mu_\alpha|$, but in this limit the

---

[3] When keeping the off-diagonal elements, the resulting set of equations are sometimes also denoted Quantum Master Equations.

[4] In [37] it is shown how to derive an expression valid to higher orders in the tunneling amplitude by using the "large-reservoir" approximation differently.

method is exact.

As a last example, Schoeller and Schön developed a method for diagrammatically deriving a (generalized) master equation for the case of a metallic dot [31], and later König, Schmid, Schoeller, and Schön considered the case of a single quantum dot [32, 33]. This technique is frequently named the Diagrammatic Real-time Transport Theory (DRTT).

The key idea is to consider the quantum mechanical average of a given operator at time t, $A(t)$,

$$\langle A(t)\rangle = \mathrm{Tr}\left[\rho_0 T_K e^{-i\int_K dt' H_T(t')_I} A(t)_I\right], \tag{5.7}$$

where the operators are written in the interaction picture and ρ_0 is the density matrix at t_0. The integral runs along the Keldysh contour from time $t_0 = -\infty$ forward in time to time t, and backward to $t_0 = -\infty$, where T_K is the time-ordering operator along the Keldysh contour.[5] By expanding the exponential in Eq. (5.7) in powers of the tunneling part of the Hamiltonian, $H_T(t)_I$, they can translate the resulting expression into a diagrammatic language similar to Feynman diagrams. They now proceed in two different ways: Either by deriving a generalized master equation in finite-order perturbation theory for the elements of the reduced density matrix of the dot, or by considering also correlations between the leads and the dot by including at most one electron-hole pair, the so-called "resonant tunneling approximation" (RTA). The latter is further discussed in Sec. 5.5.

In the finite-order perturbation theory, they consider the average of the projection operator between the many-particle states χ_1,χ_2, $|\chi_2\rangle\langle\chi_1|$. I.e. the elements of the reduced dot density matrix, $P^{\chi_1}_{\chi_2}(t) = \langle(|\chi_2\rangle\langle\chi_1|)(t)\rangle$. The equation of motion for these elements can be expressed as [42]

$$\frac{\mathrm{d}}{\mathrm{d}t}P^{\chi_1}_{\chi_2}(t) + i(E_{\chi_1} - E_{\chi_2})P^{\chi_1}_{\chi_2}(t) = \sum_{\chi_1'\chi_2'} \int_{t_0}^{t} dt' P^{\chi_1'}_{\chi_2'}(t')\Sigma^{\chi_1',\chi_1}_{\chi_2',\chi_2}(t',t) \tag{5.8}$$

with $\Sigma^{\chi_1',\chi_1}_{\chi_2',\chi_2}(t',t)$ being the irreducible self-energy part of the propagator from χ_1' at time t' forward to χ_1 at time t, and then from χ_2 at time t backward to χ_2' at time t_0.[6] Equation (5.8) is completely general and can also incorporate time-dependent phenomena, but it of course depends on the approximations for the self-energy.

---

[5] Working on the Keldysh contour is similar to the nonequilibrium Green function (NEGF) formalism, see, e.g., [35]. However, in the latter formalism only single-particle operators are considered, while in the DRTT the operators are, e.g., many-body projection operators. Furthermore, in the DRTT only the value of a single operator at one time is evaluated, while in the NEGF formalism, the Green function have a two-time structure.

[6] This is similar to the self-energy in the Dyson equation for Green functions.

For the steady-state limit, they derive an equation satisfied by the elements of the reduced dot density matrix,

$$0 = \sum_{\chi'} P_{\chi'} \Sigma_{\chi',\chi}, \tag{5.9}$$

where they for simplicity only consider the diagonal elements, $P_\chi^\chi = P_\chi$. Expanding both the self-energy and the density-matrix elements in powers of the square of the tunneling amplitude, $|T|^2$, they find to each order p in $|T|^2$ that

$$0 = \sum_{m+m'=p} \sum_{\chi'} P_{\chi'}^{(m)} \Sigma_{\chi',\chi}^{(m')} \tag{5.10}$$

where the self-energy is at least first order in $|T|^2$.[7]

By solving Eq. (5.10) for each order separately, the elements can be calculated to any finite order, and so can the current. In the sequential tunneling regime, the method has been applied to various problems such as spin-valve geometries [43, 44] as well as to the calculation of current noise [45]. Several works including cotunneling processes have been made, e.g., cotunneling at resonance [46], inelastic cotunneling processes [47, 48], models with ferromagnetic leads [49], and also current noise [50, 51].

This order-by-order expansion is very appealing, but might not always be possible as discussed in Chap. 8, where inelastic cotunneling is treated.

In summary, three examples of methods for deriving generalized master equations were presented. They all have in common that only the elements of the reduced dot density matrix are kept, and all effects of the leads have been put into the tunneling rates or, equivalently, the self-energy.

Calculating these rates to arbitrary order in the tunneling coupling allows for an expansion of the dot density matrix elements. To lowest order in the tunneling coupling, the rates correspond to the rates obtained using Fermi's Golden Rule, and the corresponding stationary occupations can be found. Introducing higher-order rates gives corrections to the stationary occupations as well as to any other observable, such as, e.g., the current.

5.3 The second order von Neumann approach

In this section the transport formalism introduced in Paper II is reviewed, although it is presented in a slightly different way. In the coming sections the advantages and disadvantages of the scheme are more thoroughly discussed.

---

[7] T is used for the tunnel amplitude between many-particle states. The temperature is always described by the energy scale $k_B T$ in order to avoid confusion.

The method will below be denoted the 2vN approach. It is an extension of the generalized master equation approach as not only a kinetic equation for the reduced dot density matrix is derived but also a kinetic equation for the elements of the total density matrix consisting of a single electron-hole pair. I.e. the density matrix of the total system is not completely factorized into a lead and a dot part. This resembles the "resonant tunneling approximation" in the DRTT [31, 32, 33], which is discussed in Sec. 5.5.

As above, the physical system in consideration consists of two (or more) leads coupled to a quantum dot. The leads are modelled as non-interacting reservoirs, each having a well-defined chemical potential μ_i and a temperature denoted by the energy $k_B T$. On the dot all kinds of complicated many-body interactions such as, e.g., the Coulomb effect might be present, but it is assumed that without the coupling to the leads, the Hamiltonian of the isolated quantum can be diagonalized and the eigenstates, $|a\rangle$, and corresponding eigenenergies, E_a, are known.

In a many-particle basis, the three terms in the Hamiltonian for the total system in Eq. (5.1) can be written as

$$H_D = \sum_a E_a |a\rangle\langle a|, \tag{5.11}$$

describing the dot, and

$$H_{\text{leads}} = \sum_{k\sigma\ell} E_{k\sigma\ell} c^\dagger_{k\sigma\ell} c_{k\sigma\ell}, \tag{5.12}$$

describing the non-interacting leads, where $\sigma =\uparrow, \downarrow$ denotes the spin, k labels the spatial wave functions of the contact states and ℓ denotes the lead. The last part in the Hamiltonian expresses the tunneling between the states in the leads and the dot[8]

$$H_T = \sum_{k\sigma\ell, ab} \Big[T_{ba}(k\sigma\ell) |b\rangle\langle a| c_{k\sigma\ell} + c^\dagger_{k\sigma\ell} |a\rangle\langle b| T^*_{ba}(k\sigma\ell) \Big] . \tag{5.13}$$

The matrix element $T_{ba}(k\sigma\ell)$ is the scattering amplitude for an electron in the state $k\sigma\ell$ tunneling from the lead onto the dot, thereby changing the dot state from the state $|a\rangle$ to a state $|b\rangle$. Note that this amplitude vanishes unless the number of electrons in state $|b\rangle$, N_b, equals N_a+1. In general states are denoted such that the particle number increases with the position in the alphabet of the denoting letter.

A general state vector for the entire system is written as $|ag\rangle = |a\rangle \otimes |g\rangle$, with $|g\rangle = |\{N_{k\sigma\ell}\}\rangle$ denoting the state of both leads where $N_{k\sigma\ell} \in \{0, 1\}$.

---

[8] How to transform the tunneling Hamiltonian from a single-particle to a many-particle basis is described in Paper II App. A.

To ensure the anti-commutator rules of the operators the following notation is used

- $|\,g-k\sigma\ell\rangle \equiv c_{k\sigma\ell}\,|\,g\rangle$ and $|\,g+k\sigma\ell\rangle \equiv c^{\dagger}_{k\sigma\ell}\,|\,g\rangle$.
  I.e. $|\,g-k\sigma\ell\rangle$ denotes the same set of indices as the state $|\,g\rangle$, but with $N_{k\sigma\ell}$ reduced by one. Furthermore it contains a minus sign depending on the number of occupied states to the left of the position $k\sigma\ell$.
- $|\,gk\sigma\ell\rangle \equiv c^{\dagger}_{k\sigma\ell}c_{k\sigma\ell}\,|\,g\rangle$ and $\big|\,g\overline{k\sigma\ell}\,\big\rangle \equiv c_{k\sigma\ell}c^{\dagger}_{k\sigma\ell}\,|\,g\rangle$. I.e., $|\,gk\sigma\ell\rangle = \delta_{N_{k\sigma\ell},1}|g\rangle$.
- The order of indices is opposite to the order of the operators. E.g. $|\,g-k'\sigma'\ell'+k\sigma\ell\rangle = c^{\dagger}_{k\sigma\ell}c_{k'\sigma'\ell'}\,|\,g\rangle = -c_{k'\sigma'\ell'}c^{\dagger}_{k\sigma\ell}\,|\,g\rangle = -\,|\,g+k\sigma\ell-k'\sigma'\ell'\rangle$ for $k\sigma\ell \neq k'\sigma'\ell'$, which is tacitly assumed, unless stated otherwise.

To simplify the notation, $\sigma\ell$ is only attached to k the first time the index k appears in the equation, and below it is implicitly assumed to be connected with k. Furthermore, the convention is applied that $\sum_{k\sigma(\ell)}$ means summing over k and σ with a fixed ℓ, which is being connected to k in this sum.

The density matrix elements are defined as $\rho^{[n]}_{ag;bg'} = \langle ag\,|\,\hat{\rho}\,|\,bg'\rangle$ and compared to the derivation in Paper II, the notation has been extended by attaching a label, n. It is defined as the total number of electron-hole pairs (ehp) involved in the two states $|\,bg'\rangle$ and $|\,ag\rangle$, e.g., $\rho^{[1]}_{bg-k;ag}$ and $\rho^{[2]}_{cg-k;ag+k'}$, where holes can be in the leads or on the dot. In other words, n counts the number of different k-states present in the density matrix element, and the elements are denoted n-ehp elements.

The time-evolution of the elements of the density matrix is governed by the von Neumann equation

$$i\hbar\frac{\mathrm{d}}{\mathrm{d}t}\rho^{[n]}_{ag;bg'} = \langle ag\,|\,H\rho-\rho H\,|\,bg'\rangle \tag{5.14}$$

Note that the method is formulated in the Schrödinger picture, while in other works, the density matrix is often transformed to the interaction picture, $\rho(t)_I = e^{iH_Tt}\rho(t)e^{-iH_Tt}$, and the time evolution and the approximations are performed in the interaction picture, see, e.g., [28, 32, 33]. This will be further discussed Sec. 5.5.

The particle current from the left lead into the structure, J_L, equals the rate of change of the occupations in the left lead. This gives

$$\begin{aligned} J_L &= -\frac{\mathrm{d}}{\mathrm{d}t}\sum_{k\sigma(L)}\left\langle c^{\dagger}_{k}c_{k}\right\rangle = -\frac{\mathrm{d}}{\mathrm{d}t}\sum_{k\sigma(L)}\rho^{[0]}_{bg,bgk} \\ &= -\frac{2}{\hbar}\sum_{k\sigma(L),cb}\Im\left\{\sum_{g}T^{*}_{cb}(k)\rho^{[1]}_{cg-k;bg}\right\}, \end{aligned} \tag{5.15}$$

i.e. the current is expressed in terms of off-diagonal elements of the total density matrix connecting two dot states, where the number of electrons differ by one.

Without any approximations, the equations of motion for the 0-ehp and 1-ehp elements read

$$\begin{aligned} i\hbar\frac{\mathrm{d}}{\mathrm{d}t}\rho^{[0]}_{bg;b'g} =&(E_b - E_{b'})\rho^{[0]}_{bg;b'g} \\ &+ \sum_{a,k\sigma\ell} T_{ba}(k)\rho^{[1]}_{ag+k;b'g} + \sum_{c,k\sigma\ell} T^*_{cb}(k)\rho^{[1]}_{cg-k;b'g} \\ &- \sum_{c,k\sigma\ell} \rho^{[1]}_{bg;cg-k}T_{cb'}(k) - \sum_{a,k\sigma\ell} \rho^{[1]}_{bg;ag+k}T^*_{b'a}(k), \end{aligned} \tag{5.16}$$

$$\begin{aligned} i\hbar\frac{\mathrm{d}}{\mathrm{d}t}\rho^{[1]}_{cg-k\sigma\ell;bg} &= (E_c - E_b - E_k)\rho^{[1]}_{cg-k;bg} \\ &+ \sum_{b'} T_{cb'}(k)\rho^{[0]}_{b'gk;bg} - \sum_{c'} \rho^{[0]}_{cg-k;c'g-k}T_{c'b}(k) \\ &+ \sum_{k'\sigma'\ell'} \Big[\sum_{b'} T_{cb'}(k')\rho^{[2]}_{b'g-k+k';bg} + \sum_{d} T^*_{dc}(k')\rho^{[2]}_{dg-k-k';bg} \\ &\qquad - \sum_{c'} \rho^{[2]}_{cg-k;c'g-k'}T_{c'b}(k') - \sum_{a} \rho^{[2]}_{cg-k;ag+k'}T^*_{ba}(k')\Big]. \end{aligned} \tag{5.17}$$

Note how the 1-ehp density matrix element is coupled to elements with n equal to 0 and 2, but it does not couple to other 1-ehp elements.

The equation of motion for the 2-ehp elements is derived similarly, but here the first approximation is used: (i) only coherent processes involving transitions of at most two different k-states are considered. For the first element in the square bracket in Eq. (5.17) this gives (the expressions for the other 2-ehp elements can be found in Paper II App. B.)

$$\begin{aligned} i\hbar\frac{\mathrm{d}}{\mathrm{d}t}\rho^{[2]}_{b'g-k\sigma\ell+k'\sigma'\ell';bg} &= (E_{b'} + E_{k'} - E_b - E_k)\rho^{[2]}_{b'g-k+k';bg} \\ &- \sum_{a} T_{b'a}(k)\rho^{[1]}_{agk+k';bg} + \sum_{c'} T^*_{c'b'}(k')\rho^{[1]}_{c'g-k\overline{k'};bg} \\ &- \sum_{c'} \rho^{[1]}_{b'g-k+k';c'g-k}T_{c'b}(k) - \sum_{a} \rho^{[1]}_{b'g-k+k';ag+k'}T^*_{ba}(k') \end{aligned} \tag{5.18}$$

Neglecting elements with $n \geq 3$ lead to a closed set of equations, where the 2-ehp elements only depend on themselves and 1-ehp elements.

For all three types of density matrix elements, $\rho^{[n]}_{ag;bg}$ with $n = 0, 1, 2$, a sum over all possible lead configurations, $\sum_g$, is carried out and the following notation is introduced[9]

$$
\begin{aligned}
\Phi^{[0]}_{b'b} &= \sum_g \rho^{[0]}_{b'g;bg}, && (5.19)\\
\Phi^{[1]}_{ba}(k\sigma\ell) &= \sum_g \rho^{[1]}_{bg-k;ag}, && (5.20)\\
\Phi^{[2]}_{ca}(-k\sigma\ell;+k'\sigma'\ell') &= \sum_g \rho^{[2]}_{cg-k\sigma\ell;ag+k'\sigma'\ell'}. && (5.21)
\end{aligned}
$$

Keeping the numbering of the approximations as in Paper II, the third(!) approximation is invoked, saying that (iii) the level occupations in the leads, $f_{k\sigma\ell}$, are unaffected by the couplings to the dot, i.e. the densities in the leads and on the dot can be factorized. It means that for states requiring a specific k-state being occupied or empty, the approximation

$$
\sum_g \rho_{b'gk;bg} = \sum_g \delta_{N_k,1}\rho_{b'g;bg} \approx f_k \sum_g \rho_{b'g;bg} = f_k \Phi^{[0]}_{b'b}, \tag{5.22}
$$

is applied, and similar for the empty states.

The resulting expressions for the 0- and 1-ehp elements, together with an example of a 2-ehp element, Eqs. (5.16)-(5.18), read[10]

$$
\begin{aligned}
i\hbar\frac{\mathrm{d}}{\mathrm{d}t}\Phi^{[0]}_{bb'} = (E_b - E_{b'})\Phi^{[0]}_{bb'} &+ \sum_{a,k\sigma\ell}\Big(T_{ba}(k)[\Phi^{[1]}_{b'a}(k)]^* - \Phi^{[1]}_{ba}(k)T^*_{b'a}(k)\Big)\\
&+ \sum_{c,k\sigma\ell}\Big(T^*_{cb}(k)\Phi^{[1]}_{cb'}(k) - [\Phi^{[1]}_{cb}(k)]^*T_{cb'}(k)\Big)
\end{aligned} \tag{5.23}
$$

$$
\begin{aligned}
i\hbar\frac{\mathrm{d}}{\mathrm{d}t}\Phi^{[1]}_{cb}(k\sigma\ell) &= (E_c - E_b - E_k)\Phi^{[1]}_{cb}(k\sigma\ell)\\
&+ \sum_{b'} T_{cb'}(k) f_k \Phi^{[0]}_{b'b} - \sum_{c'}\Phi^{[0]}_{cc'}(1-f_k)T_{c'b}(k)\\
&+ \sum_{k'\sigma'\ell'}\Big[\sum_{b'}T_{cb'}(k')\Phi^{[2]}_{b'b}(-k+k';0) + \sum_d T^*_{dc}(k')\Phi^{[2]}_{db}(-k-k';0)\\
&\qquad - \sum_{c'}\Phi^{[2]}_{cc'}(-k;-k')T_{c'b}(k') - \sum_a \Phi^{[2]}_{ca}(-k;+k')T^*_{ba}(k')\Big],
\end{aligned} \tag{5.24}
$$

$$
\begin{aligned}
i\hbar\frac{\mathrm{d}}{\mathrm{d}t}\Phi^{[2]}_{b'b}(-k\sigma\ell+k'\sigma'\ell';0) &= (E_{b'} + E_{k'} - E_b - E_k)\Phi^{[2]}_{b'b}(-k+k';0)\\
&- \sum_a f_k T_{b'a}(k)[\Phi^{[1]}_{ba}(k')]^* + \sum_{c'}(1-f_{k'})T^*_{c'b'}(k')\Phi^{[1]}_{c'b}(k)\\
&- \sum_{c'}[\Phi^{[1]}_{c'b'}(k')]^*(1-f_k)T_{c'b}(k) - \sum_a \Phi^{[1]}_{b'a}(k)f_{k'}T^*_{ba}(k'),
\end{aligned} \tag{5.25}
$$

---

[9] In Paper II, $\Phi^{[0]}_{b'b}$ and $\Phi^{[1]}_{ba}(k\sigma\ell)$ are denoted $w_{b'b}$ and $\phi_{ba}(k\sigma\ell)$, respectively.

[10] See Paper II App. B for details.

The 0-ehp elements are the elements of the reduced dot density matrix also contained in the generalized master equation approach as outlined in Sec. 5.2. Elements with $n \geq 1$ include correlations between the lead and the dot states, and can be viewed as expectation values for coherent superpositions between states located in the leads and on the dot.

Defining a discrete set of k-states, one can set up a column vector consisting of all the elements of the density-matrix $\mathbf{\Phi} = \left(\mathbf{\Phi}^{[0]}, \mathbf{\Phi}^{[1]}, \mathbf{\Phi}^{[2]}\right)$, where the sub-vectors contain all the elements of the density-matrix with a specific n-value, as well as the complex conjugates of the complex elements. The equation of motion for the vector $\mathbf{\Phi}$ can be cast on a matrix form[11]

$$i\hbar \frac{\mathrm{d}}{\mathrm{d}t}\mathbf{\Phi} = \begin{pmatrix} \underline{\underline{\mathbf{E}}}_{00} & \underline{\underline{\mathbf{M}}}_{01} & \underline{\underline{\mathbf{0}}} \\ \underline{\underline{\mathbf{M}}}_{10} & \underline{\underline{\mathbf{E}}}_{11} & \underline{\underline{\mathbf{M}}}_{12} \\ \underline{\underline{\mathbf{0}}} & \underline{\underline{\mathbf{M}}}_{21} & \underline{\underline{\mathbf{E}}}_{22} \end{pmatrix} \mathbf{\Phi} = \underline{\underline{\mathbf{M}}}\mathbf{\Phi}. \tag{5.26}$$

The submatrices $\mathbf{E}_{nn}$ are diagonal and contain the energy differences between the states involved, see Eqs. (5.23)-(5.25).

In Paper II the derivation continues by using the second assumption, (ii), that the time dependence of terms generating two-electron transition processes is neglected, which corresponds to the Markov limit [52]. I.e. $i\hbar\frac{\mathrm{d}}{\mathrm{d}t}\mathbf{\Phi}^{[2]} = \mathbf{0}$, and then solve for the stationary $\mathbf{\Phi}^{[2]}$, which depends only on $\mathbf{\Phi}^{[1]}$. As an example, Eq. (5.25) gives[12]

$$\begin{aligned} \Phi^{[2]}_{b'b}(-k\sigma\ell + k'\sigma'\ell'; 0) = {} & \frac{1}{E_{b'} + E_{k'} - E_b - E_k + i0^+} \\ & \times \Big\{ -\sum_a f_k T_{b'a}(k) \left[\Phi^{[1]}_{ba}(k')\right]^* + \sum_{c'} (1 - f_{k'}) T^*_{c'b'}(k') \Phi^{[1]}_{c'b}(k) \\ & - \sum_{c'} \left[\Phi^{[1]}_{c'b'}(k')\right]^* (-f_k) T_{c'b}(k) - \sum_a \Phi^{[1]}_{b'a}(k) f_{k'} T^*_{ba}(k') \Big\}. \end{aligned} \tag{5.27}$$

Inserting the result in Eq. (5.26) leads to an expression for the time-dependence of the vector $\tilde{\mathbf{\Phi}} = \left(\mathbf{\Phi}^{[0]}, \mathbf{\Phi}^{[1]}\right)$,

$$i\hbar \frac{\mathrm{d}}{\mathrm{d}t}\tilde{\mathbf{\Phi}} = \begin{pmatrix} \underline{\underline{\mathbf{E}}}_{00} & \underline{\underline{\mathbf{M}}}_{01} \\ \underline{\underline{\mathbf{M}}}_{10} & \underline{\underline{\mathbf{M}}}_{11} \end{pmatrix} \tilde{\mathbf{\Phi}} = \underline{\underline{\tilde{\mathbf{M}}}}\tilde{\mathbf{\Phi}}. \tag{5.28}$$

where the sub-matrix $\underline{\underline{\mathbf{M}}}_{11}$ is not diagonal. I.e. it is not possible to express $\mathbf{\Phi}^{[1]}$ solely in terms of $\mathbf{\Phi}^{[0]}$ thereby reducing the problem to a generalized master equation.

---

[11] The matrix $\underline{\underline{\mathbf{M}}}$ is sometimes denoted a superoperator, as it acts on the density matrix, and not on a state vector.

[12] A factor of $-i0^+\Phi^{[2]}_{b'b}(-k\sigma\ell + k'\sigma'\ell'; 0)$ has been added to ensure decay of initial conditions as $t_0 \to -\infty$.

The explicit, and completely general, expression for the equation of motion for the elements in the vector $\tilde{\mathbf{\Phi}}$ is found in Eqs. (10)-(11) in Paper II, and is the main result of that paper.

Inspecting the structure of the equation of motion for the 0- and 1-ehp elements shows that they have the generic structure

$$\begin{aligned} i\hbar\frac{\mathrm{d}}{\mathrm{d}t}\Phi^{[0]}_{bb'} &= (E_b - E_{b'})\Phi^{[0]}_{bb'} + \sum T\Phi^{[1]}, && (5.29)\\ i\hbar\frac{\mathrm{d}}{\mathrm{d}t}\Phi^{[1]}(k) &= (E_c - E_b - E_k)\Phi^{[1]}(k) + \sum \left[f_k T\Phi^{[0]}_{cb} - (1-f_k)T\Phi^{[0]}_{c'b'}\right] \\ &\quad + \sum_{k'}\left[\frac{f_k TT^{(*)}}{\Delta E - E_k \pm E_{k'}}\Phi^{[1]}_{ji} - \frac{(1-f_k)TT^{(*)}}{\Delta E - E_k \pm E_{k'}}\Phi^{[1]}_{lk}\right], && (5.30) \end{aligned}$$

with ΔE being the energy difference between two dot states involved. That is in Eq. (5.28) the sub-matrices $\underline{\underline{\mathbf{M}}}_{10}$ and $\underline{\underline{\mathbf{M}}}_{01}$ contain elements proportional to the tunneling amplitude T, and the matrix $\underline{\underline{\mathbf{M}}}_{11}$ involves terms proportional to T^2. Solving for the stationary $\tilde{\mathbf{\Phi}}$ together with the normalization $\sum_b \Phi^{[0]}_{bb} = 1$, involves inversion of the matrix $\underline{\underline{\tilde{\mathbf{M}}}}$, and the resulting inverse matrix will contain all powers of T, and so will the stationary occupations and coherences. Consequently, this is not a systematic expansion in powers of the tunneling coupling.

This contrasts, e.g., the generalized master equation approach in the sequential tunneling approximation, where all terms in the kinetic equation related to scattering between the dot states are proportional to $|T|^2$. Upon inverting the matrix, the occupations become zeroth-order in $|T|^2$, and the resulting current is proportional to $|T|^2$, i.e. the coupling strength Γ.

In conclusion, the standard generalized master equation scheme has been extended by also deriving a kinetic equation for the elements of the total density matrix involving states with at most a single electron-hole pair. In deriving the latter equation, all processes including up to two electron-hole pairs are taken into account, but in the kinetic equation for those elements approximations were made in order to close the equations.

The resulting set of equations do not give a systematic expansion of the 0- and 1-ehp elements in powers of the tunneling amplitude, but is rather a non-perturbative approach, as some coherent processes between the leads and the dots are fully kept.

In the next section the applied approximation scheme is discussed in more detail.

5.4 The applied approximation scheme in the 2vN approach

In deriving the closed set of equations for the elements of the total density matrix involving zero or a single electron-hole pair, Eq. (5.28), three approximations were applied; (i) only coherent processes involving transitions of at most two different k-states are considered, (ii) the time-dependence of terms generating two-electron transition processes is neglected, which corresponds to the Markov limit [52], and (iii) the level occupations in the leads, $f_{k\sigma\ell}$, is unaffected by the couplings to the dot, i.e. the densities in the leads and on the dot can be factorized.

The first approximation is necessary in order to truncate the equation of motion for the total density matrix, i.e. the Liouville space is restricted to only contain elements with a total of at most two electron-hole pairs. The physical motivation behind is that if the coupling between the leads and the dot is sufficiently weak, the states containing three or more electrons-hole pairs decay so fast that the dynamics of the elements with up to 2 electron-hole pairs are unaffected by these terms, i.e., $\rho^{[3]}(t) \simeq 0$. The validity of the assumption depends on the time-scale between consecutive tunneling events (set by $1/\Gamma$) and the temperature of the leads which determine the decay time of the excitations in the leads. As a consequence, this assumption is assumed to break down for temperatures much lower than the coupling constant. The applicability of the assumption also depends on the geometry of the contacts.

The third approximation is also related to the properties of the leads. If the leads are assumed to be large reservoirs, the occupations of the lead states are unaffected by the coupling to the dot, and an effective decoupling is performed, $\rho \approx \rho_{\text{leads}} \otimes \rho_{\text{dot}}$. This is only valid if the relaxation time of the leads is short compared to the time between consecutive tunneling events.

The second approximation is only applied to the elements with two electron-hole pairs. In the kinetic equation for these elements, they are, due to the first assumption, coupled solely to one electron-hole pair elements. The assumption is that the 1-ehp elements are evolving slowly in time compared to the 2-ehp elements, and consequently can be considered as local in time. I.e. in the solution of Eq. (5.18),

$$
\begin{aligned}
\rho^{[2]}_{b'g-k\sigma\ell+k'\sigma'\ell';bg}(t) &= \frac{1}{i\hbar}\int_{-\infty}^{t} \mathrm{d}t' e^{(E_b+E_k-E_{b'}E_{k'}+i0^+)(t-t')/\hbar} \\
&\qquad \times \big[-\sum_a T_{b'a}(k)\rho^{[1]}_{agk+k';bg}(t')+...\big] \\
&\simeq \frac{1}{i\hbar}\big[-\sum_a T_{b'a}(k)\rho^{[1]}_{agk+k';bg}(t)+...\big] \\
&\qquad \int_{-\infty}^{t} \mathrm{d}t' e^{(E_b+E_k-E_{b'}E_{k'}+i0^+)(t-t')/\hbar},
\end{aligned}
\tag{5.31}
$$

where the assumption $\rho^{[1]}_{agk+k';bg}(t') \simeq \rho^{[1]}_{agk+k';bg}(t)$ has been used, which allows for an analytic evaluation of the integral. The assumption becomes exact in the stationary limit.

If the above mentioned approximations are valid, it was proven analytically in Paper II that for a single spinless level the method gives the exact result for the stationary current. For the non-interacting Anderson model and the non-interacting double quantum dot structure, it was verified numerically that the exact results are obtained.

The validity of the approach for time-dependent problems has not been carefully investigated. As the Markov approximation is invoked, it might not be valid for strongly time-dependent systems, where non-Markovian effects are important due to memory effects, which are also relevant when evaluating higher-order moments, such as e.g., the noise [51, 53]. As an example, the current through a single spinless level was presented in Paper II Sec. III.

5.5 Comparison with other methods

Two different cases are considered. Either an expansion to lowest order in the lead-dot coupling, i.e. the sequential tunneling regime, or the full 2vN approach. Both will be discussed below.

The sequential tunneling expression for the reduced dot density matrix elements is derived by neglecting the 2-ehp elements in the square-bracket in Eq. (5.24), and the resulting equation of motion for $\Phi^{[1]}_{cb}$ only depends on 0-ehp elements. I.e. in Eq. (5.28) the sub-matrix $\underline{\underline{\mathbf{M}}}_{11}$ has been replaced by the diagonal sub-matrix $\underline{\underline{\mathbf{E}}}_{11}$. Taking the stationary limit, $i\hbar\frac{\mathrm{d}}{\mathrm{d}t}\Phi^{[1]}_{cb} = 0$, and inserting the expression into the equation of motion for the 0-ehp elements, it ends up with a kinetic equation solely for the elements of the reduced dot density matrix, $\Phi^{[0]}_{bb'}$, where all terms describing scattering are proportional to $|T|^2$. The resulting set of generalized master equations is shown in Paper III App. A and is denoted the first-order von Neumann (1vN) result.

The generalized master equations in the 1vN approach is similar to the set derived using the WBR approach (or the DRTT technique).[13] However, in the 1vN approach the time evolution of the density matrix elements is done in the Schrödinger picture, while in the WBR approach the time evolution is performed in the interaction picture, which gives a difference due to the Markov approximation for the off-diagonal elements $\Phi^{[0]}_{bb'}(t')$:
Solving Eq. (5.24) while neglecting the 2-ehp elements, gives

$$\Phi^{[1]}_{cb}(k\sigma\ell)(t) = \frac{1}{i\hbar}\int_{-\infty}^{t} \mathrm{d}t' \mathrm{e}^{i(E_b+E_k-E_c+i0^+)(t-t')/\hbar} \left[\sum_{b'} T_{cb'}(k)\Phi^{[0]}_{b'b}(t')f_k - \sum_{c'} \Phi^{[0]}_{cc'}(t')T_{c'b}(k)(1-f_k)\right] \tag{5.32}$$

In the 1vN approach, the procedure continues as for the 2-ehp elements in the 2vN approach in Eq. (5.31) by approximating $\Phi^{[0]}_{b'b}(t') \simeq \Phi^{[0]}_{b'b}(t)$ and then perform the integral analytically. This approach is exact in the stationary limit. Another possibility is that the off-diagonal elements, describing a superposition between the two dot states with different energies, oscillate according to $\Phi^{[0]}_{b'b}(t') \simeq \Phi^{[0]}_{b'b}(t)e^{-i(E_{b'}-E_b)(t-t')/\hbar}$, which also allows for an analytic evaluation of the integral. The latter approximation corresponds to evolving the density matrix in time and applying the Markov approximation in the interaction picture, as in the WBR approach.

The difference between the 1vN and the WBR approaches results in slightly different energy denominators for the WBR equation system compared to the expression found in Eq. (A2) in Paper III. As a consequence the occupations of the lead states are evaluated at different energies, but in the high-bias limit the results of the methods are identical. For the double quantum dot system described in Chap. 6, only minor numerical differences between the two approximation schemes are found, even at finite bias.[14]

An approach which also goes beyond the order-by-order expansion was, as mentioned in Sec. 5.2, derived by Schoeller *et al.* in the framework of the diagrammatic real-time transport theory (DRTT), which is the so-called resonant tunneling approximation (RTA). In the RTA approximation, elements in the full density matrix of the system consisting of up to a single electron-hole

---

[13] According to Ref. [37] an extension of WBR to higher-order in the tunneling coupling and the DRTT approach give identical results to all orders in the tunneling coupling in an order-by-order expansion.

[14] For a further discussion of these issues, see Ref. [54].

pair are kept, similar to the $\rho^{[1]}_{cg-k,b}$ elements in the 2vN approach. For the single-level Anderson model with spin-degenerate levels and infinite Coulomb repulsion, it was shown in Paper III that exactly the same analytic expression is obtained using both methods. However, as they derive a propagator for the elements on the Keldysh contour, a direct comparison for arbitrary model systems is difficult. A possible difference between the methods might be that the DRTT-RTA is formulated in the interaction picture, which might give the same deviation between the methods as for the first-order results presented above.[15] The advantage of the 2vN scheme could be that it gives a closed expression valid for arbitrary model systems, see Eqs. (10),(11) in Paper II.

The DRTT-RTA was originally developed for metallic dots [31], and later used to explain experiments [56, 57] on a single quantum defect in point contacts showing Kondo physics, [32, 33, 42]. It was found that it gave reasonable results for temperatures smaller than the Kondo temperature, but it was not valid all the way to zero temperature. Later the DRTT-RTA method was applied to explain experiments on a single quantum dot in the Coulomb blockade regime, where the barriers were very asymmetric. The broadening at the onset of the current showed a clear dependence on the direction of the bias [58].[16] Finally, Utsumi *et al.* considered a single-level quantum dot coupled to ferromagnetic leads and extended the DRTT-RTA by including further diagrams to account for the level renormalization and the splitting of the Kondo peak in nonequilibrium situations [59].[17]

In a recent paper, Jin *et al.* also consider quantum transport in the same spirit as in the 2vN approach by keeping correlations between the leads and the dot by performing an expansion in the tunneling Hamiltonian [60]. They report a proof that they obtain the 2vN approach as an expansion to second order.

5.6 Discussion and conclusion

In summary, a method was presented which goes beyond the standard generalized master equation approach by not only considering the elements of the reduced dot density matrix, but also taking the elements with a single electron-hole pair into account. Thereby higher-order effects, such as interference or

---

[15] For the single spinless level it can be proven that the 2vN approximation scheme gives the exact result, while the alternative derivation, as presented for the 1vN approach, is only exact in the wide-band limit (Paper III and [55]). We are not sure about the result of the DRTT-RTA method.

[16] The exact same results would have been obtained using the 2vN approach.

[17] An interesting problem could be to figure out if this level renormalization is contained in the 2vN scheme.

cotunneling, can be treated and temperatures below the scale set by the coupling constant can be accessed, $\Gamma/k_BT \geq 1$. Moreover, it can describe some features in the low-temperature regime where strong correlations between the lead and the dot electrons are present, although not being able to fully account for strong-coupling effects such as, e.g., the Kondo effect. Interactions on the dot are treated exactly by working in a basis of many-particle states. Finally, the set of equations presented in Eqs. (10),(11) in Paper II are completely general and can be applied to any model system where the many-body eigenstates of the dot and the coupling to leads are known. This allows, in principle, for a straightforward numerical implementation.

The disadvantage of the method is the complexity and how it scales with the number of single-particle states. A system with N single-particle states has $\sum_{M=0}^{N} \frac{N!}{M!(N-M)!} = 2^N$ many-particle states, and the number of elements in the reduced dot density matrix will be at most[18]

$$\text{No of } \Phi^{[0]}s = \sum_{M=0}^{N} \left[\frac{N!}{M!(N-M)!}\right]^2 = \frac{4^N\Gamma(N+\frac{1}{2})}{\sqrt{\pi}N!}, \tag{5.33}$$

as only superpositions between states with the same number of electrons are non-vanishing. This number is the maximum dimension of the Liouville-space of the generalized master equations, and the number of elements in the matrix describing the transition is the square of this number.

The 2vN approach contains the same number of 0-ehp elements plus an additional number of 1-ehp elements. The latter connect the many-particle states with M and $M-1$ electrons, giving at most

$$\begin{aligned}\text{No of } \Phi^{[1]}s &= \sum_{M=1}^{N} \left[\frac{N!}{M!(N-M)!}\right]\left[\frac{N!}{(M-1)!(N-M+1)!}\right] \\ &= \frac{N4^N}{(N+1)!}\frac{\Gamma(N+\frac{1}{2})}{\sqrt{\pi}}.\end{aligned} \tag{5.34}$$

This number should then be multiplied by the number of k-states in the discretization, and it should be taken into account that the $\Phi^{[1]}$s are complex. For a system with $N = 1, 2, 3, 4, 5, 6, \ldots$ single-particle states, there are the possibility of $2, 6, 20, 70, 252, 924, \ldots$ $\Phi^{[0]}$-elements, and $1, 4, 15, 56, 210, 792, \ldots$ $\Phi^{[1]}$-elements, where the latter should be multiplied by the number of k-states. However, for a specific model system the number of both 0- and 1-ehp elements will be significantly reduced due to, e.g., spin selection rules.

This gives, even for a relative small number of single-particle states, a huge number of density matrix elements, where a direct matrix inversion is untractable. When solving the equations, the discrete set of k-states was changed

---

[18] In this section Γ denotes the Gamma function.

to an energy integral $\sum_k \rightarrow \int dE \sum_k \mathcal{D}(E)\delta(E-E_k)$ with $\mathcal{D}(E)$ being the density of states, transforming the problem from matrix inversion to solving a set of coupled integro-differential equations.[19]

Another important issue is about the mathematical foundation for density-matrix based approaches. Loosely formulated, it is required of the kinetic equation for the reduced dot density matrix that at all times it preserves the hermicity, the sum of all eigenvalues are 1, and the density-matrix stays a positive-definite matrix [36, 61]. This assures that the eigenvalues, i.e. the probabilities for the occupations of the dot states, are real, bound to the interval $[0,1]$, and the sum of all probabilities equals one. If the parameters in the kinetic equation are time-independent, there exists a most general form for the equation of motion established by Lindblad in 1976 [36, 62].

However, for tens of years it has been known that Wangness-Bloch-Redfield types of derivations of the kinetic equation for the density matrix, based on a microscopic Hamiltonian, may cause negative occupation probabilities and frequently does so, see Ref. [61] and references therein. Possible cures have been proposed, especially in the context of two-level systems coupled to an environment [61, 63]. Negative probabilities have frequently been observed using the 1vN approach and in some, but rare occasions, also for the 2vN approach. The latter problem is further discussed in Chap. 8.

In Chap. 6-8 the 2vN approach is applied to various model systems.

---

[19] For an example, see Paper II Sec. III.

6

The double quantum dot

When a discrete level is coupled to a continuum of states, it gets broadened in energy and shifted due to level renormalization [64]. The simple physical picture is that when coupled to the continuum of states, the discrete level is no longer an eigenstate of the system. That is if the system is initially in the discrete state, say before the coupling is switched on, the state will decay in time when the coupling is present. Following standard second-order perturbation theory, the decay of the state is associated with a finite energy width and the level energy gets shifted. When considering a tunneling set up, the situation gets further complicated due to the filled states in the leads and the many-body interactions on the dot.

Much experimental and theoretical work has addressed the properties of transport through single quantum dots, and as a natural extension also the properties of coupled quantum dots and even quantum dot arrays have been widely studied [29, 30, 65]. In this chapter the serial double quantum dot (DQD) is studied, see Fig. 6.1. The system is interesting because it offers the possibility to study the interplay between the internal coherent oscillations between the dot states and the influence of the coupling to leads, the latter inducing broadening of the levels and level renormalization. In this chapter, the focus is in particular on negative differential conductance (NDC) in DQDs due to this interplay. Previous work is reviewed and results obtained using the 1vN and 2vN formalisms presented in Chap. 5 are shown. The content of this chapter is extracted from Paper III.

6.1 The DQD Hamiltonian and a simple example

In order to simplify the discussion, in the rest of this chapter only spinless electrons are considered, which can be realized physically by applying a large magnetic field. Each dot is assumed to contain only a single level contributing

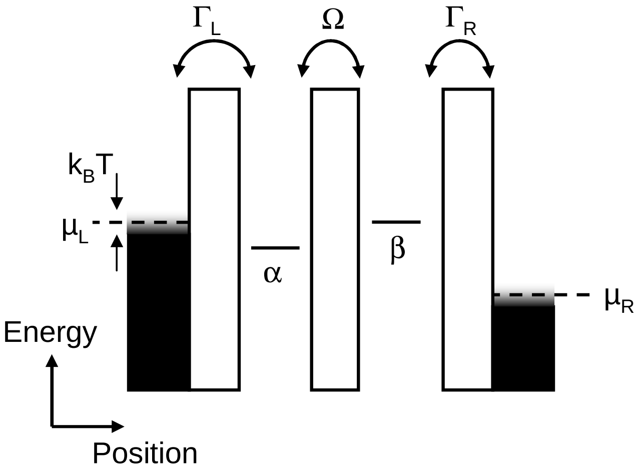

Figure 6.1: Sketch of a serial double quantum dot.

to the transport. Under these assumptions the Hamiltonian can be written as

$$\begin{aligned} H =& E_\alpha d_\alpha^\dagger d_\alpha + E_\beta d_\beta^\dagger d_\beta + U d_\alpha^\dagger d_\alpha d_\beta^\dagger d_\beta + \left(\Omega d_\beta^\dagger d_\alpha + h.c\right) \\ &+ \sum_{k\ell} E_{k\ell} c_{k\ell}^\dagger c_{k\ell} + \sum_k \left(t_{kL} d_\alpha^\dagger c_{kL} + t_{kR} d_\beta^\dagger c_{kR} + h.c.\right), \end{aligned} \tag{6.1}$$

with U being the Coulomb energy for occupying both dots, Ω the inter-dot tunneling coupling and α/β denoting the left/right dot, respectively. The first term in the second line accounts for the leads, with index $\ell = L/R$ for the left/right lead, and levels counted by k. The last term is the lead-dot tunneling coupling. The lead-dot coupling parameters $t_{k\ell}$ are parametrized by $\Gamma_\ell(E) = 2\pi \sum_k |t_{k\ell}|^2 \delta(E - E_{k\ell})$. Here the constant value Γ_ℓ is used for $|E| \leq 0.95W$ and $\Gamma_\ell(E) = 0$ for $|E| > W$. For $0.95W < |E| < W$ interpolation with an elliptic behavior is applied in order to avoid discontinuities. Furthermore, the total coupling is defined as $\Gamma = \Gamma_L + \Gamma_R$.[1]

Before applying the 1vN and 2vN methods it is necessary to diagonalize the double dot part of the Hamiltonian and obtain the many-particle eigenstates

---

[1] This is not the usual convention for the coupling in DQDs as the levels in each dot are broadened by Γ_α, $\alpha = L, R$, rather than the sum of the two. However, here the convention used in Paper III is applied.

and their energies. The many-particle energies are

$$
\begin{aligned}
E_0 &= 0, && \text{(empty state)} \quad (6.2)\\
E_1 &= \frac{1}{2}\left(\rho - \sqrt{\Delta^2 + 4\Omega^2}\right), && \text{(bonding state)} \quad (6.3)\\
E_2 &= \frac{1}{2}\left(\rho + \sqrt{\Delta^2 + 4\Omega^2}\right), && \text{(anti-bonding state)} \quad (6.4)\\
E_d &= E_\alpha + E_\beta + U = E_1 + E_2 + U, && \text{(double-occupied state)}, \quad (6.5)
\end{aligned}
$$

with $\rho = E_\alpha + E_\beta$ and the detuning $\Delta = E_\alpha - E_\beta$. The corresponding (normalized) eigenvectors are

$$
\begin{aligned}
|\,1\rangle &= \tfrac{1}{\sqrt{1+C_-^2}}\left[C_-\,|\,\alpha\rangle + |\,\beta\rangle\right]\\
|\,2\rangle &= \tfrac{1}{\sqrt{1+C_+^2}}\left[C_+\,|\,\alpha\rangle + |\,\beta\rangle\right]
\end{aligned}
\tag{6.6}
$$

with $C_\pm = \frac{\Delta \pm \sqrt{\Delta^2+4\Omega^2}}{2\Omega}$. From the many-particle states the tunneling matrix elements $T_{ba}(k\ell)$ can be obtained using the procedure described in Paper II App. A. In the rest of this chapter, only symmetric bias $\mu_L = -\mu_R = eV/2$ is considered.

Current will flow through the system whenever a one-particle excitation becomes energetically allowed and is effectively blocked when no one-particle excitations are within the bias window. As there are four possible single-particle transitions ($|\,0\rangle \leftrightarrow |\,1\rangle, |\,2\rangle$, and $|\,1\rangle, |\,2\rangle \leftrightarrow |\,d\rangle$), at most four steps can be observed in the IV-curve.

Below the 1vN and 2vN results are benchmarked against the results obtained using the generalized master equations by Gurvitz *et al.* and Stoof *et al.* in the limit where only the transitions $|\,0\rangle \leftrightarrow |\,1\rangle, |\,2\rangle$ are allowed [29, 66]

$$
I_1 = \frac{e}{\hbar}\frac{\Omega^2\Gamma_R}{\Omega^2(2+\Gamma_R/\Gamma_L) + (\Gamma_R/2)^2 + \Delta^2}, \tag{6.7}
$$

and in the limit where all excitations are within the bias window (Elatari *et al.* [38])

$$
I_2 = \frac{e}{\hbar}\frac{\Gamma_L\Gamma_R\Gamma\Omega^2}{(4\Omega^2 + \Gamma_L\Gamma_R)(\Gamma/2)^2 + \Delta^2\Gamma_L\Gamma_R}. \tag{6.8}
$$

These formulas are exact in the limit where all allowed single-particle excitations are well inside the bias window. That is for a transition from a dot state with N electrons to a state with $(N+1)$-electrons, the addition energy $E_{N+1} - E_N$ is further away from both chemical potentials of the leads, μ_ℓ, than the sum of the broadening due the leads and the temperature, $|(E_{N+1} -$

$E_N) - \mu_\ell| \gg k_B T + \Gamma$. Furthermore, the Eqs. (6.7)-(6.8) were derived under the assumption that the current flows from the left to the right lead.[2]

As an example consider Fig. 6.2, where the simple expressions are compared to the full 2vN calculation. As $\rho = E_\alpha + E_\beta = 0$ the onsets of the transitions $|\,0\rangle \leftrightarrow |\,1\rangle\,, |\,2\rangle$ are supposed to happen at the same bias voltage, i.e. at $eV = -2E_1 = 2E_2$. The next onset is expected at the transition $|\,2\rangle \leftrightarrow |\,d\rangle$, i.e. at $eV = 2(E_1{+}U)$, and the last onset ($|\,1\rangle \leftrightarrow |\,d\rangle$) at $eV = 2(E_2{+}U)$. These values are marked with vertical lines in the figure and good agreement is found. In the Coulomb blockade regime where only the transitions $|\,0\rangle \leftrightarrow |\,1\rangle\,, |\,2\rangle$ are allowed, the value of the current agrees reasonably with the value I_1 from Eq. (6.7), while at $eV \to \infty$ the current indeed reaches the value I_2 of Eq. (6.8).

It has been shown that the 2vN method gives the onset of the current at the molecular levels of the DQD rather than at the single-particle levels. This is due to the fact that the method works in the eigenbasis of the dot Hamiltonian, thereby taking both the internal coherent oscillations and the Coulomb interaction fully into account. Furthermore, the results in both the Coulomb blockade regime and infinite-bias limit agree well with the results obtained by others.[3]

Furthermore, the current was calculated in the high-bias regime with all transitions well inside the bias window (not shown), and excellent agreement with Eq. (6.8) was found for all values of the interdot coupling Ω, showing that the 2vN method works even for the lead-dot couplings being much stronger than the interdot coupling.

6.2 Negative differential conductance in double-quantum dots

As discussed in Chap. 4 the levels in a quantum dot are electrostatically influenced by the coupling to the leads and the nearby gates. In Chap. 4 only a common back gate was used while in this chapter it is assumed that two gates are present, offering control over the individual levels. For a symmetric bias,

---

[2] Notice that Eq. (6.7) is not symmetric with respect to the interchange $\Gamma_L \leftrightarrow \Gamma_R$, as in the regime where double-occupation is forbidden the filling of the dot can happen in two different ways, $|\,0\rangle \to |\,1\rangle\,, |\,2\rangle$, which happens through the left contact, while when occupied the dot can only be emptied in one way, which is through the right contact.

[3] In Chap. 8 the importance of working in the many-particle (Fock) basis when treating nonlinear transport is further discussed.

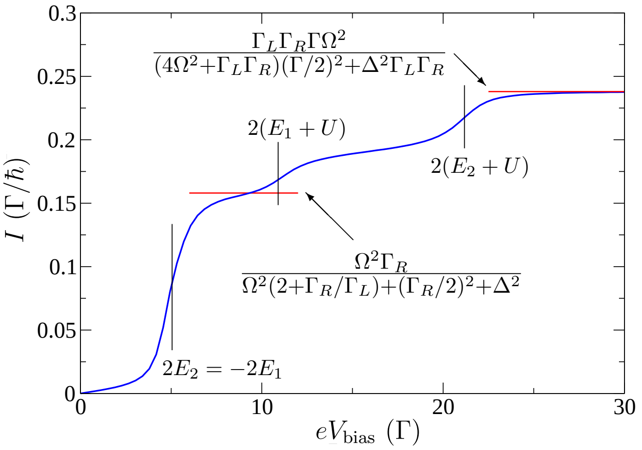

Figure 6.2: The current versus the bias voltage calculated with the 2vN approach for the parameters $\Gamma_L = \Gamma_R = \Gamma/2$, $\Omega = 5\Gamma/2$, $E_{\alpha,\beta} = \pm\Gamma/2$, $U = 8\Gamma$, $k_BT = 0.1\Gamma$ and $W = 30\Gamma$. The bias voltage is applied symmetrically.

the levels will then move according to

$$E_\alpha = E_\alpha^0 + \lambda_\alpha \frac{eV_{\mathrm{bias}}}{2} - \eta_\alpha e V_{\mathrm{gate}}^\alpha, \tag{6.9}$$

$$E_\beta = E_\beta^0 - \lambda_\beta \frac{eV_{\mathrm{bias}}}{2} - \eta_\beta e V_{\mathrm{gate}}^\beta. \tag{6.10}$$

Here E_i^0 are the equilibrium energy levels for $V_{\mathrm{bias}} = V_g = 0$, λ_α, λ_β are the lever arms due to the applied bias voltage for the respective dot levels, and η_α, η_β are the lever arms due to the gate voltages, see also Chap. 4. This allows for an independent control of V_{bias}, the level detuning $\Delta = E_\alpha - E_\beta$, and the average level position $\rho = E_\alpha + E_\beta$.

Assuming fixed gate voltage, the levels will slide across each other when sweeping the bias voltage and thereby change the detuning Δ. The maximum current is obtained when the levels are aligned, giving pronounced resonance features in the IV-curves.[4] The crossing of the levels gives rise to negative differential conductance and as it is caused by the electrostatic environment of the dot, it will be denoted *electrostatically induced NDC.* Below it is assumed that the influence of the bias voltage is exactly balanced by the gate voltages such that the detuning Δ is kept fixed, thereby removing the electrostatically induced NDC.

---

[4] For a discussion of the resonance features, see also Chap. 4.

Quantum mechanical effects might also lead to NDC in double quantum dots, which have been discussed by various authors: *i)* J. Aghassi *et al.* [67] studied the current and the shot noise in the limit where the interdot coupling is much stronger than the coupling to leads, $\Omega \gg \Gamma$. They found that NDC only occurs if the spacial symmetry of the structure is broken, either by detuning of the levels, $\Delta \neq 0$, or asymmetric barriers, $\Gamma_L \neq \Gamma_R$. *ii)* In the opposite limit, $\Omega \ll \Gamma$, I. Djuric *et al.* [68] showed that for aligned levels, $\Delta = 0$, NDC occur at the transitions $|\,1\rangle\,, |\,2\rangle \rightarrow |\,d\rangle$ for a certain ratio between the lead-dot coupling and the interdot tunneling coupling. As explained below, the NDC is caused by decoherence. Finally, *iii)* also in the weak interdot coupling limit, $\Omega \ll \Gamma$, and for $\Delta \gg \Omega$, B. Wunsch *et al.* [69] found that the current is asymmetric with respect to reversal of bias voltage, and that pronounced NDC occurs after the onset of the transitions $|\,0\rangle \rightarrow |\,1\rangle\,, |\,2\rangle$. They assign these effects to the level renormalization due to the coupling to leads.

In all three works the current is calculated to lowest order in the lead-dot coupling Γ, i.e. only in the sequential tunneling limit. For the works *ii)* and *iii)*, where they consider the weak inter-dot tunneling limit, it is not a priori obvious that this is justified as the sequential tunneling expression is derived under the assumption that the levels are only weakly coupled to the leads. Furthermore, they use the local basis, $|\,\alpha\rangle\,, |\,\beta\rangle$ and do not diagonalize the dot part of the Hamiltonian, which leads to simpler analytical expressions. The application of the local basis is reasonable in *iii)* where $k_B T \gg |E_1 - E_2|$, but not in *ii)*, where $\Delta = 0$.

Below the same parameter regimes as in *ii)* and *iii)* are considered using the 1vN and 2vN approaches from Chap 5.

6.3 Applying the 1vN and 2vN methods to the DQD problem

When applying the 1vN formalism two different versions are used. In Paper III App. A the general set of 1vN equations are shown, where the scattering rates are of the form (c_ℓ are constants depending on the explicit form of the couplings)

$$\begin{aligned}\sum_{k\ell} &\frac{T_{ba}(k\ell)T^*_{b'a'}(k\ell)f_\ell(E_k)}{E_k - E_{b'} + E_a - i0^+} \\ &\longrightarrow \sum_\ell c_\ell \left[\frac{i}{2}\Gamma_\ell(E_{b'} - E_a)f_\ell(E_{b'} - E_a) + \mathcal{P}\int \frac{dE}{2\pi}\frac{\Gamma_\ell(E)f_\ell(E)}{E - E_{b'} + E_a}\right]\end{aligned} \tag{6.11}$$

where the sum over $k\ell$ has been changed to an integral, see Sec. 5.6, and f_ℓ is the Fermi function evaluated using the chemical potential μ_ℓ. The imaginary part in Eq. (6.11) is the (in-) scattering rate. The real part causes a shift of the levels which is often neglected but plays a key role in the discussion below.

The 1vN calculations where the real parts are omitted are denoted “1vN-noR”. Otherwise the real parts are included and the calculations are denoted “1vN”.

Consider first NDC due to decoherence and assume fixed couplings to leads. At first sight it appears counter-intuitive that for small Ω the current is larger in the Coulomb blockade regime than when double occupation is allowed, $I_1 > I_2$. Qualitatively this can be explained as different broadening of the levels in the different regimes, see Paper III Sec. IVD, or alternatively as being due to the quantum Zeno effect, see Ref. [30] Sec. II. In the latter description, localized dot states, positive bias $\mu_L > \mu_R$ and all transitions well inside the bias window are assumed. The current flows through the system via a scattering process moving an electron from the left lead onto the left dot. Then the electron passes from the left to the right dot via a coherent evolution, i.e., the system is in a coherent superposition between the left and the right dot state and the off-diagonal elements of the reduced dot density matrix are non-vanishing. Now the leads can be viewed as observers destroying the coherent superposition between the dot states by adding/removing electrons to/from the system. In the Coulomb blockade regime only the right lead acts as an observer as double occupation is forbidden. When double occupation is allowed, both contacts act as observers thereby diminishing the current by destroying the superposition.[5] In the limit $\Omega \gg \Gamma_{L,R}$ the internal oscillations are much faster than the scattering rate due to the coupling to leads, and the current increases monotonously.

In Ref. [68] they apply a formalism developed by B. Dong *et al.* [70], where a set of generalized rate equations were derived by applying the nonequilibrium Green function formalism. At the plateaus with double occupation being either forbidden or allowed, they find expressions which agree exactly with the results in Eqs. (6.7)-(6.8), and they notice that for vanishing detuning, $\Delta = 0$, $I_1 > I_2$ if $\Omega < \sqrt{\Gamma_L \Gamma_R}/2$, such that NDC occurs at the transitions at $|\,1\rangle\,, |\,2\rangle \to |\,d\rangle$.

Several aspects are questionable. First of all, the applied generalized master equation formalism is derived in the local basis, i.e. the internal oscillations due to the interdot tunneling Ω are not treated exactly.[6] As a consequence, the transitions happen at the energies of the localized levels $E_{\alpha,\beta}$ and not at the eigenenergies $E_{1,2}$, which are the correct intrinsic energies of the dot. The applied approach is only reasonable when the smearing of the levels caused by the temperature is larger than the energy difference $|E_\alpha - E_\beta|$. Secondly,

---

[5] In Ref. [30] this is taken as an example of the importance of using a set of generalized master equations and not classical rate equations, where in the latter the off-diagonal elements are neglected.

[6] The same formalism was previously discussed in Ref. [71], where it was shown to fail for the spin-model treated in Chap. 7 due to non-hermicity of the derived density matrix.

the current is only calculated to lowest order in the coupling, whereby the broadenings of the transitions are only given by the temperature, not taking the quantum mechanical level broadening into account. Considering temperatures $k_BT < \Gamma$, they treat a regime where the sequential tunneling result is not valid. Finally, they do not consider the real parts of the scattering rates, which is important especially in the regime $\Omega < \Gamma_\ell$ as discussed below.

Figure 6.3 shows the results obtained using the 1vNnoR and 2vN approaches. For $\Omega = \sqrt{\Gamma_L\Gamma_R}/2 = \Gamma/10$ the 1vNnoR approach gives an IV-characteristic which does not show a single long plateau with the value $I_1 = I_2$, but shows some further structure at the onset of the different transitions. It is also noticed that the onset of the transition $|\,0\rangle \leftrightarrow |\,1\rangle\,, |\,2\rangle$ is seen in the 1vNnoR calculation, but is washed out in the 2vN calculation due to the level broadening. In Ref. [68] only a single step is seen, as they work in the local basis without diagonalizing the dot part of the Hamiltonian.

For $\Omega < \sqrt{\Gamma_L\Gamma_R}/2$ the 1vNnoR approach does indeed reach the value I_1 when double-occupation is forbidden. At the step where double occupation becomes possible NDC is observed, and the width of the step is due to the temperature and the two different values for the onset of the transitions $|\,2\rangle \to |\,d\rangle$ and $|\,1\rangle \to |\,d\rangle$. On the contrary, the 2vN approach does not reach the plateau value I_1, and the NDC is much weaker. This is due to the smearing of the level caused by the coupling to leads but also by the level renormalization not included in the 1vNnoR approach. In Paper III Fig. 4 calculations using the 1vN and 2vN approaches for larger values of the Coulomb interaction, U, show that even for $U \gg \Omega, \Gamma$ no plateau value I_1 is reached, emphasizing the importance of the real parts.[7]

In conclusion, it has been shown that the onsets of the transitions happen at the molecular levels found by diagonalizing the dot Hamiltonian, rather than at the energies of the localized levels. Furthermore, the NDC effect discussed in Ref. [68] is significantly diminished due to both level renormalization and broadening induced by the coupling to leads.

In the work by B. Wunsch *et al.* [69], NDC in double quantum dots due to level renomalization is considered. They also work in the local basis, which is justified as they in order to simplify the analysis and interpretation assume $|E_1 - E_2| \leq \Gamma \ll k_BT$, i.e. the smearing due to temperature is much larger than the level spacing between the states.[8] They use the Diagrammtic Real-time Transport Theory (see Sec. 5.2) in the sequential tunneling limit, where they keep the real parts of the scattering rates.

The main finding in this work is that for finite Coulomb interaction the level in each dot is dragged closer to the chemical potential of the nearest lead.

---

[7] Notice that the value I_1 in Eq. (6.7) where derived in the limit $U \to \infty$.

[8] The advantage of working in the local basis is that it is simpler to obtain analytic results.

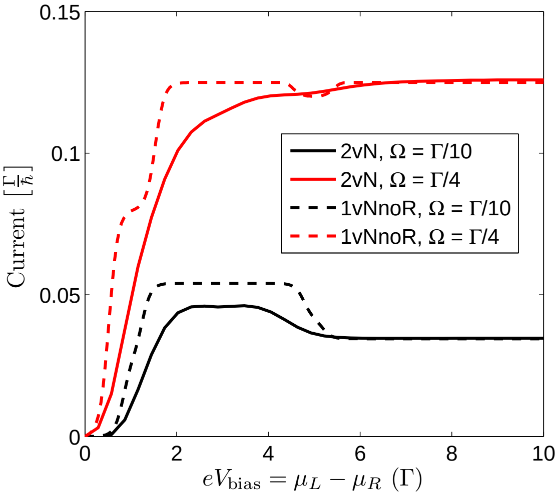

Figure 6.3: The current versus the bias voltage calculated using the 2vN and 1vNnoR approaches for two different values of Ω using the parameters $\Gamma_L = \Gamma_R = \Gamma/2$, $E_{\alpha,\beta} = \Gamma/2$, $U = 2\Gamma$, $k_BT = 0.05\Gamma$ and $W = 30\Gamma$.

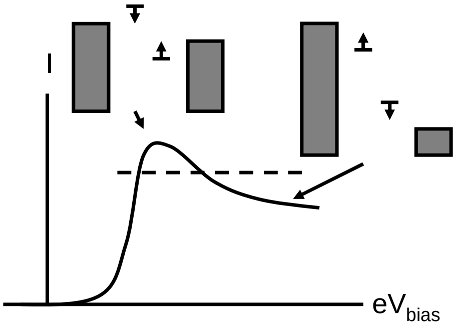

Figure 6.4: Sketch of the level renormalization described in Ref. [69] for large Coulomb interaction, see also Eq. (6.12). The arrows indicate how the levels move relative to the chemical potential of the nearest lead, and the dashed line indicates the plateau value of the current in case of no level renormalization. First the level renormalization gives a decrease of the detuning between the levels, causing an overshoot of the current as compared to the plateau value. This is followed by an increased detuning causing a significant negative differential conductance. See in particular Fig. 6.5d for $\Delta = \Gamma/4$.

The effect is largest when the level is close to the chemical potential of the lead and disappears when it is far away. For symmetric bias, $\mu_{L/R} = \pm eV/2$, they find the analytic expression for the level renormalization (see also Eq. (9) and Fig. 2 in Ref. [69]),[9]

$$\delta E_{\alpha/\beta} = \phi_{L/R}(\rho/2) - 2\phi_{L/R}(\rho/2 + U) + \phi_{L/R}(\rho/2 + U_{\text{intra}}) \tag{6.12}$$

with $\phi_\ell(E) = \frac{\Gamma_\ell}{2\pi}\text{Re}\Psi(\frac{1}{2} + \frac{i}{2\pi}\frac{E-\mu_\ell}{k_B T})$, and Ψ being the digamma function. The energy U_{intra} is the intradot Coulomb energy, which in their work serves as a high-energy cut-off, with U_{intra} being by far the largest energy. The level renormalization leads to an effective detuning of the levels, $\Delta_{\text{eff}} = E_\alpha + \delta E_\alpha - (E_\beta + \delta E_\beta)$. Being in a situation as sketched in Fig. 6.4 with a symmetrically applied bias, the detuning is first decreased, $\Delta_{\text{eff}} < \Delta$, giving a clear overshoot at the first plateau, and then increased, $\Delta_{\text{eff}} > \Delta$, leading to a significant NDC.

However, as they consider the weak internal coupling limit, $\Omega < \Gamma_{L,R}$, it is not clear that higher-order coupling effects will not alter this finding. Moreover, within their approximation scheme, the temperature and the tunnel coupling become independent energy scales.

Using the 1vN, 1vNnoR and 2vN methods the different parameter regimes were treated in Paper III. As an overview, consider Fig. 6.5a-c calculated using the 1vN approach using $\Omega < \sqrt{\Gamma_L\Gamma_R}/2$, $\Omega = \sqrt{\Gamma_L\Gamma_R}/2$ and $\Omega > \sqrt{\Gamma_L\Gamma_R}/2$, respectively. In Fig. 6.5a for $\Delta \simeq 0$ one clearly sees NDC due to decoherence at the transition $|1\rangle, |2\rangle \to |d\rangle$, occurring around $eV_{\text{bias}} \simeq 20\Gamma$. In Fig. 6.5b this effect has disappeared giving an almost constant current away from zero bias, and in Fig. 6.5c the current increases monotonically with the bias voltage for all values of the detuning Δ.

The level renormalization is visible as the bending of the resonance lines around the '$\Delta = 0$'-line in Fig. 6.5a-c. The effect is most pronounced in the weak interdot coupling limit ($\Omega < \sqrt{\Gamma_L\Gamma_R}/2$, a) and almost disappears in the opposite limit (c). If the level renormalization is neglected in the scattering rates, the resonance line will be straight (not shown). In Fig. 6.5d-f IV-curves corresponding to cuts along horizontal lines in the contour plots in Fig. 6.5a-c are shown, i.e. Δ is kept fixed. The calculations are done using the 1vN, 1vNnoR and the 2vN methods.

The calculations presented in Fig. 6.5 show that the level renormalization is pronounced for small interdot tunneling coupling leading to a significant NDC, which is not included if the real parts of the scattering rates are neglected. For increasing interdot coupling the effect disappears as the states become more delocalized over the structure, i.e. coupling the bonding and anti-bonding states more equally to both leads. For temperatures $k_B T = \Gamma$ only small

---

[9] In [69] they work within the approximation $|E_1 - E_2| \leq \Gamma \ll k_B T$ and consequently the energies $E_{1,2}$ are replaced by their common average value $\rho/2$.

deviations between the 1vN and the 2vN approaches are observed, but for $k_B T < \Gamma$ the 1vN method overestimates the level renormalization (see Paper III Fig. 3). Moreover, in the non-interacting limit, $U = 0$, the 1vN method overshoots at the transition $|\,0\rangle \rightarrow |\,1\rangle\,, |\,2\rangle$ and gives a weak but physically wrong NDC even for $k_B T = \Gamma$, as shown in Paper III Fig. 4. In this case it can be obtained from an exact nonequilibrium Green function calculation that no level renormalization occurs. It was verified numerically that for $U = 0$ the 2vN calculation yields exactly the nonequilibrium Green function result.

6.4 Discussion and conclusion

Two quantum mechanical sources of negative differential conductance in double quantum dots have been discussed. For the NDC due to decoherence occurring at weak interdot coupling, the importance of working in the diagonalized basis of the dot Hamiltonian was shown. This gave a weak NDC not only given by the temperature, as predicted by calculations performed in the local basis. For NDC due to level renormalization, a more complete picture was presented by considering all values of the ratio between the interdot coupling and the coupling to leads, and also discussing the temperature dependence. For temperatures comparable to the coupling to leads, good agreement between the 1vN approach including the real parts of the coupling constants and the 2vN approach was found. For lower temperatures, the first-order approach overestimates the level renormalization.

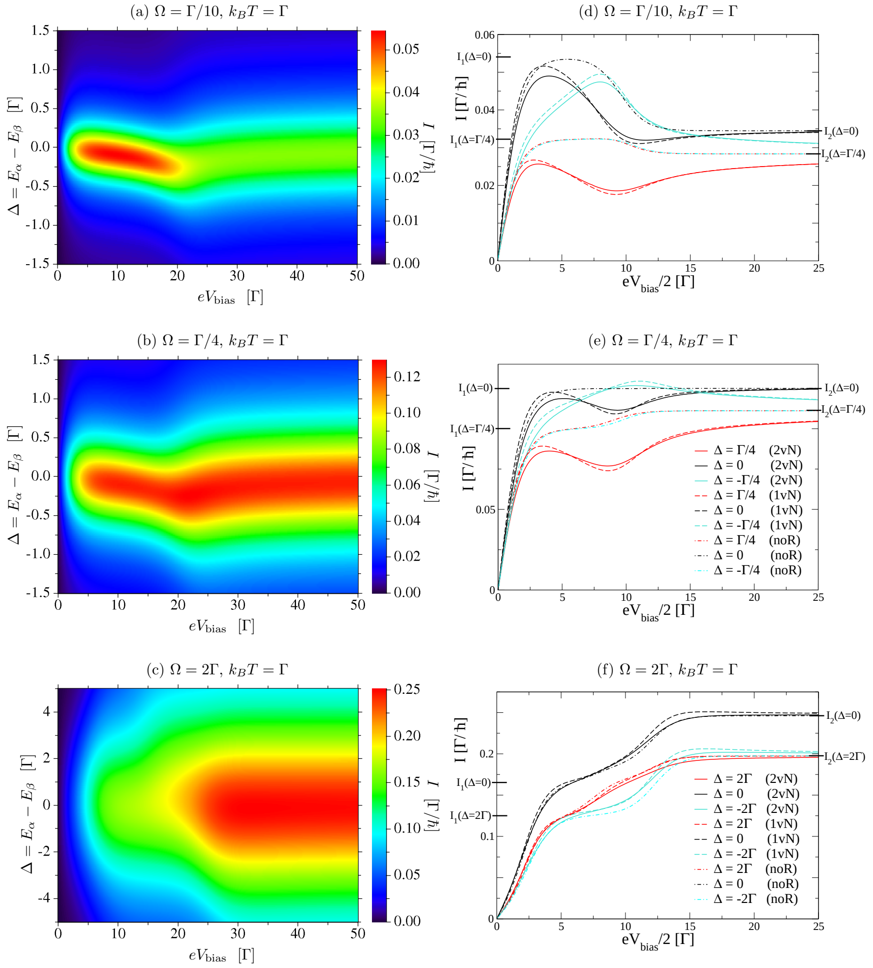

Figure 6.5: The contour plots a-c show the current versus the bias voltage and the detuning Δ using the 1vN approach for $\Omega/\Gamma = 0.1,\ 0.25$ and 2, respectively. The other parameters are $\Gamma_L = \Gamma_R = \Gamma/2$, $E_\alpha + E_\beta = 0$, $U = 10\Gamma$, $k_BT = \Gamma$ and $W = 35\Gamma$. The figures d-f are calculated using the 1vN, 1vNnoR and 2vN approaches and correspond to cuts along horizontal lines in Figs. a-c. The same values for the detuning Δ are used in Figs. d and e. From Paper III.

7

The FAB model

Many electronic devices are based on controlling the flow of electrons via their charge by altering the electrostatic environment, as, e.g., in transistors. However, it is also possible to take advantage of the spin of the electrons when designing electronic components, and the field of research is frequently named spintronics.

For several decades it has been possible to form layered structures of different materials using so-called epitaxial growth. Sandwiching an insulating layer between two ferromagnetic films, Julliere showed that the tunneling resistance of the device depends on whether the magnetizations of the ferromagnetic films are parallel or antiparallel [72], which is denoted the magnetoresistance. Later, two groups almost simultaneously discovered that structures consisting of layers with ferromagnetic/non-magnetic/ferromagnetic materials displayed a strong dependence on an applied in-plane magnetic field [73, 74, 75]. The effect was named giant magnetoresistance (GMR) and found almost immediately commercial use for read heads in modern hard drives and for magnetic sensors. For mesoscopic systems, spintronics has received an enormous attention, especially theoretically due to the proposal of the spin transistor by Datta and Das [76].

In the context of quantum dots, where the Coulomb interaction between the electrons plays a significant role, investigations of the possibilities for taking advantage of the electron spin are an active field of research. For isolated single or double quantum dots, the research deals with the manipulation of the spins using a combination of applied magnetic fields, electric gates and exploiting the local magnetic environment, see, e.g., [77]. The research is in particular driven by the perspectives for implementing devices for quantum computers in solid state materials [78]. In transport devices the possibility of using the spin has also been investigated, e.g., by attaching ferromagnetic contacts to various types of quantum dots [79, 80, 81], and one such device will be discussed in this chapter. It is described by a single-level Anderson model with ferromagnetic contacts, and in addition a magnetic field is applied noncollinearly with the magnetizations of the leads. The model is named the Ferromagnetic Anderson

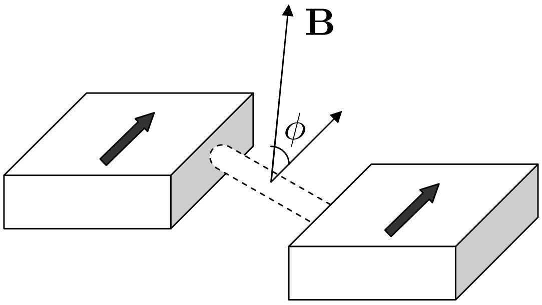

Figure 7.1: A sketch of the FAB model with two polarized leads and an applied magnetic field.

model with an applied magnetic B-field, in short FAB.[1] For the bare level at resonance, the model shows in the linear conductance regime a strong dependence on the angle between the magnetizations of the leads and the applied magnetic field, and the Coulomb interaction. This is explained as an interplay between interference and interaction, which makes the model a challenge and a benchmark for theoretical formalisms describing transport through quantum dots.

In this chapter, the 2vN transport formalism presented in Chap. 5 is applied to the FAB model in both the linear response regime and for finite bias. In the linear response regime the results are compared to density-matrix renormalization group (DMRG) calculations, while for finite bias the role of the non-diagonal elements of the density matrix and the failure of a mean-field solution are discussed. The material in this chapter is based on Paper IV.

7.1 The FAB Hamiltonian

Imagine a physical system consisting of a quantum dot coupled to ferromagnetic leads, such as, e.g., a carbon nanotube coupled to leads via ferromagnetic Ni contacts [81], where the magnetizations of the leads are assumed to be unaffected by the applied magnetic field, see Fig. 7.1. The validity of the latter assumption can be questioned, but it might be realized in magnetic thin-films where the magnetic moments are strongly pinned in the plane of the films. In this thesis, as well as in Paper IV, only parallel magnetizations of the leads are considered.

---

[1] This model was previously studied in Refs. [71, 82] and also in Ref. [83].

Based on this physical system, a model Hamiltonian with three parts is considered,

$$H = H_{LR} + H_T + H_D, \tag{7.1}$$

where

$$H_{LR} = \sum_{\alpha=L,R,k\sigma} \xi_{\alpha,k\sigma} c^{\dagger}_{\alpha,k\sigma} c_{\alpha,k\sigma}. \tag{7.2}$$

Here $\sigma = \uparrow / \downarrow$ is the spin of the electrons, α denotes the left or right electrodes, which are assumed to be polarized along the z-axis (the spin quantization axis), either parallel or anti-parallel. The quantum dot is subjected to a magnetic field $\mathbf{B}$, which is tilted by an angle ϕ with respect to the z-axis and lies within the xz-plane. Note that the negative sign of the electron charge is neglected for simplicity. Thus, the energetically preferred spin direction is pointing in the direction of $\mathbf{B}$. The dot-Hamiltonian reads ($n_\sigma = d^{\dagger}_{\sigma} d_\sigma$)

$$H_D = \sum_{\sigma} \xi_0 d^{\dagger}_{\sigma} d_\sigma + U n_\uparrow n_\downarrow - \sum_{\sigma\sigma'} \mu_B \mathbf{B} \cdot \boldsymbol{\tau}_{\sigma\sigma'} d^{\dagger}_{\sigma} d_{\sigma'}, \tag{7.3}$$

where ξ_0 is the orbital quantum dot energy, $B = |\mu_B \mathbf{B}|$ represents the magnetic field splitting, $\boldsymbol{\tau}$ is a vector containing the Pauli spin matrices, and U is the Coulomb energy for double occupancy. In a spin basis parallel to $\mathbf{B}$, the dot Hamiltonian is diagonalized as

$$H_D = \sum_{\sigma} (\xi_0 - \tilde{\sigma} B) d^{\dagger}_{\tilde{\sigma}} d_{\tilde{\sigma}} + U n_{\tilde{\uparrow}} n_{\tilde{\downarrow}}, \tag{7.4}$$

where the d_σ and $d_{\tilde{\sigma}}$ operators are related by the unitary rotation

$$d_\sigma = \sum_{\tilde{\sigma}} \mathbf{R}_{\sigma\tilde{\sigma}} d_{\tilde{\sigma}}, \quad \mathbf{R} = \begin{pmatrix} \cos(\phi/2) & \sin(\phi/2) \\ -\sin(\phi/2) & \cos(\phi/2) \end{pmatrix}. \tag{7.5}$$

Finally, the tunneling Hamiltonian is

$$H_T = \sum_{\alpha=L,R} \sum_{k\sigma} \left(t_{\alpha,k\sigma} c^{\dagger}_{\alpha,k\sigma} d_\sigma + \text{h.c.} \right) = \sum_{\alpha=L,R} \sum_{k\sigma\tilde{\sigma}} \left(t_{\alpha,k\sigma} \mathbf{R}_{\sigma\tilde{\sigma}} c^{\dagger}_{\alpha,k\sigma} d_{\tilde{\sigma}} + \text{h.c.} \right). \tag{7.6}$$

Here the tunneling matrix element $t_{\alpha,k\sigma}$ can be spin dependent, because the states in the leads depend on the spin direction.

The energy-dependent coupling constants are defined as

$$\Gamma_\alpha(\varepsilon) = 2\pi \sum_{k\sigma} |t_{\alpha,k\sigma}|^2 \delta(\varepsilon - \xi_{\alpha,k\sigma}) = \sum_{\sigma} \Gamma_{\alpha,\sigma}(\varepsilon), \tag{7.7}$$

and below P_α denote the polarization of the tunneling from lead α defined through $\Gamma_{\alpha,\sigma}(\varepsilon) = \frac{1}{2}\left(1 + \sigma P_\alpha\right) \Gamma_\alpha(\varepsilon)$. Notice that $P_\alpha \in [-1, 1]$ such that $P_\alpha =$

± 1 corresponds to full spin-↑ / ↓ polarization and $P_\alpha = 0$ corresponds to unpolarized leads. For parallel (antiparallel) polarization of the leads the P_α's have the same (opposite) sign. Finally, the total coupling constant is $\Gamma(\varepsilon) = \Gamma_L(\varepsilon) + \Gamma_R(\varepsilon)$ and $\Gamma^0 = \Gamma(0)$.

For the 2vN calculation, the many-body eigenstates of the system are needed, which are $\left\{ |\,0\rangle, \left|\,\tilde{\uparrow}\right\rangle, \left|\,\tilde{\downarrow}\right\rangle, |\,2\rangle \right\}$, where $|\,2\rangle = d^\dagger_{\tilde{\downarrow}} d^\dagger_{\tilde{\uparrow}} |0\rangle$, with the energies $0, E_{\tilde{\uparrow}} = \xi_0 - B, E_{\tilde{\downarrow}} = \xi_0 + B$ and $E_2 = E_{\tilde{\uparrow}} + E_{\tilde{\downarrow}} + U$, respectively.

In Ref. [82] it was shown that for fully polarized leads with parallel magnetizations, the bare level on resonance, $\xi_0 = 0$, and vanishing Coulomb repulsion, $U = 0$, the linear conductance versus the angle ϕ becomes (h is Planck's constant):

$$G^{\mathrm{non-int}} = \frac{e^2}{h} \frac{\Gamma^0_L \Gamma^0_R}{B^2} \frac{\cos^2\phi}{1 + \cos^2\phi \left[(\Gamma^0_L + \Gamma^0_R)/2B\right]^2}. \tag{7.8}$$

Qualitatively the result can be understood as in the basis where the dot Hamiltonian is diagonal the bare level is split into two levels at $\mp B$, each broadened by the coupling to leads depending on the angle ϕ as $\cos^2\phi/2$ and $\sin^2\phi/2$, respectively. This gives the spectral functions sketched in Fig. 7.2a. Electrons tunnel through the two resonances giving destructive interference at $\phi = \pi/2$, i.e., when the levels are equally wide. At $\phi = 0, \pi$ one of the levels is pinched off and transport is only through the opposite level, see Fig. 7.2a.

Under the same conditions as stated above, the linear conductance can be obtained in the cotunneling regime ($[\Gamma^0_L + \Gamma^0_R]/B \ll 1$) even in the presence of Coulomb interactions by applying the T-matrix formalism [82]:[2]

$$G^{\mathrm{cotun}} = \frac{e^2 \Gamma^0_L \Gamma^0_R}{h} \left[\frac{\cos^2(\phi/2)}{-B} + \frac{\sin^2(\phi/2)}{B+U} \right]^2. \tag{7.9}$$

In this regime, the conductance shows a cross-over from the behavior with anti-resonances at $\phi = \pi/2$ for the non-interacting case, to a spin-valve effect for $U \to \infty$ with $G^{\mathrm{cotun}} \propto \cos^4(\phi/2)$, i.e. the anti-resonance around $\phi = \pi/2$ disappears and the conductance vanishes instead for $\phi = \pi$, see Fig. 7.2b.

7.2 The linear response regime

In the linear response regime the FAB model shows, as pointed out above, some interesting features when the linear conductance is plotted versus the angle between the magnetizations of the leads, showing a strong dependence of the Coulomb interaction on the dot.

---

[2] Another application of the T-matrix formalism is shown in Chap. 8.

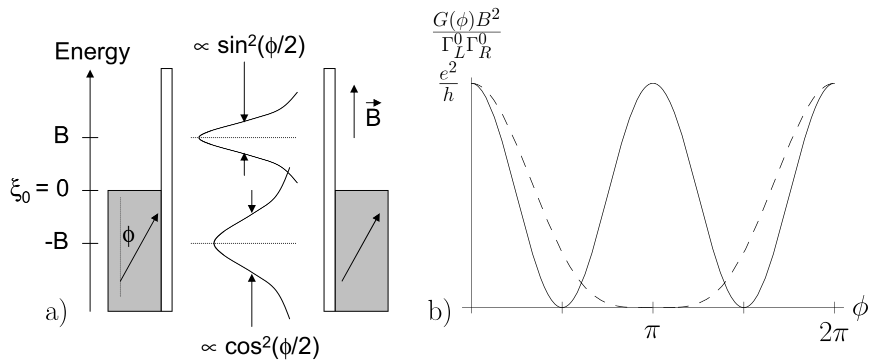

Figure 7.2: a) Schematic energy spectrum in the linear conductance regime for the non-interacting case. The bare resonant level is split due to the magnetic field. The widths of the two resonances depend on the angle ϕ as $\cos^2(\phi/2)$ and $\sin^2(\phi/2)$, respectively. b) The linear conductance, Eq. (7.9), showing the anti-resonances for noninteracting electrons (full line, $U = 0$) and the spin valve behavior for strongly interacting electrons (dashed line, $U = 100B$) as a function of the angle between the magnetizations of the dot and the applied magnetic field.

The analysis presented in Refs. [71, 82] is only valid in the regime with vanishing Coulomb interaction or in the cotunneling regime $B \gg \Gamma^0$. The goal of Paper IV is to also include the regime where the strength of the coupling to leads and the magnetic field strength are comparable, $B \sim \Gamma^0$, and also include arbitrary Coulomb interaction. This regime is considered to be complicated as broadening as well as Coulomb interactions have to be properly accounted for.[3]

Density-matrix renormalizations group calculations were carried out by D. Bohr and P. Schmitteckert giving numerically exact results used for benchmarking. The calculations are limited to the linear response regime, zero temperature and partial polarization, where the latter gives a smearing of the angular dependence discussed above. However, the physical picture remains unchanged. Furthermore, it was found in Paper IV that within a Hartree-Fock approximation the nonequilibrium Green function method leads to almost identical results even for large Coulomb repulsion, which is rather surprising as mean-field solutions are known to be problematic in the Coulomb blockade regime [84]. The success of the mean-field solution was explained in terms of the occupations of the dot levels in the diagonal basis for the situation sketched in Fig. 7.2a,

---

[3] Notice that the FAB Hamiltonian, and consequently all results are symmetric with respect to $\phi \rightarrow 2\pi - \phi$. It is therefore sufficient to show results for angles in the interval $\phi \in [0, \pi]$.

where one level is above and the other below the chemical potentials of the leads, see Paper IV. Below the focus is instead on results of the 2vN method for the linear response regime, which are not included in Paper IV.

For the T-matrix calculations, a constant coupling constant, Γ^0, is used below, while for the DMRG and the 2vN calculations an elliptic, energy-dependent coupling constant defined as $\Gamma(E) = \Gamma^0\sqrt{W^2 - E^2}/W$ with a bandwidth $W = 10\Gamma^0$ is used for the 2vN calculation and $W = 2\Gamma^0$ for the DMRG calculation. For the 2vN results the linear conductance is defined as $G = I/eV_{\text{bias}}$, with I being the current and $eV_{\text{bias}} = \mu_L - \mu_R$ a small applied bias voltage. For the bare level at resonance, $\xi_0 = 0$, the current versus the angle ϕ is calculated for $B = 2\Gamma^0$ for a symmetric bias, fixing the chemical potentials at $\mu_L = -\mu_R = 0.05\Gamma^0$ and the temperature at $k_BT = 0.05\Gamma^0$ such that $eV_{\text{bias}}, k_BT \ll B, \Gamma^0$.

The results are shown in Fig. 7.3. For the noninteracting case, $U = 0$, the nonequilibrium Green function result was calculated for comparison and an exact match with the 2vN approach was found (not shown). For $U \geq 0$ the 2vN results are compared to the T-matrix results, which is a generalization of Eq. (7.9) to arbitrary polarization (see App. A in Paper IV), and for $U/\Gamma^0 = 0, 0.5, 4, 6$ also with the DMRG results. For the latter very good agreement was found for all values of the Coulomb interaction despite the fact that the DMRG result is the true linear conductance calculated for zero temperature and a different energy-dependence of the coupling constants were used in the DMRG and the 2vN calculations.

Numerically the 2vN method is difficult to apply in the linear response regime and for low temperatures, where a fine energy-discretization of the leads is needed. Therefore results could not be obtained for many angles for U-values in the interval $U = 2\Gamma^0 - 4\Gamma^0$. For $B = \Gamma^0/2, \Gamma^0$ calculations were also done, but for a detailed comparison very low temperatures and small bias voltages are required, which are difficult to handle numerically. However, the calculations seem to indicate the correct behaviour also in this regime (not shown).

The T-matrix results for the linear conductance were derived for zero temperature, but energy-independent coupling constants were used. In Fig. 7.3 the deviation of the T-matrix result as compared to the other approaches might be due to the fact that the derivation of the T-matrix conductance assumes $B \gg \Gamma^0$, giving (almost) full occupation of the lower level which might not hold for $B = 2\Gamma^0$ [71, 82].

It is concluded that the 2vN method is indeed capable of handling both the influence of interactions and interference in the linear response regime, but numerically it is difficult to obtain results for all angles. The numerical problems for some angles are partly due to the fact that for these angles one of the levels is almost decoupled from the leads in case of highly polarized leads,

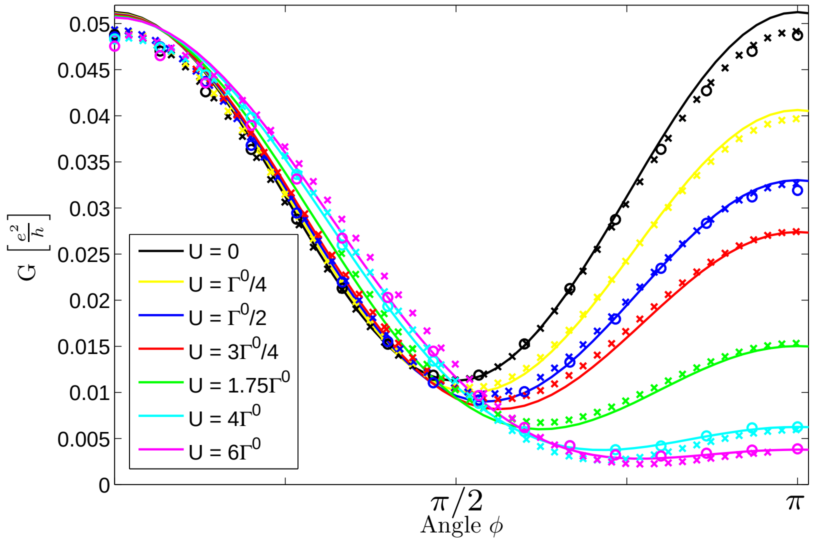

Figure 7.3: The T-matrix cotunneling results (full lines), DMRG results ('o') and 2vN results ('x') for the linear conductance versus the angle ϕ for the bare level at resonance, $\xi_0 = 0$. Notice that the DMRG results are only calculated for $U/\Gamma^0 = 0, 0.5, 4, 6$. It is the true zero-bias conductance for vanishing temperature which is calculated with the T-matrix and the DMRG methods. For the 2vN results the temperature is $k_B T = 0.05\Gamma^0$ and a small finite bias, $\mu_L = -\mu_R = 0.05\Gamma^0$ is used. The linear conductance is defined as $G = I/eV_{\text{bias}}$, where I is the current. The coupling constants are defined in the main text. The other parameters are: $B = 2\Gamma^0$, $\Gamma_L = \Gamma_R = \Gamma^0/2$ and $P_L = P_R = 0.8$. *The DMRG calculations were performed by D. Bohr and P. Schmitteckert.*

making it hard to obtain the correct occupations of the levels.

7.3 The finite bias regime

For finite bias two different setups are considered. In the first example, taken from Paper IV, the FAB model is solved using the 2vN method, and the results are compared with results obtained using the nonequilibrium Green function formalism within a mean-field approximation. It is found that the mean-field approximation is not able to capture the blockade regime.[4] Secondly, a setup related to FAB is considered, which was used by S. Datta [85] in order to

---

[4] The general discussion of mean-field approximations applied to transport through nanostructures is postponed to Chap. 8.

illustrate the importance of the correct treatment of Coulomb interaction, coherences and broadening in quantum transport.

In Paper IV, the FAB model with the bare level at resonance and the magnetic field $B = 2\Gamma^0$ is treated. For a symmetric bias, $\mu_L = -\mu_R = eV_{\text{bias}}/2$ the full IV-curve is calculated using the 2vN method and the nonequilibrium Green function method within a mean-field approximation, see Fig. 7.4a and Fig. 7.4b, respectively.[5] In the mean-field calculation, the interaction part of the Hamiltonian, $U\left[n_{\tilde{\uparrow}}\left\langle n_{\tilde{\downarrow}}\right\rangle + n_{\tilde{\downarrow}}\left\langle n_{\tilde{\uparrow}}\right\rangle\right]$, is replaced with

$$\begin{aligned} H_{\text{Hartree}} &= U\left[d^\dagger_{\tilde{\uparrow}}d_{\tilde{\uparrow}}\left\langle d^\dagger_{\tilde{\downarrow}}d_{\tilde{\downarrow}}\right\rangle + d^\dagger_{\tilde{\downarrow}}d_{\tilde{\downarrow}}\left\langle d^\dagger_{\tilde{\uparrow}}d_{\tilde{\uparrow}}\right\rangle\right], && (7.10) \\ H_{\text{Fock}} &= -U\left[d^\dagger_{\tilde{\uparrow}}d_{\tilde{\downarrow}}\left\langle d^\dagger_{\tilde{\downarrow}}d_{\tilde{\uparrow}}\right\rangle + d^\dagger_{\tilde{\downarrow}}d_{\tilde{\uparrow}}\left\langle d^\dagger_{\tilde{\uparrow}}d_{\tilde{\downarrow}}\right\rangle\right], && (7.11) \end{aligned}$$

denoting the Hartree and the Fock part of the interaction.[6]

As discussed in Chap. 6, shoulders in the current are expected whenever a single-particle excitation enters the bias window. For the parameters used in Fig. 7.4 this first happens at $eV_{\text{bias}} = 2|E_{\tilde{\uparrow},\tilde{\downarrow}}| = 4\Gamma^0$ when the transitions $|\,0\rangle \to \left|\,\tilde{\uparrow}\right\rangle, \left|\,\tilde{\downarrow}\right\rangle$ become possible. The next shoulder should appear for the transition $\left|\,\tilde{\downarrow}\right\rangle \to |\,2\rangle$ at the bias voltage $eV_{\text{bias}} = 2(E_{\tilde{\downarrow}} + U) = 12\Gamma^0$, and finally the last shoulder is expected at $eV_{\text{bias}} = 2(E_{\tilde{\uparrow}} + U) = 20\Gamma^0$ for the transition $\left|\,\tilde{\uparrow}\right\rangle \to |\,2\rangle$.

This behaviour is indeed observed in Fig. 7.4a. In Eq. (10) in Paper IV it is shown that for the angles $\phi = 0, \pi$, the couplings to the eigenstates are $\Gamma_{\alpha,\tilde{\uparrow}(\tilde{\downarrow})}(\varepsilon) = (1 \pm P)\Gamma_\alpha(\varepsilon)/2$, respectively, giving a strong(weak) coupling of the spin-$\tilde{\uparrow}(\tilde{\downarrow})$ state.

For $\phi = 0$, transport after the first shoulder is dominated by tunneling through the lower level with spin-$\tilde{\uparrow}$, while occupation of the other level tends to block the current due to Coulomb interaction. At the second shoulder, the current rises as transport becomes possible even if the spin-$\tilde{\downarrow}$ state is occupied.

For $\phi = \pi$ the strengths of the couplings are reversed and after the first shoulder, the current is mainly due to transport through the upper level with spin-$\tilde{\downarrow}$. The value of the current is slightly less than for $\phi = 0$ as the occupation of the blocking state (spin-$\tilde{\uparrow}$) is larger than for $\phi = 0$ due to the lower energy of the spin-$\tilde{\uparrow}$ state. After the second shoulder at $eV_{\text{bias}} = 12\Gamma^0$, the blocking spin-$\tilde{\uparrow}$ state can be filled in two different ways. Either by the process $|\,0\rangle \to \left|\,\tilde{\uparrow}\right\rangle$

---

[5] The details of the nonequilibrium Green function calculation is found in Paper IV.

[6] Often the Fock term is neglected, but for situations where spin is not conserved, e.g., due to tunneling to leads, this procedure gives a basis-dependent approximation and a non-vanishing Fock term.

or the process $|\,2\rangle \to \left|\,\tilde{\uparrow}\right\rangle$, leading to a larger blocking than at the first shoulder and consequently a lower value of the current. Between the first and the second shoulder negative differential conductance occurs.

The mean-field solution completely misses these blocking features as seen in Fig. 7.4b. Here the current increases monotonously for all angles and the second shoulder is not visible. The example illustrates the failure of mean-field solutions when blocking of states is essential. These issues are further discussed in Chap. 8.

In Ref. [85] S. Datta proposed a nonequilibrium Green function formalism formulated in a many-body Fock space, where the goal was to account properly for the Coulomb effects, the coherences and the broadening of the levels.[7] As a test of the method, he used a model system very similar to the FAB model described in the present chapter. Here the same type of calculations are done for the FAB model using the 2vN formalism.

Again the Hamiltonian in Eq. (7.1) is considered, but a different notation for the polarization is used, where the couplings are specified directly $\Gamma_{\alpha,\sigma}(E) = 2\pi\sum_{k\sigma}|t_{\alpha,k\sigma}|^2\delta(\varepsilon-\xi_{\alpha,k\sigma})$. Here σ is the spin of the lead states. A coupling constant $\Gamma(E)$ is defined, which takes the constant value Γ for $|E| \leq 0.95W$ and $\Gamma(E) = 0$ for $|E| > W$, while for $0.95W < |E| < W$ an elliptic interpolation as in Chap. 6 is used.

In Fig. 7.5 the results for different values of $E_\downarrow$ and $\Gamma_{R\uparrow}$ are shown, where the couplings $\Gamma_{\alpha\sigma}(E)$ for the individual spin and lead indices are defined as multiples of $\Gamma(E)$. Two different angles between the parallel magnetizations of the leads and the applied magnetic field are considered: $\phi = 0$ (full lines) and $\phi = \pi/2$ ('+'). As described above, a change in the current is expected whenever single-particle excitations enter the bias window. Consider first unpolarized leads and equal energies, $E_{\tilde{\uparrow}} = E_{\tilde{\downarrow}} = 50\Gamma$, corresponding to the black curve and black pluses in Fig. 7.5. A monotonous increase of the current is seen for both angles and the results are identical. This is indeed the correct behaviour as the two different angles only correspond to a change of basis. For $\phi = 0$ the dot basis is identical to the lead spin basis, and for $\phi = \pi/2$ the dot spins are superpositions of the leads spins. The description of the transport is however very different, as for $\phi = 0$ the off-diagonal elements of the density-matrix vanishes as spin is conserved, whereas for $\phi = \pi/2$ the magnitudes of the off-diagonal elements are comparable to the diagonal ones. Neglecting the off-diagonal elements would lead to a basis dependent IV-characteristic, which emphasizes the importance of the off-diagonal elements in quantum transport.

Also for identical level energies, $E_{\tilde{\uparrow}} = E_{\tilde{\downarrow}} = 50\Gamma$, and $\phi = 0$ but with polarized leads, the current shows a decrease after $eV_{\text{bias}} = 50\Gamma$ due to a blocking of

---

[7] Here coherence is used in the sense of nonvanishing off-diagonal elements of the density matrix.

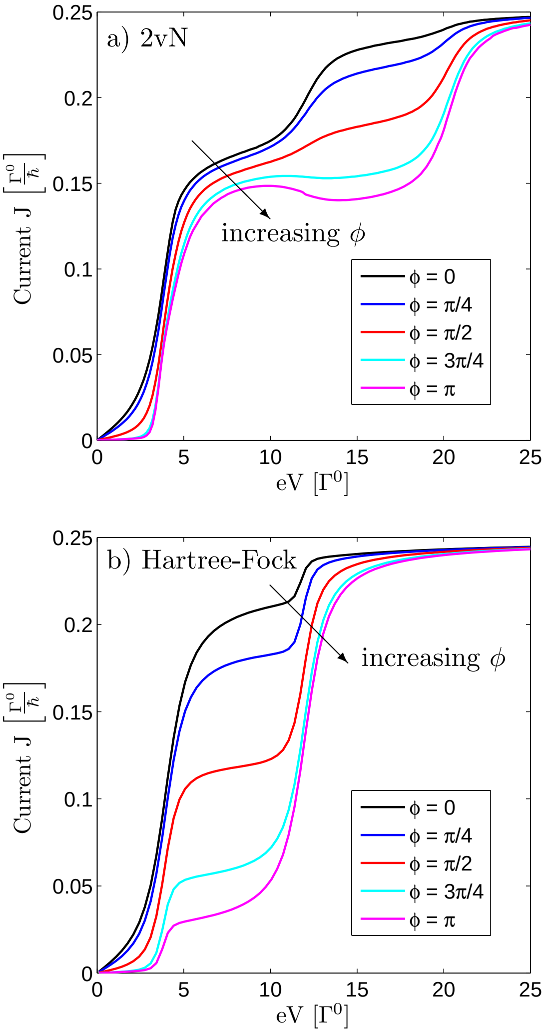

Figure 7.4: The current versus bias voltage for five different angles ϕ obtained using the 2vN density-matrix formalism (a) and the mean-field Hartree-Fock approach (b). The parameters are: $\xi_0 = 0$, $B = 2\Gamma^0$, $U = 8\Gamma^0$ and $k_BT = 0.1\Gamma^0$, $P_L = P_R = 0.8$ and the bias is applied symmetrically. For the 2vN-method a constant density-of states with a half band-width $W = 20\Gamma^0$ and a 5% cut-off at the ends is used (see the main text), while for the Hartree-Fock calculation the wide-band limit is assumed, i.e. the real-part of the self-energy was neglected. From Paper IV.

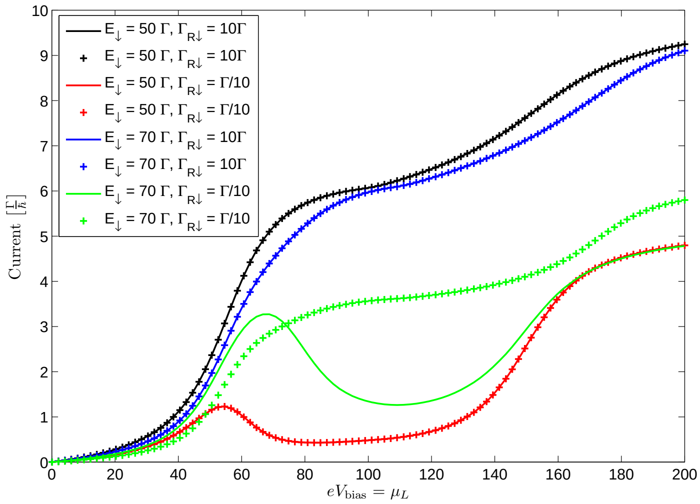

Figure 7.5: The current versus bias voltage for the angle $\phi = 0$ (full lines) and $\phi = \pi/2$ ('+'). The right chemical potential is kept at zero, i.e. the bias voltage corresponds to $eV_{\text{bias}} = \mu_L$. The fixed parameters are: $\Gamma_{L\uparrow} = \Gamma_{R\uparrow} = \Gamma_{L\downarrow} = 10\Gamma$, $k_BT = 2.5\Gamma$, $U = 100\Gamma$, $E_\uparrow = 50\Gamma$, and the bandwidth $W = 250\Gamma$.

the current by the spin-$\tilde{\downarrow}$ state (red curve). As the two states with spin-$\tilde{\uparrow}, \tilde{\downarrow}$ are degenerate, the same IV-curve should be obtained for $\phi = \pi/2$ (red pluses), as it just corresponds to a rotation of the dot basis. This is indeed observed.

For spin-split levels $E_{\tilde{\uparrow}} = 50\Gamma$ and $E_{\tilde{\downarrow}} = 70\Gamma$, the curves for unpolarized leads are again identical for the two different angles, as the different angles only correspond to a change of the dot spin basis (the blue curve and blue pluses in Fig. 7.5). However, for spin-polarized leads *and* spin-split dot levels the situation is different for the two angles, as the dot levels are no longer degenerate. For $\phi = 0$ (green curve) spin-blockade occurs when the spin-$\tilde{\downarrow}$ level gets occupied around $eV_{\text{bias}} = 70$, whereas for $\phi = \pi/2$ (green pluses) the spin-blockade is lifted as the dot spins are superpositions of the lead spins.

Finally, it should be noticed that the broadening at the onsets of the shoulders are comparable to the coupling to leads rather than the energy scale set by the temperature.

7.4 Discussion and conclusion

In this chapter the transport properties of the Ferromagnetic Anderson model with an applied magnetic B-field (FAB) were discussed.

In the linear response it was shown that for sufficiently low temperatures and small bias voltages, the linear conductance calculated using the 2vN method was almost identical to density-matrix renormalization group calculations in the cotunneling regime. An approximate analytic result could in this regime be obtained using the T-matrix formalism. It was also discussed that the 2vN approach is not well suited for the linear response regime at low temperatures when one of the states is weakly coupled, as it requires a fine energy discretization of the leads, and it is difficult to obtain the stationary occupations.

In Paper IV, the success of the mean-field nonequilibrium Green function solution in the linear response regime is further discussed. It is also shown that the frequently used Hubbard-I approximation for the nonequilibrium Green function completely fails, even mathematically, for the FAB model due to the noncollinear leads and the spin-split levels.

The calculations for finite bias using the 2vN method illustrate the importance of off-diagonal elements in quantum transport and show for the FAB-model the basis-independence of the 2vN formalism. Furthermore, the 2vN method is capable of treating Coulomb blockade, which is not correctly described by a mean-field approximation. The latter issue is further discussed in the coming chapter.

8

Inelastic cotunneling in single quantum dots

Much work on quantum dots have focused on the sequential tunneling limit, where electrons pass through the structure whenever single-electron transitions are within the bias window, as discussed for the double quantum dot in Chap. 4. For a single quantum dot, the current plotted versus bias and gate voltage shows clear Coulomb blockade diamonds where the sides of the diamond mark the onset of sequential tunneling [8]. For enhanced couplings to leads higher-order processes may cause additional features within the Coulomb diamond as seen in experiments and shown schematically Fig. 8.1, and for a 2vN calculation in Fig. 8.2. These higher-order processes are so-called cotunneling events, where, e.g., two electrons tunnel almost simultaneously, thereby overcoming the Coulomb blockade [86]. This is possible due to the uncertainty principle, and is further discussed below.

Focusing on zero gate voltage in the schematic drawing in Fig. 8.1, i.e., the middle of the diamond, at low-bias the current has a finite value even deep inside the Coulomb blockade regime. This is due to elastic cotunneling processes, where electron tunnels through the structure via a virtual state, as sketched in Fig. 8.1. The energy of the dot is unchanged by the elastic cotunneling processes. For a further increase of the bias voltage a vertical ridge appears in case of non-degenerate states, defining the onset of inelastic cotunneling. Also in these processes transport is due to virtual states, but the final energy of the quantum dot may change, hence the term *inelastic*. The energy is provided by the leads. The onset of inelastic cotunneling occurs when the bias voltage matches the energy between the ground and the excited state.[1]

Experimentally inelastic cotunneling has been studied in various types of

---

[1] Also in the strong-coupling regime and for low temperatures, a zero-bias anomaly can occur inside Coulomb diamonds with an odd occupation number. This is the so-called Kondo effect (for a popular review, see [22]). In the discussion below, it is assumed that the temperature is so high that the Kondo effect plays no role.

quantum dots, e.g., gate-defined dots in two-dimensional electron gases [87, 88], gate defined ring-like structures with dots embedded in the arms [89, 90], single-molecules [91], carbon nanotube quantum dots [92, 93] and quantum dots in InAs-InP nanowires [15].

Besides from raising some fundamental questions about phase coherence of inelastic processes and decoherence due to interactions [89, 90], inelastic cotunneling can also be used as a spectroscopic tool for probing the spectrum of excited states. The advantage of inelastic cotunneling is that in an IV-curve the width of the onset of inelastic cotunneling is less broadened than the onset of sequential tunneling, thereby offering increased resolution [94].[2] This has been exploited in measurements of, e.g., the Zeeman splitting using inelastic spin-flip cotunneling [94], or the singlet-triplet splitting involving both the spin and the orbital degrees of freedom [87, 88].[3]

As it takes place in the Coulomb blockade regime, inelastic cotunneling is interesting from a theoretical point of view because it combines strong interactions with tunneling processes beyond sequential tunneling, and several aspects have been addressed. For few electron quantum dots with discrete energy levels, the studies include, e.g., the current, the thermopower [97], the noise properties [50], level-renormalization [92], three-terminal devices [98] and the width of the onset of inelastic cotunneling [99].

In this chapter the model Hamiltonian is first presented and some examples of how to calculate the scattering rates are discussed, see Sec. 8.1. In the finite-bias regime where inelastic cotunneling is present, mean-field methods fail which is discussed in Sec. 8.2, and the findings are compared to results obtained using the 1vN and 2vN approaches presented in Chap. 5. The broadening at the onset of inelastic cotunneling is treated in Sec. 8.3. Finally, in Sec. 8.4 some limitations of the 2vN method which can be probed in the elastic cotunneling regime are discussed. Also the failure of the order-by-order expansion in the inelastic cotunneling regime is considered. The conclusion on the findings is found in Sec. 8.5. The contents of this chapter have so far not been published elsewhere.

8.1 The Hamiltonian and some simple scattering rate calculations

In this section the Hamiltonian for the system is presented but before considering the results obtained using the 1vN and 2vN approaches in Sec. 8.2, it

---

[2] The width of the onset is further discussed in Sec. 8.3.

[3] Inelastic electron transport spectroscopy (IETS) has also been used in STM-measurements of, e.g., the vibrational spectrum of single molecules [95], and the Zeeman splitting in a single Mn-atom on a surface [96].

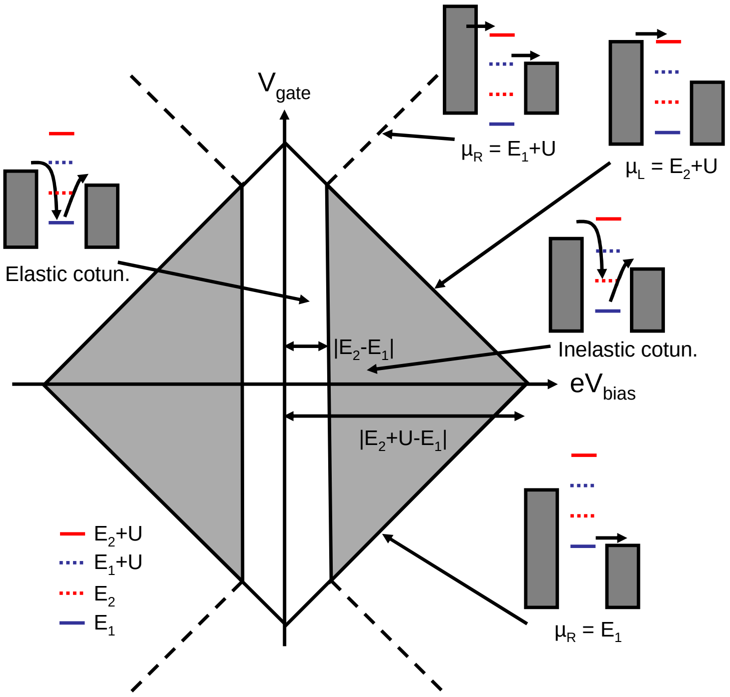

Figure 8.1: The stability diagram for the two-level model discussed in the text. The edges of the diamond are due to the onset of sequential tunneling where a chemical potential of the dot aligns with a chemical potential in one of the leads. The vertical lines inside the diamond mark the onset of inelastic cotunneling, while the dashed lines outside the diamond marks the onset of tunneling through excited states.

is discussed how to obtain the pure second-order scattering rates which give a better physical picture of the involved processes than the 2vN approach provide.

To simplify the discussion, a model with only two spinless levels is considered such that the Hamiltonian reads

$$H = \sum_{k,\ell=L,R} E_{k\ell} c^\dagger_{k\ell} c_{k\ell} + \sum_{k\ell n} \Big[V_{k\ell n} c^\dagger_{k\ell} d_n + \text{h.c} \Big] + \sum_n E_n d^\dagger_n d_n + U d^\dagger_1 d_1 d^\dagger_2 d_2, \tag{8.1}$$

with $n = 1, 2$ denoting the two dot states. The first term is the Hamiltonian of the leads, and the last two terms are the two single-particle states of the dot and the interaction between them. The second term is the tunnel Hamiltonian with the tunneling amplitudes $V_{k\ell n}$. Below it is assumed that $V_{k\ell n} = x_{\ell n} t_k$,

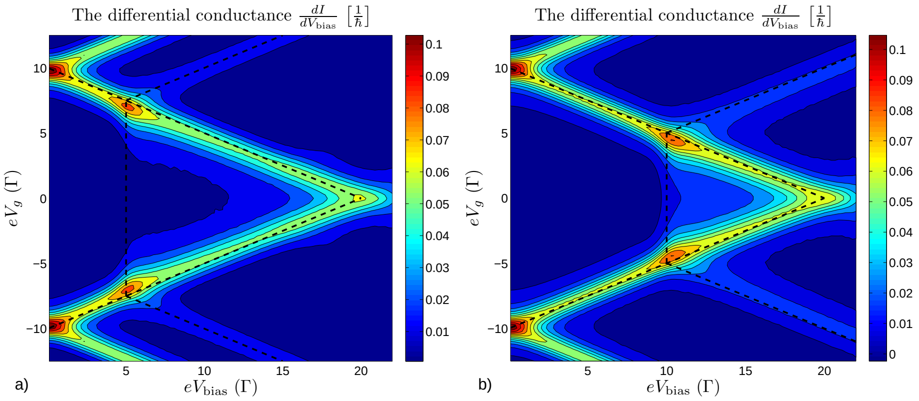

Figure 8.2: The differential conductance versus bias voltage and gate voltage, where the bias voltage is applied symmetrically, $\mu_L = \mu_R = eV_{\text{bias}}/2$. The levels in the dot are assumed to have the gate dependence $E_n = E_n^0 - eV_g$ with $e = |e|$ and $n = 1, 2$. The four coupling amplitudes are $x_{L1} = -x_{L2} = x_{R1} = x_{R2} = 1/\sqrt{2}$, i.e. $\Gamma_{\ell n} = \Gamma/2$, the temperature is $k_B T = \Gamma/4$ and $W = 25\Gamma$. The dashed lines mark the expected onsets of sequential tunneling (the boundaries of the diamond), the onset of inelastic cotunneling (the vertical lines), and the tunneling through excited states (the lines outside the diamond), see also Fig. 8.1. a) $E_1^0 = -10\Gamma$, $E_2^0 = -5\Gamma$ and $U = 15\Gamma$. b) $E_1^0 = -10\Gamma$, $E_2^0 = 0$, and $U = 10\Gamma$.

i.e. the coupling between both dot states and the lead states have a fixed phase factor $x_{\ell n}$,[4] and t_k is assumed to be a real number. The coupling constants are defined as $\Gamma_{\ell n}(E) = 2\pi \sum_k |V_{k\ell n}|^2 \delta(E - E_{k\ell n}) = |x_{\ell n}|^2 \Gamma(E)$. For the 2vN calculations a constant value Γ for $|E| \leq 0.95W$ is used, and it is assumed that $\Gamma(E) = 0$ for $|E| > W$. For $0.95W < |E| < W$ an elliptic interpolation is applied.

---

[4] This is important when considering, e.g., the Aharanov-Bohm effect which depends on the phase difference between different transport paths. If there is no fixed phase relation between the lead and the dot states, the transport paths will add up incoherently and no Aharanov-Bohm oscillations are visible. Experimentally a fixed phase relation is obtained by using a ring-like structure as a wave guide to couple the leads and the quantum dots, where only a few modes in the wave guide are accessible, see, e.g., [89, 90, 100, 101].

Cotunneling scattering rates

Using the Hamiltonian above, the system can be in the four different many-particle states denoted $|\,0\rangle$, $|\,1\rangle$, $|\,2\rangle$, $|\,d\rangle = d_2^\dagger d_1^\dagger\,|\,0\rangle$, with energies 0, E_1, E_2, E_d, respectively. It is assumed that $E_2 \geq E_1$. The different states and the leading order tunneling processes between them is shown in Fig. 8.3 for a situation with the state $|\,1\rangle$ being the ground state.

Using the so-called T-matrix approach, the tunneling rates can be calculated beyond sequential tunneling [102]. Here the second-order rates are calculated for the two-level model described above.[5] Of the second-order processes only the rates describing transport processes where an electron is transferred *through* the system via a virtual process are considered, while the number of electrons on the dot is left unchanged. For the system considered here, the dot state is either identical before and after the process (*elastic* cotunneling), or the state is changed ($|\,1\rangle \to |\,2\rangle$ or vice versa). For $E_1 < E_2$, the latter corresponds to an *inelastic* cotunneling process.

For the cotunneling rates the notation γ_{mn}^{RL} is used for a process where the dot is initially in the state $|\,n\rangle$ and ends up in the state $|\,m\rangle$, while an electron has been transferred from the left to the right contact. In total there are twelve processes: γ_{00}, γ_{11}, γ_{22}, γ_{dd}, γ_{12}, γ_{21} with LR and RL. Processes where no electrons are transferred through the quantum dot are neglected although they might give a level renormalization of the dot energies. In this semi-phenomenological approach such processes are neglected, and below only the rates γ_{11} and γ_{21} are discussed.

The second-order scattering rates are calculated as follows [102]:
Assume that initially the dot is in state $|\,n\rangle$ and the leads are in a state $|\,\nu_L\nu_R\rangle$, i.e. the initial state is $|\,i\rangle = |\,\nu_L\nu_R n\rangle$ with energy $E_i = E_{\nu_L\nu_R} + E_n$. The probability for the leads to be in the state $\nu_L\nu_R$ is denoted $W_{\nu_L\nu_R} = W_{\nu_L}W_{\nu_R}$, as the leads are assumed uncorrelated. In the final state an electron $k'L$ has been transferred from left to right ending up in the state kR, and the dot state has changed from $|\,n\rangle$ to $|\,m\rangle$, i.e. the final state is $|\,f_{kk'}\rangle = c_{kR}^\dagger d_m^\dagger c_{k'L} d_n\,|\,i\rangle$ with energy $E_i - E_n - E_{k'L} + E_m + E_{kR}$. According to the T-matrix formalism the second-order scattering rates are [102]

$$\gamma_{mn}^{RL} = 2\pi \sum_{kk'} \sum_{\nu_L\nu_R} W_{\nu_L\nu_R} \left| \langle f_{kk'}\,|\, H_T \frac{1}{E_i - H_0} H_T \,|\, i\rangle \right|^2 \delta(E_{f_{kk'}} - E_i) \tag{8.2}$$

The matrix elements can now be calculated for various initial states. As an example, the rate γ_{11}^{RL} describing the coherent sum of the elastic processes $|\,1\rangle \to |\,0\rangle \to |\,1\rangle$ and $|\,1\rangle \to |\,d\rangle \to |\,1\rangle$ transferring electrons from the left to

---

[5] For critical comments about the T-matrix procedure, see [37].

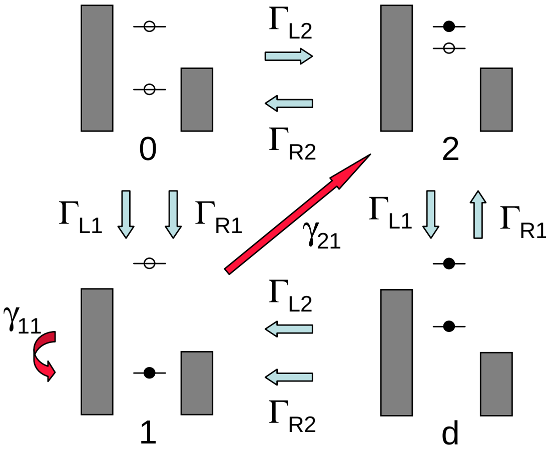

Figure 8.3: The model with two single-particle states and the four many-particle state $|\,0\rangle\,, |\,1\rangle\,, |\,2\rangle\,, |\,d\rangle$, with $|\,1\rangle$ being the ground state. The energy of the excited state $|\,2\rangle$ is in this sketch assumed to be higher than the right chemical potential. The other situation is shown in Fig. 8.5, and discussed in Sec. 8.3. The arrows show the leading order transport processes linking the different states, where the blue arrows mark the sequential tunneling processes and the red show the cotunneling processes. For the cotunneling processes transport is due to almost simultaneous tunneling of two electrons thereby overcoming the Coulomb blockade, as explained in the main text.

right lead is (for details, see App. C)

$$\gamma_{11}^{RL} = \frac{\Gamma^2}{2\pi}\int dE\left|\frac{x_{L1}^{*}x_{R1}}{E_1 - E} + \frac{x_{R2}x_{L2}^{*}}{E_2 + U - E}\right|^2 n_F(E-\mu_L)[1-n_F(E-\mu_R)], \quad (8.3)$$

and the rate γ_{21}^{RL} describing the sum of the inelastic processes $|\,1\rangle \to |\,0\rangle \to |\,2\rangle$ and $|\,1\rangle \to |\,d\rangle \to |\,2\rangle$ is

$$\begin{aligned}\gamma_{21}^{RL} = \frac{\Gamma^2}{2\pi}\int dE&\left|\frac{x_{R1}x_{L2}^{*}}{E_1 - E} - \frac{x_{R1}x_{L2}^{*}}{E_2 + U - E}\right|^2 \\ &n_F(E+E_2-E_1-\mu_L)[1-n_F(E-\mu_R)],\end{aligned} \quad (8.4)$$

where $n_F(E) = [1 + e^{E/k_BT}]^{-1}$ is the Fermi function, and energy-independent coupling constants are assumed (the Wide-Band Limit).

Two observations can be made: For vanishing temperature, $k_BT = 0$, the inelastic cotunneling rate γ_{21}^{RL} is only finite above the bias-threshold $eV_{\text{bias}} > E_2 - E_1$, giving direct access to the excitation energy of the quantum dot from the IV-curve. Secondly, for finite temperatures the expressions for the cotunneling rates diverge and a regularization procedure is needed. Turek *et al.* suggested adding $+i\Gamma$ by hand in the denominators and neglecting the part proportional to $1/\Gamma$, which correspond to an on-shell contribution, i.e. the sequential tunneling result [97]. The remainder is the cotunneling rate. This procedure was used, e.g., in Refs. [98, 103, 104], giving analytic expressions for the cotunneling rates in terms of polygamma functions.

In certain situations, the cotunneling rates exceed the values of the sequential tunneling rates. One example is shown in Fig. 8.3, with $|1\rangle$ being the ground state where $E_1 < \mu_{L,R}$ and $E_2 + U > \mu_L, \mu_R$. Here sequential tunneling is blocked and transport occurs via elastic sequential processes due to the cotunneling rates γ_{11} or via the inelastic cotunneling processes through γ_{21}.

Below the 2vN approach is applied over the full bias-range. As the method contains processes beyond second-order in the tunneling coupling, level renormalization as well as broadening of the level is included, and no regularization procedure is needed. The second-order expressions derived above are used to explain the findings in the cotunneling regime.

8.2 Mean-field vs. Generalized Master Equations

When treating quantum transport through nanodevices such as, e.g., molecules, molecular wires, Au or Pt contacts, an often used tool is density-functional theory (DFT) [105], which is often embedded in a nonequilibrium Green function framework [106]. DFT allows for the inclusion of the chemical structures of the devices, and these methods are frequently denoted *ab-initio* methods and are widely used in the field of molecular electronics.

Density-functional theory provides (in principle) exact results for the ground state properties of the systems but is effectively a mean-field method out of equilibrium, giving significant problems in the Coulomb blockade regime. Within the DFT framework attempts to overcome some of these problems have been proposed [107, 108], as well as the extension to Time-Dependent Density-Function Theory (TDDFT). In TDDFT the transport problem is transformed into a time-dependent one-particle scheme in a formally exact way. Here the major problem consists in finding sufficiently accurate action functionals for exchange and correlation effects [109].

Mean-field methods are essentially single-particle theories, where the effects of many-particle interactions are included via self-consistent calculations of averages between single-particle operators. Another approach is to work in the (many-particle) Fock-space as proposed for semiconducting quantum dots by

C.W.J. Beenakker [110] and used, e.g., in Refs. [111, 112]. In the Fock-space formulation interactions on the dot are treated exactly. Another example is the Diagrammatic Real-time Transport Theory discussed in Chap. 5. In the context of molecular electronics, the problems of self-consistent methods have been put forward by Datta and collaborators, e.g., pointing out the incorrect step heights in IV-curves as compared to Fock-space master equations [113, 114, 115].

Also for simplified model systems, mean-field methods have been applied. For a double quantum dot, bistability in the IV-curve leading to hysteresis was observed in Ref. [116], but these findings were questioned in Ref. [117] based on a master equation approach. For the Anderson model with a single spin-degenerate level, Horváth *et al.* also found that the mean-field solution incorrectly predicts a bistability for certain parameters [84].

The current versus bias voltage has been calculated for the two-level model introduced in Sec. 8.1 using the 1vN and 2vN methods as well as nonequilibrium Green functions within a mean-field approximation. In the latter, the interaction part of the Hamiltonian $Ud_1^\dagger d_1 d_2^\dagger d_2$ is replaced with the mean-field interaction

$$\begin{aligned} Ud_1^\dagger d_1 d_2^\dagger d_2 \to U\Big\{ & \left[d_1^\dagger d_1 \left\langle d_2^\dagger d_2\right\rangle + d_2^\dagger d_2 \left\langle d_1^\dagger d_1\right\rangle\right] \\ & - \left[d_1^\dagger d_2 \left\langle d_2^\dagger d_1\right\rangle + d_2^\dagger d_1 \left\langle d_1^\dagger d_2\right\rangle\right] \Big\}, \end{aligned} \tag{8.5}$$

where the first [...]-bracket is the Hartree term and the second the Fock term, similarly to Eqs. (7.10)-(7.11). This gives the effective single-particle levels $E_{1(2)} + U\left\langle d_{2(1)}^\dagger d_{2(1)}\right\rangle$, where the (generalized) occupations $\langle d_n^\dagger \mathrm{d}_m\rangle$ $(n, m = 1, 2)$ have to be found self-consistently. The calculation is identical to the one for the FAB model discussed in Chap. 7 and Paper IV.

Results for the two-level model

In Fig. 8.4 results for the two-level model defined in Eq. (8.1) are presented. The lower level is below the equilibrium chemical potentials, $E_1 < 0$, for two different values of E_1 and the other level is placed above, $E_2 > 0$. The chemical potential of the right contact is fixed while the left chemical potential is raised, $\mu_L = eV_{\text{bias}}$.

For low bias voltages, the system is in the Coulomb blockade regime and the 1vN method shows almost vanishing current for $\mu_L < E_2 + U$, whereafter it abruptly rises to its final value. Virtually no difference is observed between the curves for $E_1 = -4\Gamma$ and $E_1 = -2\Gamma$, respectively. The 2vN method gives, on the contrary, a finite current even in the Coulomb blockade regime. For $0 \le \mu_L \le |E_2 - E_1|$ only elastic cotunneling processes contribute to the current,

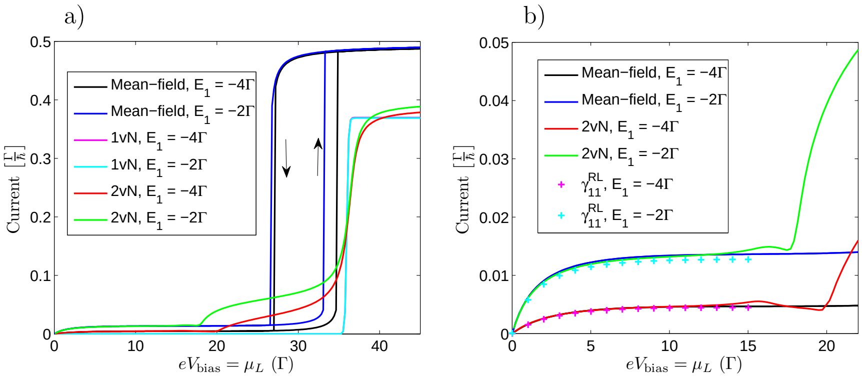

Figure 8.4: a) The current versus bias voltage for two different values of E_1 calculated using mean-field nonequilibrium Green functions, 1vN and 2vN. The chemical potentials are $\mu_L = eV_{\text{bias}}$ and $\mu_R = 0$. The phase factors are all equal $x_{\ell n} = 1/\sqrt{2}$, i.e. $\Gamma_{\ell n} = \Gamma/2$. The other parameters are: $E_2 = 16\Gamma$, $U = 20\Gamma$, $k_BT = \Gamma/10$ and $W = 50\Gamma$. The arrows indicate the direction of the bias voltage sweeps in the mean-field calculations. Note that the two 1vN results fall almost on top of each other. b) The low-bias regime for the same parameters as in a), but with the 1vN results replaced by the scattering expression $I^{\text{el.cotun}} = \frac{1}{\hbar}(\gamma^{RL}_{11} - \gamma^{LR}_{11})$ calculated for $k_BT = 0$.

and this is denoted the elastic cotunneling regime. The current agrees very well with $I^{\text{el. cotun}} = \frac{1}{\hbar}(\gamma^{RL}_{11} - \gamma^{LR}_{11})$ calculated for $k_BT = 0$ using Eq. (8.3), where it is noticed that at zero temperature the rate γ^{LR}_{11} vanishes. This approximation for the current is valid when the state $|1\rangle$ is almost fully occupied.[6] The onset of inelastic cotunneling is expected for $\mu_L = |E_2 - E_1|$ [see Eq. (8.4)] which is indeed seen for both values of E_1. A careful inspection shows a small dip in the current after the value $\mu_L = E_2$, see Fig. 8.4b. One can speculate that this is due to a small thermal occupation of this level. In the inelastic cotunneling regime, $|E_2 - E_1| \leq \mu_L \leq E_2 + U$, the current is a sum of elastic and inelastic cotunneling processes plus additional so-called cotunneling assisted sequential tunneling processes, which is further discussed in the next section. Finally, at $\mu_L = E_2 + U$ (the high-bias regime) the current rises to the final value which slightly overshoots the 1vN result, as the latter does not take the elastic cotunneling processes through the lower level into account. This is particularly pronounced for $E_1 = -2\Gamma$.

The mean-field nonequilibrium Green function results in Fig. 8.4 show a completely different behaviour. In the elastic cotunneling regime, the results

---

[6] The T-matrix approach was used in a similar setup for the FAB-model discussed in Chap. 7 and in Ref. [82].

agree with the 2vN and $I^{\text{el. cotun}}$ results, but the onset of inelastic cotunneling is missing. Instead a sudden switching of the current occurs before the onset of sequential tunneling at $\mu_L = E_2 + U$, and the final value of the current is significantly larger than the 2vN result. Sweeping the current in the opposite direction leads to a clear bistability where the current shows a sudden drop at a smaller bias voltage than the onset. The bistability can be understood in terms of the occupation of the lower level. In the elastic cotunneling regime and for increasing bias voltage, the lower level is almost fully occupied and the upper level almost completely empty. In the inelastic cotunneling regime the lower level starts to get emptied and the upper level starts to get occupied, thereby raising the lower level to the new position $E_1 + U \left\langle d_2^\dagger d_2 \right\rangle$. The lower level is eventually placed above the right chemical potential $\mu_L = 0$, allowing for sequential tunneling through the level. This leads to a too high plateau value in the high-bias regime. Sweeping the current backwards leads to the opposite scenario.

It is concluded that the mean-field approximation is not able to produce the correct IV-characteristic in the inelastic cotunneling regime where excited states get populated. In the high-bias regime it overestimates the current as compared to the generalized master equation results. Both the elastic cotunneling regime, the onset of inelastic cotunneling, as well as the high-bias limit are captured by the 2vN approach.

8.3 Broadening at the onset of inelastic cotunneling

Consider a discrete level coupled to a continuum of states. In Chap. 6 it was discussed how the coupling gives a renormalization of the level. In addition, if the system is initially prepared in the discrete state it will decay to the continuum, as the discrete state is not an eigenstate of the system due to the coupling [64]. To second order in the tunneling amplitude, the decay in time can be written as an exponential such that the occupation of the state is $\propto \exp(-\Gamma t)$, with Γ denoting the inverse of the characteristic lifetime. By Fourier transformation this corresponds in frequency space to a broadening of the discrete level, where Γ is the linewidth.

In a tunneling experiment, the linewidths of the levels give a broadening of the onsets of the current plateaus. As mentioned above, the onset of the inelastic cotunneling processes is expected to be less broadened than the onset of sequential tunneling. In the present section work on this topic is reviewed and calculations using the 2vN approach are presented. I gratefully acknowledge Matthias H. Hettler for suggesting this work.

Consider first the onset of sequential tunneling at zero temperature. The zero-temperature broadening of the onset of sequential tunneling is often denoted the intrinsic linewidth [118] or the lifetime broadening [87]. For a single non-interacting level, the intrinsic linewidth is $\Gamma_L + \Gamma_R$, which can be obtained, e.g., from a nonequilibrium Green function calculation [35]. In an IV-curve, the onset of sequential is therefore broadened by the same amount, most easily obtained from the differential conductance, dI/dV_{bias}. For the spin-degenerate, single-level Anderson model with strong Coulomb repulsion, the width of the onset of sequential tunneling depends on the asymmetry of the barriers as shown experimentally and theoretically by Könemann *et al.* [58].[7]

For finite temperatures, the total broadening is due to both the intrinsic linewidth and the temperature broadening, where the latter stems from the finite temperature of the leads. For vanishing intrinsic linewidth, the temperature broadening is proportional to k_BT and is in general dominant at high temperatures, $k_BT \gg \Gamma_L, \Gamma_R$. This is clearly seen experimentally as, e.g., in Fig. 2 in Ref. [119].

Below the onset of inelastic cotunneling is discussed for the two-level model presented in Sec. 8.1, and it is assumed that $\mu_L > \mu_R = 0$ and $E_1 < E_2$. At the onset, which happens at $eV_{\text{bias}} = |E_1 - E_2|$, two scenarios are possible: *i)* the excited state $|\,2\rangle$ is below both chemical potentials, $E_2 < \mu_L, \mu_R$, or *ii)* the state $|\,2\rangle$ is above the right chemical potential, $\mu_R < E_2 < \mu_L$, see Fig. 8.5. For situation *i)* the system can after an inelastic process end up in the state $|\,2\rangle$. In this case, either elastic cotunneling processes $|\,2\rangle \to |\,0\rangle \to |\,2\rangle$ occur, or the system enters the ground state via the inelastic cotunneling process $|\,2\rangle \to |\,0\rangle \to |\,1\rangle$. As no sequential processes are possible, the intrinsic linewidth of the state $|\,2\rangle$ is expected to be much smaller than $\Gamma_L + \Gamma_R$ and rather given in terms of the cotunneling rates γ_{22} and γ_{12}. For the other case, *ii)*, several transport paths are available if the system ends up in the excited state $|\,2\rangle$. A sequence of sequential tunneling processes $|\,2\rangle \to |\,0\rangle \to |\,2\rangle$ are possible and eventually the system enters the ground state via $|\,2\rangle \to |\,0\rangle \to |\,1\rangle$. Theses processes are named cotunneling assisted sequential tunneling (CAST), and were discussed theoretically in, e.g., Refs. [48, 99, 120], and both experimentally and theoretically in Ref. [47].[8] As the excited state $|\,2\rangle$ can decay by sequential tunneling to the right contact, the intrinsic width of the onset is anticipated to be proportional to Γ_R [87].

As for the sequential tunneling case there is also a temperature dependent

---

[7] In that work the theoretical calculations are performed using the Diagrammatic Real-time Transport Theory within the Resonant Tunneling Approximation, see Sec. 5.5.

[8] Within the Coulomb diamond, the CAST processes give a gate-dependent angular shape before the sequential lines but after the onset of inelastic cotunneling, which is seen in the conductance plot in Fig. 8.2a.

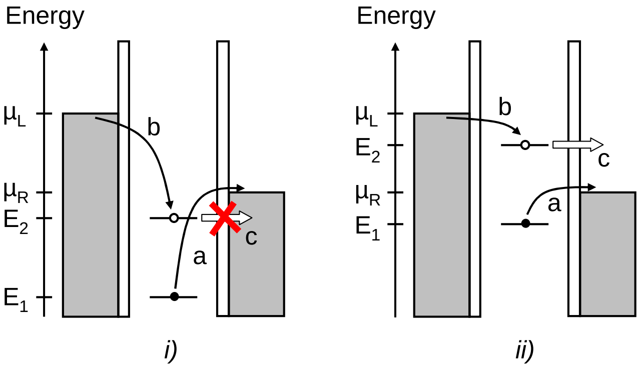

Figure 8.5: The two different situations after the onset of inelastic cotunneling discussed in the main text. The onset happens when the bias voltage matches the excitation energy, $\mu_L - \mu_R = |E_2 - E_1|$, whereafter an inelastic cotunneling process is possible. This is shown as a-b in the figures. With the excited state being occupied, there are two possibilities: In *i)* the current is blocked as the energy level E_2 is below the chemical potential of both contacts. The excited state can only decay via another inelastic process. In *ii)* the energy level E_2 is above the chemical potential of the right contact and an additional sequential tunneling process is possible.

contribution to the onset of inelastic cotunneling. For a vanishing intrinsic linewidth, the broadening at the onset of inelastic cotunneling is $5.44k_BT$ as shown in Ref. [118], where also an analytic expression for the shape of the onset is presented. However, this expression was derived for vibrational modes in a tunneling barrier where the tunnel matrix elements are independent of the level energies, which is not the case for cotunneling through quantum dots, see, e.g., the second-order matrix element in Eq. (8.2).

To our knowledge only a few transport experiments on quantum dots investigating the width of the onset of inelastic cotunneling have been carried out. One example is by Franceschi *et al.* [87] for a gate-defined quantum dot in a two-dimensional electron gas. Here they report finding a width depending on whether CAST processes are possible or not. However, no systematic investigation of the temperature dependence of the linewidth is performed.

In a recent work, Aghassi *et al.* investigated theoretically the onset of inelastic cotunneling using the Diagrammatic Real-time Transport Theory for the spin-split single-level Anderson model [99]. They calculated the tunneling rates to second-order in the coupling constant, Γ, and found that for both situations *i)* and *ii)* outlined above, the width of the onset is proportional to the temperature and no intrinsic linewidth is observed. However, as only tunneling processes to second order in the coupling constant are included, they are limited to the regime $k_BT > \Gamma$ and can only conclude that the observed linewidth for situation *ii)* is much smaller than Γ_R. Moreover, they use an order-by-order expansion to second-order in the tunneling coupling [see Eq. (5.10)], i.e. elastic and inelastic cotunneling processes are just included but all higher-order processes are neglected. Therefore the intrinsic linewidth at the onset of inelastic cotunneling might not be captured.

In Chap. 5 it was pointed out that for non-interacting systems where no inelastic cotunneling can occur, the 2vN approach gives the exact broadening at the onset of sequential tunneling, showing that the method in this situation includes all relevant higher-order processes. Therefore it was investigated if the method could also give some numerical insight into the intrinsic linewidth at the onset of inelastic cotunneling for the two-level model discussed in the present chapter. To reduce the computational effort, infinite Coulomb repulsion is assumed, $U \to \infty$, by removing the state $|d\rangle$ from the Hilbert space. The bias is applied by only raising the chemical potential of the left contact, $\mu_L = eV_{\text{bias}}$, and keeping $\mu_R = 0$. When taking the second-derivative of the current, d^2I/dV_{bias}^2, a peak appears at the onset of inelastic cotunneling. The width at the onset of inelastic cotunneling is defined as the full-width at half-maximum (FWHM) of this peak in accordance with Refs. [87, 99, 118].

The results are shown in Fig. 8.6, where the upper panels show the differential conductance, dI/dV_{bias}, while the lower panels show the FWHM of the peak in the second-derivative of the current at the onset of inelastic cotunneling. In the latter, the lines are $FWHM = 5.44k_BT$, corresponding to pure temperature broadening. Figures 8.5a-b and Figs. 8.5c-d correspond to the situations *i)* and *ii)* in Fig. 8.5, respectively, and for both cases the onset of inelastic cotunneling is found at $eV_{\text{bias}} = E_2 - E_1$ as expected. Compare also the shape of the differential conductance around the onset with Fig. 4.3.

Numerically it was difficult to obtain the second-derivatives and consequently to find the values for the FWHM, in particular for elevated temperatures. Therefore the values for the FWHM should be taken as approximate. However, it can be concluded that for both situations the results show only broadening due to temperature with a linewidth approximately given by $5.44k_BT$ in agreement with Ref. [118], and no intrinsic linewidth is observed. Therefore the findings suggest that for both situations the intrinsic linewidth is smaller than $\sim 5\%$ of Γ. This contradicts the conclusion in Ref. [87] based on experimental findings, but where no temperature dependence of the width was shown.

In conclusion, the calculations have shown that even when CAST processes are available, the 2vN approach shows no intrinsic linewidth. However, it remains an open question whether the linewidth is actually less than a few percent of Γ, or if the transport processes contributing to the width is not included in the 2vN approach and even higher-order tunneling processes must be taken into account.

8.4 Shortcomings of the 2vN approach and the order-by-order expansion

During the work with the spinless two-level model, a shortcoming of the 2vN method was found. It is related to the implicit summation of higher-order processes when applying the equation of motion technique.

Consider the elastic cotunneling regime, $eV_{\text{bias}} < |E_1 - E_2|$, in a situation with the state $|1\rangle$ being the ground state as shown in Fig. 8.3. Assuming $|E_1|, E_2 + U \gg \Gamma, eV_{\text{bias}}$ the factor $|\ldots|^2$ in Eq. (8.3) is approximated by a constant and taken outside the integral, and the current is evaluated as $I^{\text{el. cotun}} = \frac{1}{\hbar}\left(\gamma_{11}^{RL} - \gamma_{11}^{LR}\right)$. Evaluating the resulting integral over the product of the Fermi functions, the conductance in the linear response regime becomes[9]

$$G^{\text{el. cotun}} = \frac{e^2\Gamma^2}{2\pi\hbar}\left|\frac{x_{L1}^* x_{R1}}{E_1} + \frac{x_{R2}^* x_{L2}}{E_2 + U}\right|^2 . \tag{8.6}$$

For identical phase factors, e.g., $x_{\ell n} = 1$, the linear conductance vanishes at the particle-hole symmetric point, $E_1 = -(E_2 + U)$, i.e. both the first- and the second-order contributions to the conductance vanishes. For nonzero temperatures and a (small) finite bias, second-order contributions are finite but higher-order processes may still dominate.

The current in the low-bias regime was calculated using the 2vN approach setting all phase factors equal, and an unphysical negative current was found at the particle-hole symmetric point (not shown). This shows that when tunneling processes beyond second order in the tunnneling coupling are dominant, the 2vN method may fail as only a subset of processes beyond second order is included and not automatically the dominant ones.

Finally, the problem of the order-by-order expansion of the generalized master equation discussed in Sec. 5.2 is revisited, see Eq. (5.10). As explained below, the order-by-order expansion gets problems for the two-level model in the regime where cotunneling processes dominate when only processes up to second-order in the coupling constant are taken into account.

For simplicity the spin-split single-level Anderson model is considered, where no off-diagonal elements are present due to spin conservation, and also infinite Coulomb repulsion is assumed. Consider now a situation with the state

---

[9] See also [71, 82].

$|1\rangle = |\uparrow\rangle$ being the ground state and the state $|2\rangle = |\downarrow\rangle$ being the excited state. In the order-by-order expansion, the tunneling rates and the densities are expanded in powers of the tunneling coupling as shown in Eq. (5.10). As pointed out by Weymann *el al.* [49] and discussed in Refs. [48, 121], a problem occurs when the excited state is below both chemical potentials, corresponding to situation *i)* in Sec. 8.3. Expanding the occupations in powers of Γ, the occupation of the excited state, $P_2 = P_2^{(0)} + P_2^{(1)} + \ldots$, vanishes to zeroth order in Γ as sequential tunneling is exponentially suppressed due to the Coulomb energy, i.e. $P_2^{(0)} = 0$. However, for a sufficiently large bias voltage, the excited state can get populated via an inelastic cotunneling process from the ground state, $\gamma_{21} P_1^{(0)}$, which is second order in Γ. The problem now occurs because to second order in Γ the system cannot decay, as the decay can only happen via another inelastic process, $\gamma_{12} P_2^{(1)}$, which is third order in Γ. The consequence is a pumping of the excited state. As pointed out in Ref. [121] this may happen whenever all lowest order couplings to some state are suppressed.[10]

Different cross-over scheme have been proposed to handle this shortcoming of the order-by-order expansion [48, 49, 121], but the prize to pay is that the final result is no longer only second-order in the tunneling coupling but contains a subset of higher-order processes.

8.5 Discussion and conclusion

In this chapter it has been shown that the nonequilibrium Green function method with a Hartree-Fock mean-field interaction provides both quantitatively and qualitatively wrong results for the spinless two-level model in the inelastic cotunneling regime as well as in the high-bias regime. This is in line with findings in other theoretical work, e.g. Refs. [113, 84]. In the elastic cotunneling regime, the nonequilibrium Green function, the 2vN and the T-matrix solutions gave almost identical results. The 2vN method gave also the onset of inelastic cotunneling at the expected bias voltage, which matches the excitation energy.

Regarding the broadening of the onset of inelastic cotunneling, the results are inconclusive but so far no intrinsic linewidth has been observed for any of the two cases mentioned above. Hopefully further investigations will show whether this is because the 2vN method is unable to capture the intrinsic linewidth, or because the linewidth is much smaller than expected.

Finally, a shortcoming of the 2vN method in the elastic cotunneling regime at the particle-hole symmetric point was discussed, which was due to vanishing first- and second-order couplings. For similar reasons, the second-order expansion of a generalized master equation can also get problems due to a pumping of the upper level.

---

[10] For the 2vN approach no such pumping of the upper level has been observed.

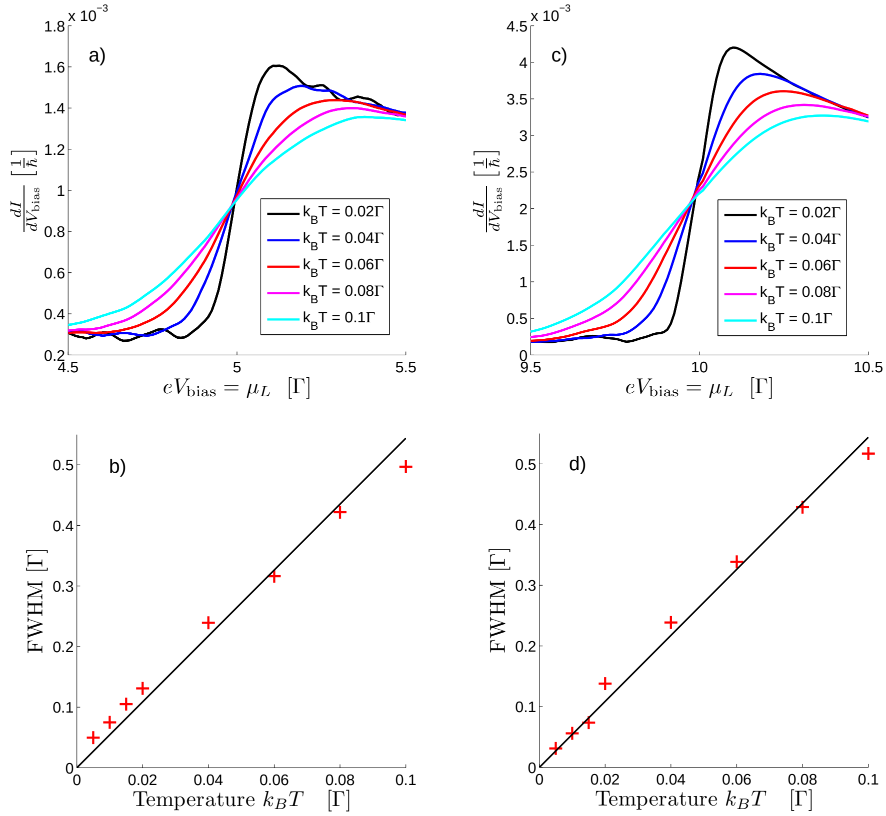

Figure 8.6: The derivative of the current, dI/dV_{bias}, and the full-width-half-maximum (FWHM) of the peak in the second- derivative, d^2I/dV_{bias}^2, at the onset of inelastic cotunneling for infinite Coulomb repulsion, $U \to \infty$. The bias is applied by raising $\mu_L = eV_{\text{bias}}$. Figure a-b are for $E_1 = -8\Gamma$ and $E_2 = -3\Gamma$, corresponding to situation *i)* in Fig. 8.5, while c-d are calculated for $E_1 = -5\Gamma$ and $E_2 = 5\Gamma$, i.e. situation *ii)* in Fig. 8.5. The full lines in Fig. b and d are the FWHM $= 5.44k_BT$. The other parameters are in all plots $x_{L1} = -x_{L2} = x_{R1} = x_{R2} = 1/\sqrt{2}$, and $W = 20\Gamma$.

9

Summary and outlook

In this thesis the topic of transport through nanostructures has been addressed. After a general introduction to the subject, a thorough analysis of transport spectroscopy data obtained from a double dot in an InAs-InP nanowire was presented in Chap. 4. Based on a capacitance model, it was explained how the various lines in the data could be related to the capacitances. Due to the lack of gate control for the individual dots, two relations between the capacitances were missing. From an electrostatic model for the nanowire, it was justified that also lead-next-to-nearest-dot capacitances should be included for a double dot embedded in a heterostructure nanowire. These capacitances are normally neglected in double dot systems with gate-defined dots [17].

In Chap. 5 an overview of the problem of calculating electron transport through nanostructures was presented with a particular focus on density-matrix based approaches, also denoted generalized master equations. The advantage of the density-matrix approach when formulated in a many-particle basis is that all interactions within the nanostructure are taken fully into account. Then a newly developed method, the 2vN approach, was presented. Formulated in a many-particle basis, it extends previous work on generalized master equations by not only treating the (generalized) occupations, but also including processes with up to two electron-hole pairs by applying a straightforward approximation scheme. Thus processes beyond sequential tunneling are included, such as, e.g., cotunneling processes, where electrons tunnel via virtual states. The method is not limited to the linear response regime, but is applicable over the full bias range. Steps in the current are not only broadened due to the temperature of the leads, but they also acquire a finite broadening because of the coupling to leads. The method is applicable for temperatures lower than the energy scale set by the coupling to leads, but cannot account for strong correlations close to zero temperature, as causing, e.g., the Kondo effect.

The method was applied to a double dot system in Chap. 6, where particular focus was given to the quantum mechanical level renormalization due to the coupling to leads, which can lead to negative differential conductance. The findings were compared to a first-order generalized master equation approach and good agreement was found for temperatures larger than the energy scale set by the coupling to leads. The work also emphasized the importance of working in the molecular basis, i.e. using the basis where the Hamiltonian of the central region is diagonal, in order to correctly describe the onset of the different steps in the current.

A spintronics model with a single level coupled to ferromagnetic leads with parallel magnetizations was discussed in Chap. 7, where a magnetic field was applied noncollinearly with the magnetization of the leads. With one level above the chemical potentials of the leads and the other below, the linear conductance shows a strong dependence on the angle between the magnetizations of the leads and the applied magnetic field, where the behaviour depends on the strength of the Coulomb interaction. The results obtained using the 2vN approach were compared to calculations performed by others using a density-matrix renormalization group scheme, as well as a scattering approach. For finite bias, the IV-curve also depended strongly on the angle between the magnetizations of the leads and the applied magnetic field, leading to negative differential conductance in some parameter regimes. It was also shown that the non-equilibrium Green function method with a mean-field approximation for the interaction was not even capable of describing this feature qualitatively. Finally, an example showing the importance of a correct treatment of the off-diagonal density matrix elements was included.

As a last application of the 2vN method, the phenomenon denoted inelastic cotunneling was addressed in Chap. 8. This is maybe the most prominent example, as it illustrates the need for a method which can correctly describe the Coulomb interaction between the electrons and also handle both sequential and cotunneling processes at temperatures lower than the energy scale set by the coupling to leads. It was shown that this is not the case for the mean-field approximation as it leads to a bistable solution due to an insufficient description of the Coulomb interaction. However, it also revealed that in certain situations the 2vN approach can yield physically incorrect results as further discussed below.

As the 2vN method, forming the core of this thesis, is a new way of including broadening of many-particle states within a density matrix formalism, the work presented in this thesis raises some fundamental and practical questions, and provides various opportunities for further research.

As mentioned in the final remarks in Chap. 5, it is well established that generalized master equation methods can have shortcomings leading to the occurrence of negative densities in certain parameter regimes. This has also been observed for the 1vN approach. For the 2vN approach an unphysical negative linear conductance occurs in the regime where sequential tunneling is blocked and elastic cotunneling amplitudes cancel due to interference, as discussed in Sec. 8.4. Under the same conditions, negative densities may occur. It would be interesting to further explore the limitations of the 2vN approach in order to identify other potentially problematic regimes, and set up clear criteria for when the method safely can be applied, or develop a new approximate scheme without these drawbacks. Moreover, so far analytical results are only available for two particularly simple model systems, namely for a single level without spin, and the Anderson model with degenerate levels and infinite Coulomb repulsion. This is due to the complicated equations of motion for the terms containing a single electron-hole pair, which have the form of integro-differential equations. Further analytical results for other systems will require more insight in the analytical structure and probably also some further model-dependent approximations.

Apart from the more fundamental aspects, also the task of establishing an efficient numerical implementation of the 2vN method is unsolved. So far only systems with at most two single-particle levels, i.e. containing four many-particle states, have been treated, but dealing with larger systems will require automatized numerical schemes.

The results presented in this thesis are all for the steady-state values of the current, and so far little attention has been devoted to the time-dependence of the 2vN equations, where the only example is shown in Sec. III in Paper II. In the derivations of the 2vN equations the Markov approximation was applied, which might limit the validity of the method for time-dependent problems, but maybe it is possible to modify the derivation to better account for the time-dependence. E.g., Ref. [37] might provide helpful ideas in this context.

An even more interesting topic is the calculation of higher-order cumulants, such as, e.g., the noise, using full-counting statistics. It has previously been shown that the higher-order cumulants can give access to information not available in the average current, such as, e.g., the transport mechanism in quantum shuttles [39], or bunching of electrons in the inelastic cotunneling regime for transport through a single dot [50]. Some preliminary studies were performed for the 2vN method for different model systems, but some of the results were clearly wrong. It would be interesting to figure out whether this is due to numerical problems or, more likely, due to the applied approximation scheme used for deriving the 2vN equations. One source for the unphysical results could be the application of the Markov approximation, see, e.g., Ref. [51].

The work in thesis is about the theoretical description of quantum transport through nanostructures. The method introduced, 2vN, is based on the many-particle density matrix formalism and includes transport processes beyond sequential tunneling. Several other density-matrix based approaches are available, in particular methods which only include transport processes to lowest order in the coupling, while transport beyond sequential tunneling is less studied. Especially in this context, this thesis may provide a useful step in a developing field.

Appendices

A

The capacitance model for a double quantum dot

From classical electrostatics it is known that the charge Q_i on the ith conductor connected to N other conductors is

$$Q_i = \sum_{j=0}^{N} C_{ij}(V_i - V_j) \tag{A.1}$$

where the zeroth conductor is defined to be grounded, $V_0 = 0$.

For the system shown in Fig. 4.1, the charges on the two dots can be expressed as[1]

$$\begin{aligned} Q_1 &= C_{L1}(V_1 - V_L) + C_{R1}(V_1 - V_R) + C_{g1}(V_1 - V_g) + C_m(V_1 - V_2), && \text{(A.2)} \\ Q_2 &= C_{L2}(V_2 - V_L) + C_{R2}(V_2 - V_R) + C_{g2}(V_2 - V_g) + C_m(V_2 - V_1), && \text{(A.3)} \end{aligned}$$

which can be arranged on the form

$$\mathbf{V} = \begin{pmatrix} V_1 \\ V_2 \end{pmatrix} = \underline{\underline{\mathbf{C}}}^{-1} \begin{pmatrix} Q_1 + C_{L1}V_L + C_{R1}V_R + C_{g1}V_g \\ Q_2 + C_{R2}V_R + C_{L2}V_L + C_{g2}V_g \end{pmatrix} \tag{A.4}$$

with $\underline{\underline{\mathbf{C}}}$ being the capacitance matrix for system consisting of the two dots,

$$\underline{\underline{\mathbf{C}}} = \begin{pmatrix} C_1 & -C_m \\ -C_m & C_2 \end{pmatrix}, \tag{A.5}$$

where $C_1 = C_{L1} + C_{R1} + C_{g1} + C_m$ and $C_2 = C_{R2} + C_{L2} + C_{g2} + C_m$.

Defining $Q_1 = -eN_1$ and $Q_2 = -eN_2$, with $e = |e|$, the *electrostatic* energy of the conductor network in terms of the voltages and the charges on the dots

---

[1] The derivation is similar to Ref. [17]. Note also that S(ource) and D(rain) have been replaced with L(eft) and R(ight), respectively.

is[2]

$$\begin{aligned}
U(N_1,N_2,V_L,V_R,V_g) &= \frac{1}{2}\,\mathbf{V}\cdot(\underline{\underline{\mathbf{C}}}\mathbf{V}) \\
&= \frac{1}{2}E_{C1}N_1^2+\frac{1}{2}E_{C2}N_2^2+E_{Cm}N_1N_2 \\
&+\frac{1}{C_1C_2-C_m^2}\Bigg[-e(C_{g2}V_g+C_{R2}V_R+C_{L2}V_L)(N_2C_1+N_1C_m) \\
&-e(C_{g1}V_g+C_{L1}V_L+C_{R1}V_R)(N_2C_m+N_1C_2) \\
&+\frac{1}{2}(C_{g1}V_g+C_{L1}V_L+C_{R1}V_R)^2C_2 \\
&+\frac{1}{2}(C_{g2}V_g+C_{R2}V_R+C_{L2}V_L)^2C_1 \\
&+(C_{g1}V_g+C_{L1}V_L+C_{R1}V_R)(C_{g2}V_g+C_{R2}V_R+C_{L2}V_L)C_m\Bigg].
\end{aligned} \tag{A.6}$$

with

$$\begin{aligned}
E_{C1} &= \frac{e^2}{C_1}\left(\frac{1}{1-\frac{C_m^2}{C_1C_2}}\right), \qquad E_{C2}=\frac{e^2}{C_2}\left(\frac{1}{1-\frac{C_m^2}{C_1C_2}}\right), \qquad \text{(A.7)}\\
E_{Cm} &= \frac{e^2}{C_m}\left(\frac{1}{\frac{C_1C_2}{C_m^2}-1}\right).
\end{aligned}$$

The chemical potentials $\mu_{1,2}$ of the dots due to *electrostatics* are defined as the energies of the last added electron, and for a symmetrically applied bias voltage it becomes [see also Eqs. (4.1,4.2)]

$$\begin{aligned}
&\mu_1(N_1,N_2,V,V_g) \\
&\quad\equiv U(N_1,N_2,-V/2,V/2,V_g)-U(N_1-1,N_2,-V/2,V/2,V_g) \\
&\quad=\frac{1}{2}E_{C1}(2N_1-1)+E_{Cm}N_2-e\alpha_g^1V_g+e\alpha_V^1\frac{V}{2}.
\end{aligned} \tag{A.8}$$

and

$$\begin{aligned}
&\mu_2(N_1,N_2,V,V_g) \\
&\quad\equiv U(N_1,N_2,-V/2,V/2,V_g)-U(N_1,N_2-1,-V/2,V/2,V_g) \\
&\quad=\frac{1}{2}E_{C2}(2N_2-1)+E_{Cm}N_1-e\alpha_g^2V_g-e\alpha_V^2\frac{V}{2}.
\end{aligned} \tag{A.9}$$

---

[2] Often we will not write the voltage dependence explicitly.

where the lever arms

$$\alpha_V^1 = \frac{C_2(C_{L1} - C_{R1}) + C_m(C_{L2} - C_{R2})}{C_1C_2 - C_m^2}, \tag{A.10}$$

$$\alpha_V^2 = \frac{C_m(C_{R1} - C_{L1}) + C_1(C_{R2} - C_{L2})}{C_1C_2 - C_m^2}, \tag{A.11}$$

$$\alpha_g^1 = \frac{C_2C_{g1} + C_{g2}C_m}{C_1C_2 - C_m^2}, \tag{A.12}$$

$$\alpha_g^2 = \frac{C_1C_{g2} + C_{g1}C_m}{C_1C_2 - C_m^2}, \tag{A.13}$$

have been introduced. The lever arms express the change in the chemical potentials of the dots due to a change in bias or gate voltage.

The change in chemical potential for adding an electron to dot 1 at fixed bias and gate voltage is called the addition energy (or the charging energy) and is defined as $\mu_1(N_1+1, N_2) - \mu_1(N_1, N_2) = E_{C1}$, where a similar expression holds for dot 2. Due to the cross-capacitance, C_m, the chemical potential in one dot is changed when adding a charge to the other,
$\mu_1(N_1, N_2+1) - \mu_1(N_1, N_2) = \mu_2(N_1+1, N_2) - \mu_1(N_1, N_2) = E_{Cm}$.

In summary, there are seven capacitances, C_{g1}, C_{g2}, C_{L1}, C_{L2}, C_{R1}, C_{R2} and C_m which have to be fixed from the experimental data in order to determine the charging energies E_{C1}, E_{C2} and E_{Cm}. As explained below, the experimental data can only provide five relations between the capacitances and therefore we have to fix C_{L2}/C_{L1} and C_{R1}/C_{R2} based on electrostatic modelling of the nanowire in order to solve for the capacitances.

B

Extracting capacitances from double quantum dot data

In this appendix, it is shown how to extract the capacitances from the experimental data for the double quantum dot system described in Chap. 4.

In Fig. 4.2a, the distances between the dashed green lines are related to the interdot charging energy E_{Cm}: At *fixed bias voltage* and being on a dashed green line $\mu_L = \mu_1(N_1, N_2, V, V_g)$, lowering the gate voltage leads to a change in occupation of dot 2 thereby changing the chemical potential of dot 1. At the dashed green line below, with the gate voltage $V_g - \Delta V_g^{\text{green}}$, the chemical potential of dot 1 is again aligned with the chemical potential of the left lead, but the occupation of dot 2 has changed by one, i.e. $\mu_L = \mu_1(N_1, N_2 - 1, V, V_g - \Delta V_g^{\text{green}})$, see Fig. 4.4. Subtracting the two expressions gives

$$\Delta V_g^{\text{green}} = \frac{E_{Cm}}{\alpha_g^1} = \frac{1}{\alpha_g^1} \frac{e^2}{C_m} \left(\frac{1}{\frac{C_1 C_2}{C_m^2} - 1} \right). \tag{B.1}$$

Two neighbouring dashed red lines both correspond to the alignment of the right chemical potential with the chemical potential of dot 2, but with the occupation of dot 2 changed by one, see Fig. 4.4. Also at *fixed bias voltage*, the distance ΔV_g^{red} between the dashed red lines gives the relations, $\mu_R = \mu_1(N_1, N_2, V, V_g) = \mu_1(N_1, N_2 - 1, V, V_g - \Delta V_g^{\text{red}})$, leading to

$$\Delta V_g^{\text{red}} = \frac{E_{C2}}{\alpha_g^2} = \frac{1}{\alpha_g^2} \frac{e^2}{C_2} \left(\frac{1}{1 - \frac{C_m^2}{C_1 C_2}} \right). \tag{B.2}$$

Along the dashed green lines, the filling of dot 1 and 2 is constant and the left chemical potential is aligned with the chemical potential of dot 1. Choosing two points on the line, (V_{bias}, V_g) and $(V_{\text{bias}} + \Delta V_{\text{bias}}, V_g - \Delta V_g)$ and using $eV_{\text{bias}}/2 = \mu_1(N_1, N_2, V_{\text{bias}}, V_g)$ and $e(V_{\text{bias}} + \Delta V_{\text{bias}})/2 = \mu_1(N_1, N_2, V_{\text{bias}} +$

$\Delta V_{\mathrm{bias}}, V_g - \Delta V_g)$, gives the slope of the dashed green line

$$\alpha_{\mathrm{green}} = \frac{\alpha_V^1 - 1}{2\alpha_g^1} = \frac{C_2([C_{L1} - C_{R1}] - C_1) + C_m(C_m - [C_{R2} - C_{L2}])}{2(C_{g2}C_m + C_2C_{g1})}. \tag{B.3}$$

Similarly, using that along the red dashed lines the chemical potential of the right lead is aligned with chemical potential of dot 2, the slopes are

$$\alpha_{\mathrm{red}} = \frac{1 - \alpha_V^2}{2\alpha_g^2} = \frac{C_1(C_2 - [C_{R2} - C_{L2}]) + C_m([C_{L1} - C_{R1}] - C_m)}{2(C_{g2}C_1 + C_mC_{g1})}. \tag{B.4}$$

Finally, on the resonance lines, the chemical potential in dot 1 for an electron filling in the two dots being N_1, N_2, respectively, is aligned with the chemical potential in dot 2 for a filling of the dots $N_1 - 1$ and $N_2 + 1$, i.e. $\mu_1(N_1, N_2, V_{\mathrm{bias}}, V_g) = \mu_2^*(N_1 - 1, N_2 + 1, V_{\mathrm{bias}}, V_g)$, where the '*' indicates, that the tunneling through dot 2 might happen through an excited state. The slopes of the resonance lines are

$$\alpha_{\mathrm{resonance}} = \frac{\alpha_V^1 + \alpha_V^2}{2\left[\alpha_g^1 - \alpha_g^2\right]} = \frac{[C_{R2} - C_{L2}](C_1 - C_m) + [C_{L1} - C_{R1}](C_2 - C_m)}{2[C_{g2}(C_m - C_1) + C_{g1}(C_2 - C_m)]}. \tag{B.5}$$

In total, five relations between the capacitances have been obtained.

C

Cotunneling rates for the single quantum dot

The cotunneling rates γ_{11}^{RL} and γ_{11}^{LR}

First the rate γ_{11}^{RL} is considered with the initial state $|\, i\rangle = |\, \nu_L \nu_R 1\rangle$ and the final states $|\, f_{kk'}\rangle = c^\dagger_{kR} c_{k'L} \,|\, i\rangle$, where the energies are $E_i = E_{\nu_L\nu_R} + E_1$ and $E_{f_{kk'}} = E_i - E_{k'L} + E_{kR}$, respectively. There are two different transport processes: $|\, 1\rangle \to |\, 0\rangle \to |\, 1\rangle$ and $|\, 1\rangle \to |\, d\rangle \to |\, 1\rangle$, and as they have the same final state they interfere with each other.

According to Eq. (8.2), the cotunneling rate is

$$\begin{aligned}
\gamma_{11}^{RL} &= 2\pi \sum_{kk'} \sum_{\nu_L\nu_R} W_{\nu_L\nu_R} \bigg| \sum_{k_1k_2} \Big\{ \langle f_{kk'} \,|\, V^*_{k_2L1} d_1^\dagger c_{k_2L} \frac{1}{E_i - H_0} V_{k_1R1} c^\dagger_{k_1R} d_1 \,|\, i\rangle \\
&\qquad + \langle f_{kk'} \,|\, V_{k_2R2} c^\dagger_{k_2R} d_2 \frac{1}{E_i - H_0} V^*_{k_1L2} d_2^\dagger c_{k_1L} \,|\, i\rangle \Big\} \bigg|^2 \delta(E_{f_{kk'}} - E_i) \\
&= 2\pi \sum_{kk'} \sum_{\nu_L\nu_R} W_{\nu_L\nu_R} \delta(E_{f_{kk'}} - E_i) \\
&\qquad \bigg| \sum_{k_1k_2} \Big\{ \frac{V^*_{k_2L1} V_{k_1R1}}{E_i - (E_i + E_{k_1R} - E_1)} \langle i \,|\, c^\dagger_{k'L} c_{kR} d_1^\dagger c_{k_2L} c^\dagger_{k_1R} d_1 \,|\, i\rangle \\
&\qquad + \frac{V_{k_2R2} V^*_{k_1L2}}{E_i - (E_i - E_{k_1L} + E_2 + U)} \langle i \,|\, c^\dagger_{k'L} c_{kR} c^\dagger_{k_2R} d_2 d_2^\dagger c_{k_1L} \,|\, i\rangle \Big\} \bigg|^2 \\
&= 2\pi \sum_{kk'} \sum_{\nu_L\nu_R} W_{\nu_L\nu_R} \bigg| \sum_{k_1k_2} \Big\{ \frac{V^*_{k_2L1} V_{k_1R1}}{E_1 - E_{k_1R}} \langle i \,|\, c^\dagger_{k'L} c_{kR} c_{k_2L} c^\dagger_{k_1R} \,|\, i\rangle \\
&\qquad + \frac{V_{k_2R2} V^*_{k_1L2}}{E_{k_1L} - E_2 - U} \langle i \,|\, c^\dagger_{k'L} c_{kR} c^\dagger_{k_2R} c_{k_1L} \,|\, i\rangle \Big\} \bigg|^2 \delta(E_{f_{kk'}} - E_i),
\end{aligned} \tag{C.1}$$

and finally

$$\gamma_{11}^{RL} = 2\pi \sum_{kk'} \sum_{\nu_L\nu_R} W_{\nu_L\nu_R} \Big| \sum_{k_1k_2} \Big\{ \frac{-V^*_{k_2L1}V_{k_1R1}}{E_1 - E_{k_1R}} \langle i \,|\, c^\dagger_{k'L} c_{k_2L} c_{kR} c^\dagger_{k_1R} \,|\, i\rangle + \frac{V_{k_2R2}V^*_{k_1L2}}{E_{k_1L} - E_2 - U} \langle i \,|\, c^\dagger_{k'L} c_{k_1L} c_{kR} c^\dagger_{k_2R} \,|\, i\rangle \Big\} \Big|^2 \delta(E_{f_{kk'}} - E_i). \tag{C.2}$$

Carrying out the sums over k_1k_2 and inserting the energies gives

$$\gamma_{11}^{RL} = 2\pi \sum_{kk'} \sum_{\nu_L\nu_R} W_{\nu_L\nu_R} \Big| \left(\frac{-V^*_{k'L1}V_{kR1}}{E_1 - E_{kR}} + \frac{V_{kR2}V^*_{k'L2}}{E_{k'L} - E_2 - U} \right) \langle i \,|\, c^\dagger_{k'L} c_{k'L} [1 - c^\dagger_{kR} c_{kR}] \,|\, i\rangle \Big|^2 \delta(E_{kR} - E_{k'L}). \tag{C.3}$$

As the matrix elements are either $0, 1$ they can be taken outside the square. Moreover, it holds that

$$\begin{aligned} &\sum_{\nu_L\nu_R} W_{\nu_L\nu_R} \langle \nu_L\nu_R \,|\, c^\dagger_{k'L} c_{k'L} [1 - c^\dagger_{kR} c_{kR}] \,|\, \nu_L\nu_R\rangle \\ &\quad = \left(\sum_{\nu_L} W_{\nu_L} \langle \nu_L \,|\, c^\dagger_{k'L} c_{k'L} \,|\, \nu_L\rangle \right) \left(\sum_{\nu_R} W_{\nu_R} \langle \nu_R \,|\, [1 - c^\dagger_{kR} c_{kR}] \,|\, \nu_R\rangle \right) \\ &\quad = f_{k'L}[1 - f_{kR}], \end{aligned} \tag{C.4}$$

with $f_{k'L} = n_F(E_{k'L} - \mu_L)$ being the Fermi function, not to be confused with the state $|\, f_{kk'}\rangle$. In the first equality a complete set of lead states have been inserted. When carrying out the internal sums, the definition of the Fermi function has been used.

Inserting Eq. (C.4) in Eq. (C.3) gives

$$\begin{aligned} \gamma_{11}^{RL} &= 2\pi \sum_{kk'} f_{k'L}[1 - f_{kR}] \Big| \frac{V^*_{k'L1}V_{kR1}}{E_1 - E_{kR}} + \frac{V_{kR2}V^*_{k'L2}}{E_2 + U - E_{k'L}} \Big|^2 \delta(E_{kR} - E_{k'L}) \\ &= 2\pi \sum_{kk'} f_{k'L}[1 - f_{kR}] |t_{k'L}|^2 |t_{kR}|^2 \\ &\qquad \Big| \frac{x^*_{L1}x_{R1}}{E_1 - E_{kR}} + \frac{x_{R2}x^*_{L2}}{E_2 + U - E_{k'L}} \Big|^2 \delta(E_{kR} - E_{k'L}) \\ &= 2\pi \int dE \int dE' \sum_{kk'} |t_{k'L}|^2 \delta(E' - E_{k'L}) |t_{kR}|^2 \delta(E - E_{kR}) \\ &\qquad \Big| \frac{x^*_{L1}x_{R1}}{E_1 - E} + \frac{x_{R2}x^*_{L2}}{E_2 + U - E'} \Big|^2 n_F(E' - \mu_L)[1 - n_F(E - \mu_R)] \delta(E - E'). \end{aligned} \tag{C.5}$$

Introducing the coupling constants, $\Gamma_\ell(E) = 2\pi \sum_k |t_{k\ell}|^2 \delta(E - E_{k\ell})$, leads to

$$\begin{aligned}\gamma_{11}^{RL} = \frac{1}{2\pi} \int dE \int dE' \Gamma_L(E')\Gamma_R(E) \Big| \frac{x_{L1}^* x_{R1}}{E_1 - E} + \frac{x_{R2} x_{L2}^*}{E_2 + U - E'} \Big|^2 \\ n_F(E' - \mu_L)[1 - n_F(E - \mu_R)]\delta(E - E').\end{aligned} \tag{C.6}$$

Carrying out one of the integrals and assuming the Wide Band Limit, i.e. $\Gamma_\ell(E) = \Gamma_\ell$, we obtain the final result

$$\gamma_{11}^{RL} = \frac{\Gamma_L \Gamma_R}{2\pi} \int dE \Big| \frac{x_{L1}^* x_{R1}}{E_1 - E} + \frac{x_{R2} x_{L2}^*}{E_2 + U - E} \Big|^2 n_F(E - \mu_L)[1 - n_F(E - \mu_R)] \tag{C.7}$$

The rate for electron transport in the opposite direction, γ_{11}^{LR}, is found by interchanging $L \leftrightarrow R$ in Eq. (C.7).

The cotunneling rates γ_{21}^{LR} and γ_{21}^{RL}

Starting with the rate γ_{21}^{RL}, in this case there are two nonvanishing matrix elements, which come from the processes $|\,1\rangle \rightarrow |\,0\rangle \rightarrow |\,2\rangle$ and $|\,1\rangle \rightarrow |\,d\rangle \rightarrow |\,2\rangle$. The initial state is $|\,i\rangle = |\,\nu_L \nu_R 1\rangle$ with energy $E_i = E_{\nu_L \nu_R} + E_1$, and the final states are $|\,f_{kk'}\rangle = d_2^\dagger c_{kR}^\dagger c_{k'L} d_1 \,|\,i\rangle$ with energies $E_{f_{kk'}} = E_i - E_1 + E_2 - E_{k'L} + E_{kR}$.

The absolute square in Eq. (8.2) becomes

$$\begin{aligned}
&\Bigg| \sum_{k_1 k_2} \Big\{ \langle f_{kk'} \,|\, V_{k_2 L2}^* d_2^\dagger c_{k_2 L} \frac{1}{E_i - H_0} V_{k_1 R1} c_{k_1 R}^\dagger d_1 \,|\, i\rangle \\
&\qquad + \langle f_{kk'} \,|\, V_{k_2 R1} c_{k_2 R}^\dagger d_1 \frac{1}{E_i - H_0} V_{k_1 L2}^* d_2^\dagger c_{k_1 L} \,|\, i\rangle \Big\} \Bigg|^2 \\
&= \Bigg| \sum_{k_1 k_2} \Big\{ \frac{V_{k_2 L2}^* V_{k_1 R1}}{E_i - (E_i - E_1 + E_{k_1 R})} \langle i \,|\, d_1^\dagger c_{k'L}^\dagger c_{kR} d_2 d_2^\dagger c_{k_2 L} c_{k_1 R}^\dagger d_1 \,|\, i\rangle \\
&\qquad + \frac{V_{k_2 R1} V_{k_1 L2}^*}{E_i - (E_i - E_{k_1 L} + E_2 + U)} \langle i \,|\, d_1^\dagger c_{k'L}^\dagger c_{kR} d_2 c_{k_2 R}^\dagger d_1 d_2^\dagger c_{k_1 L} \,|\, i\rangle \Big\} \Bigg|^2 \\
&= \Bigg| \frac{V_{k'L2}^* V_{kR1}}{E_1 - E_{kR}} \langle i \,|\, d_1^\dagger c_{k'L}^\dagger c_{kR} d_2 d_2^\dagger c_{k'L} c_{kR}^\dagger d_1 \,|\, i\rangle \\
&\qquad + \frac{V_{kR1} V_{k'L2}^*}{E_{k'L} - E_2 - U} \langle i \,|\, d_1^\dagger c_{k'L}^\dagger c_{kR} d_2 c_{kR}^\dagger d_1 d_2^\dagger c_{k'L} \,|\, i\rangle \Bigg|^2 .
\end{aligned} \tag{C.8}$$

The two matrix elements become

$$\langle i\,|\,d_1^\dagger c_{k'L}^\dagger c_{kR} d_2 d_2^\dagger c_{k'L} c_{kR}^\dagger d_1\,|\,i\rangle = -\,\langle \nu_L\nu_R\,|\,c_{k'L}^\dagger c_{k'L}[1-c_{kR}^\dagger c_{kR}]\,|\,\nu_L\nu_R\rangle\,, \tag{C.9}$$

$$\langle i\,|\,d_1^\dagger c_{k'L}^\dagger c_{kR} d_2 c_{kR}^\dagger d_1 d_2^\dagger c_{k'L}\,|\,i\rangle = -\,\langle \nu_L\nu_R\,|\,c_{k'L}^\dagger c_{k'L}[1-c_{kR}^\dagger c_{kR}]\,|\,\nu_L\nu_R\rangle\,, \tag{C.10}$$

so after summing over $\nu_L\nu_R$, Eq. (C.8) becomes

$$|\cdots|^2 = |t_{k'L}|^2|t_{kR}|^2 \left|\frac{x_{L2}^* x_{R1}}{E_1 - E_{kR}} + \frac{x_{L2}^* x_{R1}}{E_{k'L} - E_2 - U}\right|^2 f_{k'L}[1-f_{kR}] \tag{C.11}$$

The energy differences between the initial and final states are $E_{f_{kk'}} - E_i = E_{kR} + E_2 - E_1 - E_{k'L}$, which in the Wide Band Limit leads to [see Eqs. (C.5,C.7)]

$$\begin{aligned}\gamma_{21}^{RL} = \frac{\Gamma_L\Gamma_R}{2\pi}\int dE &\left|\frac{x_{L2}^* x_{R1}}{E_1 - E} - \frac{x_{L2}^* x_{R1}}{E_2 + U - E}\right|^2 \\ &n_F(E + E_2 - E_1 - \mu_L)[1 - n_F(E - \mu_R)].\end{aligned} \tag{C.12}$$

Again, the rate γ_{21}^{LR} is found by interchanging $L \leftrightarrow R$.

References

References

[1] K. von Klitzing, For the discovery of the quantized Hall effect, www.nobel.se/physics/laureates/1985/.

[2] Z. I. Alferov and H. Kroemer, For developing semiconductor heterostructures used in high-speed and opto-electronics, www.nobel.se/physics/laureates/2000/.

[3] R. B. Laughlin, H. L. Stormer, and D. C. Tsui, For their discovery of a new form of quantum fluid with fractionally charged excitations, www.nobel.se/physics/laureates/1998/.

[4] A. Wacker, Phys. Rep. **357**, 1 (2002).

[5] A. Yacoby, H. Stormer, K. W. Baldwin, L. N. Pfeiffer, and K. W. West, Solid State Communications **101**, 77 (1997).

[6] X. Duan, Y. Huang, Y. Cui, J. Wang, and C. M. Lieber, Nature **409**, 66 (2001).

[7] B. J. Ohlsson, M. T. Björk, B. J. Ohlsson, M. H. Magnusson, K. Deppert, L. Samuelson, and L. R. Wallenberg, Appl. Phys. Lett. **79**, 3335 (2001).

[8] L. P. Kouwenhoven, C. M. Marcus, P. L. McEuen, S. Tarucha, R. M. Westervelt, and N. S. Wingreen, in *Mesoscopic Electron Transport*, Vol. 345 of *Series E: Applied Sciences*, edited by L. L. Sohnn, L. P. Kouwenhoven, and G. Schön (Kluwer Academic Publishers, Dordrecht/Boston/London, 1997), pp. 105–214.

[9] D. G. Austing, S. Sasaki, S. Tarucha, S. M. Reimann, M. Koskinen, and M. Manninen, Phys. Rev. B **60**, 11514 (1999).

[10] D. Bimberg, M. Grundmann, and N. Ledentsov, *Quantum Dot Heterostructures* (John Wiley & Sons Ltd., New York, 1999).

[11] *Carbon Nanotubes: Synthesis, Structure, Properties and Applications*, edited by R. E. Smalley, M. S. Dresselhaus, G. Dresselhaus, and P. Avouris (Springer-Verlag, Berlin, Heidelberg, New York, 2001).

[12] H. Park, J. Park, A. K. L. Lim, E. H. Anderson, A. P. Alivisatos, and P. L. McEuen, Nature **407**, 57 (2000).

[13] S. Kubatkin, A. Danilov, M. Hjort, J. Cornil, J.-L. Bredas, N. Stuhr-Hansen, P. Hedegard, and T. Bjornholm, Nature **425**, 698 (2003).

[14] M. T. Björk, B. J. Ohlsson, T. Sass, A. I. Persson, C. Thelander, M. H. Magnusson, K. Deppert, L. R. Wallenberg, and L. Samuelson, Nano Letters **2**, 87 (2002).

[15] M. Björk, C. Thelander, A. Hansen, L. Jensen, M. Larsson, L. Wallenberg, and L. Samuelson, Nano Letters **4**, 1621 (2004).

[16] Y. Cui, L. J. Lauhon, M. S. Gudiksen, J. Wang, and C. M. Lieber, Appl. Phys. Lett. **78**, 2214 (2001).

[17] W. G. v. Wiel, S. D. Franceschi, J. M. Elzerman, T. Fujisawa, S. Tarucha, and L. P. Kouwenhoven, Rev. Mod. Phys. **75**, 1 (2003).

[18] M. T. Björk, A. Fuhrer, A. E. Hansen, M. W. Larsson, L. E. Fröberg, and L. Samuelson, Phys. Rev. B **72**, 201307(R) (2005).

[19] S. Nilsson and I. Ragnarsson, *Shapes and Shells in Nuclear Structure* (Cambridge University Press, Cambridge, 1995).

[20] M.-E. Pistol and C. E. Pryor, Phys. Rev. B **78**, 115319 (2008).

[21] C. Fasth, A. Fuhrer, M. T. Björk, and L. Samuelson, Nano Letters **5**, 1487 (2005).

[22] L. Kouwenhoven and L. Glazman, Physics World **January 2001**, 33 (2001).

[23] A. Rosch, J. Paaske, J. Kroha, and P. Wölfle, Phys. Rev. Lett. **90**, 076804 (2003).

[24] J. Paaske, A. Rosch, J. Kroha, and P. Wölfle, Phys. Rev. B **70**, 155301 (2004).

[25] V. Meden, W. Metzneran, U. Schollwöck, and K. Schönhammer, J. Low Temp. Phys. **126**, 1147 (2002).

[26] S. R. White, Phys. Rev. Lett. **69**, 2863 (1992).

[27] S. R. White, Phys. Rev. B **48**, 10345 (1993).

[28] A. G. Redfield, IBM Journal of Research and Development **1**, 19 (1957).

[29] S. A. Gurvitz and Y. S. Prager, Phys. Rev. B **53**, 15932 (1996).

[30] S. A. Gurvitz, Phys. Rev. B **57**, 6602 (1998).

[31] H. Schoeller and G. Schön, Phys. Rev. B **50**, 18436 (1994).

[32] J. König, J. Schmid, H. Schoeller, and G. Schön, Phys. Rev. B **54**, 16820 (1996).

[33] J. König, H. Schoeller, and G. Schön, Phys. Rev. Lett. **76**, 1715 (1996).

[34] D. A. Ryndyk, R. Gutierrez, B. Song, and G. Cuniberti, arXiv:0805.0628v2 (unpublished).

[35] H. Haug and A.-P. Jauho, *Quantum Kinetics in Transport and Optics of Semiconductors* (Springer, Berlin, 1996).

[36] H.-P. Breuer and F. Petruccione, *The Theory of Open Quantum Systems* (Oxford University Press, Oxford, 2002).

[37] C. Timm, Phys. Rev. B **77**, 195416 (2008).

[38] B. Elatari and S. Gurvitz, Phys. Lett. A **292**, 289 (2002).

[39] T. Novotný, A. Donarini, C. Flindt, and A.-P. Jauho, Phys. Rev. Lett. **92**, 248302 (2004).

[40] C. Flindt, T. Novotný, and A.-P. Jauho, Phys. Rev. B **70**, 205334 (2004).

[41] B. Elattari and S. A. Gurvitz, Phys. Rev. Lett. **84**, 2047 (2000).

[42] J. König, Ph.D. thesis, University Karlsruhe, 1998.

[43] J. König and J. Martinek, Phys. Rev. Lett. **90**, 166602 (2003).

[44] M. Braun, J. König, and J. Martinek, Phys. Rev. B **70**, 195345 (2004).

[45] A. Thielmann, M. H. Hettler, J. König, and G. Schön, Phys. Rev. B **68**, 115105 (2003).

[46] J. König, H. Schoeller, and G. Schön, Phys. Rev. Lett. **78**, 4482 (1997).

[47] R. Schleser, T. Ihn, E. Ruh, K. Ensslin, M. Tews, D. Pfannkuche, D. C. Driscoll, and A. C. Gossard, Phys. Rev. Lett. **94**, 206805 (2005).

[48] D. Becker and D. Pfannkuche, Phys. Rev. B **77**, 205307 (2008).

[49] I. Weymann, J. König, J. Martinek, J. Barnas, and G. Schön, Phys. Rev. B **72**, 115334 (2005).

[50] A. Thielmann, M. H. Hettler, J. Konig, and G. Schon, Phys. Rev. Lett. **95**, 146806 (2005).

[51] A. Braggio, J. Konig, and R. Fazio, Phys. Rev. Lett. **96**, 026805 (2006).

[52] T. Kuhn, in *Theory of Transport Properties of Semiconductor Nanostructures*, edited by E. Schöll (Chapman and Hall, London, 1998).

[53] C. Flindt, T. Novotny, A. Braggio, M. Sassetti, and A.-P. Jauho, Phys. Rev. Lett. **100**, 150601 (2008).

[54] A. Wacker, physica status solidi (c) **5**, 215 (2008).

[55] A. Wacker (unpublished).

[56] D. C. Ralph and R. A. Buhrman, Phys. Rev. Lett. **69**, 2118 (1992).

[57] D. C. Ralph and R. A. Buhrman, Phys. Rev. B **51**, 3554 (1995).

[58] J. Konemann, B. Kubala, J. Konig, and R. J. Haug, Phys. Rev. B **73**, 033313 (2006).

[59] Y. Utsumi, J. Martinek, G. Schon, H. Imamura, and S. Maekawa, Phys. Rev. B **71**, 245116 (2005).

[60] J. Jin, X. Zheng, and Y. Yan, J. Chem. Phys. **128**, 234703 (2008).

[61] R. S. Whitney, J. Phys. A **41**, 175304 (2008).

[62] G. Lindblad, Commun. math. Phys. **48**, 119 (1976).

[63] G. Schaller and T. Brandes, Phys. Rev. A **78**, 022106 (2008).

[64] J. J. Sakurai, *Modern Quantum Mechanics - Revised Edition* (Addison-Wesley, Reading, Massachusetts, 1994).

[65] M. R. Wegewijs and Y. V. Nazarov, Phys. Rev. B **60**, 14318 (1999).

[66] T. H. Stoof and Y. V. Nazarov, Phys. Rev. B **53**, 1050 (1996).

[67] J. Aghassi, A. Thielmann, M. Hettler, and G. Schön, Phys. Rev. B **73**, 195323 (2006).

[68] I. Djuric, B. Dong, and H. L. Cui, J. Appl. Phys. **99**, 063710 (2006).

[69] B. Wunsch, M. Braun, J. König, and D. Pfannkuche, Phys. Rev. B **72**, 205319 (2005).

[70] B. Dong, H. L. Cui, and X. L. Lei, Phys. Rev. B **69**, 035324 (2004).

[71] J. N. Pedersen, Master's thesis, University of Copenhagen, 2004.

[72] M. Julliere, Physics Letters A **54**, 225 (1975).

[73] M. N. Baibich, J. M. Broto, A. Fert, F. N. Van Dau, F. Petroff, P. Etienne, G. Creuzet, A. Friederich, and J. Chazelas, Phys. Rev. Lett. **61**, 2472 (1988).

[74] G. Binasch, P. Grünberg, F. Saurenbach, and W. Zinn, Phys. Rev. B **39**, 4828 (1989).

[75] A. Fert and P. Grünberg, For the discovery of Giant Magnetoresistance, www.nobel.se/physics/laureates/2007/.

[76] S. Datta and B. Das, Applied Physics Letters **56**, 665 (1990).

[77] J. R. Petta, A. C. Johnson, J. M. Taylor, E. A. Laird, A. Yacoby, M. D. Lukin, C. M. Marcus, M. P. Hanson, and A. C. Gossard, Science **309**, 2180 (2005).

[78] D. Loss and D. P. DiVincenzo, Phys. Rev. A **57**, 120 (1998).

[79] S. J. van der Molen, N. Tombros, and B. J. van Wees, Phys. Rev. B **73**, 220406 (2006).

[80] R. S. Liu, D. Suyatin, H. Pettersson, and L. Samuelson, Nanotechnology **18**, 055302 (2007).

[81] J. Hauptmann, J. Paaske, and P. Lindelof, Nature Physics **4**, 373 (2008).

[82] J. N. Pedersen, J. Q. Thomassen, and K. Flensberg, Phys. Rev. B **72**, 045341 (2005).

[83] I. Weymann and J. Barnas, Eur. Phys. J. B **46**, 289 (2005).

[84] B. Horvath, B. Lazarovits, O. Sauret, and G. Zarand, Phys. Rev. B **77**, 113108 (2008).

[85] S. Datta, arXiv:cond-mat/0603034v1 (unpublished).

[86] D. V. Averin and Y. V. Nazarov, Phys. Rev. Lett. **65**, 2446 (1990).

[87] S. De Franceschi, S. Sasaki, J. M. Elzerman, W. G. van der Wiel, S. Tarucha, and L. P. Kouwenhoven, Phys. Rev. Lett. **86**, 878 (2001).

[88] D. M. Zumbuhl, C. M. Marcus, M. P. Hanson, and A. C. Gossard, Phys. Rev. Lett. **93**, 256801 (2004).

[89] M. Sigrist, T. Ihn, K. Ensslin, D. Loss, M. Reinwald, and W. Wegscheider, Phys. Rev. Lett. **96**, 036804 (2006).

[90] M. Sigrist, T. Ihn, K. Ensslin, M. Reinwald, and W. Wegscheider, Phys. Rev. Lett. **98**, 036805 (2007).

[91] L. H. Yu, Z. K. Keane, J. W. Ciszek, L. Cheng, M. P. Stewart, J. M. Tour, and D. Natelson, Phys. Rev. Lett. **93**, 266802 (2004).

[92] J. V. Holm, H. I. Jorgensen, K. Grove-Rasmussen, J. Paaske, K. Flensberg, and P. E. Lindelof, Phys. Rev. B **77**, 161406 (2008).

[93] P. Jarillo-Herrero, J. Kong, H. S. J. van der Zant, C. Dekker, L. P. Kouwenhoven, and S. D. Franceschi, Phys. Rev. Lett. **94**, 156802 (2005).

[94] A. Kogan, S. Amasha, D. Goldhaber-Gordon, G. Granger, M. A. Kastner, and H. Shtrikman, Phys. Rev. Lett. **93**, 166602 (2004).

[95] B. C. Stipe, M. A. Rezaei, and W. Ho, Science **280**, 1732 (1998).

[96] A. J. Heinrich, J. A. Gupta, C. P. Lutz, and D. M. Eigler, Science **306**, 466 (2004).

[97] M. Turek and K. A. Matveev, Phys. Rev. B **65**, 115332 (2002).

[98] R. A. Zak and K. Flensberg, Phys. Rev. B **77**, 045329 (2008).

[99] J. Aghassi, M. H. Hettler, and G. Schön, Applied Physics Letters **92**, 202101 (2008).

[100] A. Fuhrer, S. Luscher, T. Ihn, T. Heinzel, K. Ensslin, W. Wegscheider, and M. Bichler, Nature **413**, 822 (2001).

[101] M. Sigrist, A. Fuhrer, T. Ihn, K. Ensslin, S. E. Ulloa, W. Wegscheider, and M. Bichler, Phys. Rev. Lett. **93**, 066802 (2004).

[102] H. Bruus and K. Flensberg, *Many-Body Quantum Theory in Condensed Matter Physics*, 1st ed. (Oxford University Press, New York, 2004).

[103] J. Koch, F. von Oppen, Y. Oreg, and E. Sela, Phys. Rev. B **70**, 195107 (2004).

[104] J. Koch, F. von Oppen, and A. V. Andreev, Phys. Rev. B **74**, 205438 (2006).

[105] N. D. Lang, Phys. Rev. B **52**, 5335 (1995).

[106] M. Brandbyge, J.-L. Mozos, P. Ordejón, J. Taylor, and K. Stokbro, Phys. Rev. B **65**, 165401 (2002).

[107] C. Toher, A. Filippetti, S. Sanvito, and K. Burke, Phys. Rev. Lett. **95**, 146402 (2005).

[108] M. Koentopp, K. Burke, and F. Evers, Phys. Rev. B **73**, 121403 (2006).

[109] G. Stefanucci, C.-O. Almbladh, S. Kurth, E. K. U. Gross, A. Rubio, R. van Leeuwen, N. E. Dahlen, and U. von Barth, Lect. Notes Phys. **706**, 479 (2006).

[110] C. W. J. Beenakker, Phys. Rev. B **44**, 1646 (1991).

[111] J. M. Kinaret, Y. Meir, N. S. Wingreen, P. A. Lee, and X. Wen, Phys. Rev. B **46**, 4681 (1992).

[112] M. H. Hettler, W. Wenzel, M. R. Wegewijs, and H. Schoeller, Phys. Rev. Lett. **90**, 076805 (2003).

[113] B. Muralidharan, A. W. Ghosh, and S. Datta, Phys. Rev. B **73**, 155410 (2006).

[114] B. Muralidharan and S. Datta, Phys. Rev. B **76**, 035432 (2007).

[115] B. Muralidharan, L. Siddiqui, and A. W. Ghosh, arXiv:0806.3724v1 (unpublished).

[116] J. E. Han and V. H. Crespi, Appl. Phys. Lett. **79**, 2829 (2001).

[117] H. Sprekeler, G. Kießlich, A. Wacker, and E. Schöll, Phys. Rev. B **69**, 125328 (2004).

[118] J. Lambe and R. C. Jaklevic, Phys. Rev. **165**, 821 (1968).

[119] D. Goldhaber-Gordon, J. Göres, M. A. Kastner, H. Shtrikman, D. Mahalu, and U. Meirav, Phys. Rev. Lett. **81**, 5225 (1998).

[120] V. N. Golovach and D. Loss, Phys. Rev. B **69**, 245327 (2004).

[121] M. Leijnse and M. R. Wegewijs, arXiv:0807.4027v1 (unpublished).

Acknowledgments

To me physics is a social science – to have good collaborators is mandatory! Below is a poor attempt to thank those who have contributed to this Ph.D. thesis in one way or another.

First of all, I am very thankful to my supervisor, Andreas Wacker, for guiding me through the last four and a half years. Outlining the direction to go, always willing to help and discuss when necessary, but also giving me the possibility to follow my own ideas and interests. Thanks a lot, Andreas!

It was very nice to have Carl-Olof Almbladh as a co-supervisor for additional advice. Thanks, Carl-Olof.

I have enormously enjoyed sharing an office with Rikard Nelander. Whereas I am embarrassed to write that I never learnt to speak Swedish, he is now able to understand a very fast and sloppy version of Danish. An ability learnt from many discussions in the office, a ski/physics conference in Mauterndorf, and lunch breaks at his favorite lunch restaurant in Lund, 'Tegnérs Matsalar'. I have really enjoyed his always positive attitude. Thanks, Rikard.

In Lund I have also benefited a lot from an infinite number of discussions with Peter Samuelsson at the white board in his office, offering me the possibility to explain the status of the current problems and to learn about his many new ideas. Thanks, Peter.

I am also grateful to all the people who have been a part of Andreas Wacker's group in Lund, Benny Lassen, Greta Lindwall, Olov Karlström and Carsten Weber.

Many people have contributed to the publications included in this thesis, and I thank them all for nice collaborations.

While being exiled to Lund, I still kept the contact to my past in Copenhagen through seminars, conferences, workshops and summer schools. Thanks to Mathias Lunde, Dan Bohr, Tomas Novotny, Andrea Donarini, Thomas Frederiksen, Christian Flindt, Jens Paaske and Karsten Flensberg.

I would also like to thank all the staff at Mathematical Physics, Lund University, for a nice atmosphere and many good discussions, especially in the lunch room.

Of course also a warm thankyou to friends and family for support and not

least for listening to me through the periods of ups and downs which make up doing a Ph.D.

Finally, a special thankyou to the most important ones, Daniel and Mai!

Part B

The Papers

The Papers—Summary and contributions to papers

Paper I

The paper deals with transport measurements of a double quantum dot in an InAs-InP nanowire. The data was analyzed using a capacitance model, extending previous work by also taking the lead-next-to-nearest-dot capacitances into account.

I contributed to the interpretation of the data, did the electrostatic modelling of the nanowire and performed all calculations of the capacitances. I did neither take part in the manufacturing of the nanowire nor in the measurements.

Paper II

Here a new approach for calculating transport through a nanostructure was presented. Formulated in a many-particle basis, all interactions within the nanostructure are treated exactly, while by including higher-order tunneling processes broadening is also incorporated.

I contributed to the formulation of the method, did the calculations for Figs. 1-2 and did large parts of the writing of the paper.

Paper III

The paper deals with sources for negative differential conductance in double quantum dots due to quantum mechanical effects. The results are extensions of previous work on the subject and give a more complete picture.

I contributed to the formulation of the problems to consider, did all calculations except for Fig. 5, and wrote large parts of the paper.

Paper IV

The paper describes a spintronic model consisting of a single quantum dot contacted to ferromagnetic leads, and in addition a magnetic field is applied. Both the linear response as well as the high-bias regime is discussed, and different approaches are compared.

I contributed to the formulation of the problems and especially to the understanding of the success of the mean-field approximation in the linear response regime. I also did all numerical implementations and calculations, except for the DMRG results and the master equation result. I also participated in the understanding of the failure of the Hubbard-I approach and wrote large parts of the manuscript.